8-8-2014 12:00 AM

Rapid Segmentation Techniques for Cardiac and Neuroimage Analysis

Martin Rajchl
The University of Western Ontario

Supervisor
Dr. Terry Peters
The University of Western Ontario

Graduate Program in Biomedical Engineering
A thesis submitted in partial fulfillment of the requirements for the degree in Doctor of Philosophy

RAPID SEGMENTATION TECHNIQUES FOR CARDIAC AND NEUROIMAGE ANALYSIS

(Thesis format: Integrated Article)

by

Martin Rajchl

Graduate Program in Biomedical Engineering

A thesis submitted in partial fulfillment
of the requirements for the degree of
Doctor of Philosophy

The School of Graduate and Postdoctoral Studies
Western University
London, Ontario, Canada

Abstract

Recent technological advances in medical imaging have allowed for the quick acquisition of highly resolved data to aid in diagnosis and characterization of diseases or to guide interventions. In order to to be integrated into a clinical work flow, accurate and robust methods of analysis must be developed which manage this increase in data. Recent improvements in inexpensive commercially available graphics hardware and General-Purpose Programming on Graphics Processing Units (GPGPU) have allowed for many large scale data analysis problems to be addressed in meaningful time and will continue to as parallel computing technology improves.

In this thesis we propose methods to tackle two clinically relevant image segmentation problems: a user-guided segmentation of myocardial scar from Late-Enhancement Magnetic Resonance Images (LE-MRI) and a multi-atlas segmentation pipeline to automatically segment and partition brain tissue from multi-channel MRI. Both methods are based on recent advances in computer vision, in particular max-flow optimization that aims at solving the segmentation problem in continuous space. This allows for (approximately) globally optimal solvers to be employed in multi-region segmentation problems, without the particular drawbacks of their discrete counterparts, graph cuts, which typically present with metrication artefacts. Max-flow solvers are generally able to produce robust results, but are known for being computationally expensive, especially with large datasets, such as volume images.

Additionally, we propose two new deformable registration methods based on Gauss-Newton optimization and smooth the resulting deformation fields via total-variation regularization to guarantee the problem is mathematically well-posed. We compare the performance of these two methods against four highly ranked and well-known deformable registration methods on four publicly available databases and are able to demonstrate a highly accurate performance with low run times. The best performing variant is subsequently used in a multi-atlas segmentation pipeline for the segmentation of brain tissue and facilitates fast run times for this computationally expensive approach.

All proposed methods are implemented using GPGPU for a substantial increase in computational performance and so facilitate deployment into clinical work flows. We evaluate all proposed algorithms in terms of run times, accuracy, repeatability and errors arising from user interactions and we demonstrate that these methods are able to outperform established methods.

The presented approaches demonstrate high performance in comparison with established methods in terms of accuracy and repeatability while largely reducing run times due to the employment of GPU hardware.

Keywords: Image Segmentation, Max-Flow, GPGPU, Magnetic Resonance Imaging, Deformable image registration, Myocardial Scar, Brain tissue

Acknowlegements

I want to emphasize how grateful I am to my supervisor, Terry Peters, who offered me the opportunity to study with him at Robarts Research Institute, after we talked in Vienna during his visit in Spring 2010. Three days after convocation for my master's degree, in September 2010, I sat on a plane heading to Canada to study medical imaging for four years, and I could not be more happy about the decision I made back then. Terry is an extra-ordinary researcher and advisor, and as I like to mention repeatedly, I highly doubt that a more productive study would have been possible for me anywhere else. It is due to the respectful and collegial environment that Terry creates in his laboratory that lets us conduct cutting edge research in a collaborative manner, and facilitates cross-fertilization of many projects and ideas. I also would like to mention that, by coincidence, my very first scientific citation is R.H.T. Bates and T.M. Peters, Towards Improvements in Tomography (1971), in my bachelor's thesis in 2005, while Chapter 2 of this thesis contains my first peer-reviewed and published paper, on which Terry is the senior author.

Any reader should know that this thesis would not have been in this form, if it was not for the many people contributing to these projects and whom I had the pleasure to work with and to learn from. I want to express my gratitude for all the council I have gotten from my advisory committee, Aaron D. Ward, David McCarty, and James A. White. I want to further highlight my closest collaborators Jing Yuan and James A. White and thank them for their mentorship and their invaluable contributions to many publications. Both supported and taught me endlessly and I hope through the collaborations we established, we enriched the field of image analysis by building bridges from computer vision theory to the clinic. At this point, I want to mention all my co-authors for bringing in their wisdom and experience to the many projects we have had over the last four years.

Further, I would like to mention all my colleagues and friends at Dr. Peters' VASST lab, especially John Baxter and Ali Khan for their support and sharing their knowledge with me,

and also the backbone of the laboratory, John Moore, Elvis Chen and Chris Wedlake, who had endless perseverance teaching me the principles of imaging and image-guided interventions.

I am very grateful for the many people, who enrich my life, celebrated with me in good times and supported me in hard times: Lukas Nespor, Markus Pantschier, Edith Hofbauer, Eileen Sung, Martin Meyrath, Tassilo Kaiser, Niko Nespor, Lisi Haider, Anna Grisold, Helle Mann, Anita Forche, Iris Mörwald and Sandra Muhry. You are the reason, why I am the person I am today and if I would have to do it all over again, I would not change a thing.

Lastly, I want to thank my family, my parents Marlene and Heinz Rajchl, and the best brother anyone can wish for, Andreas, for all the support, be it mental or financial, during the course of my years of studying: Without you, I would not even have the chance to get here. I consider myself indescribably lucky to be part of this family and I am grateful for everything you have done for me.

Contents

List of Figures

List of Tables

List of Appendices

List of Abbreviations, Symbols, and Nomenclature

ACM	Active Contour Model
ANN	Artificial Neural Network
ANTs	Advanced Normalization Tools
ART	Automatic Registration Toolbox
ASeTs	Advanced Segmentation Tools
ASM	Active Shape Model
AVD	Absolute Volume Difference
BG	Background
BMI	Body Mass Index
BS	Brain Stem
CE	Contrast Enhancement
cGM	Cortical Gray Matter
CHF	Congestive Heart Failure
CI	Confidence Interval
CMR	Cardiovascular Magnetic Resonance
CRT	Cardiac Resynchronization Therapy
CT	Computed Tomography
CV	Coefficient of variation
DAGMF	Directed Acyclic Graphical Max-Flow
DCM	Dilated Cardiomyopathy
DE	Distance Error
DR	Deformable Registration
DSC	Dice Similarity Coefficient
DT	Decision Tree
eCSF	External Cerebro-spinal Fluid
EDV	End-diastolic Volume
EF	Ejection Fraction
EM	Expectation Maximization
ESV	End-systolic Volume
FLAIR	Fluid-attenuated Inversion Recovery
FWHM	Full-Width-At-Half-Maximum
GFR	Glomerular Filtration Rate
GHMF	Generalized Hierarchical Max-flow
GMM	Gaussian Mixture Model
GN	Gauss-Newton
GPGPU	General-Purpose Programming on Graphics Processing Units
GPU	Graphics processing unit
GUI	Graphical User Interface
HD	Hausdorff Distance
HMF	Hierarchical Max-flow
HR	Heart Rate
ICC	Intra-class Correlation Coefficient
ICD	Implantable Cardioverter Defibrillator

ICM	Ischemic Cardiomyopathy
IID	Independent and Identically Distributed
IPAT	Integrated Parallel Acquisition Technique
IR	Inversion Recovery
IRTK	Image Registration Toolkit
JI	Jaccard Index
JLF	Joint Label Fusion
KNN	K-Nearest Neighbours
KSOM	Kohonen Self-organizing Map
LAX	Long-Axis
LE	Late Gadolinium Enhancement
LSM	Level Set Method
LV	Left ventricle, Left-ventricular
MAD	Mean Absolute Distance
MDD	Minimum Detectable Difference
MI	Mutual Information
MIP	Maximum Intensity Projection
MLF	Mean Label Fusion
MPR	Multi-planar Reformatted
MRF	Markov Random Field
MRI	Magnetic Resonance Imaging
MRO	Mean Region Overlap
N-D	*N*-Dimensional
OASIS	Open Access Series of Imaging Studies
PCA	Principle Component Analysis
PDF	Probability Density Function
PDM	Point Distribution Model
POP	Partially-ordered Potts
QR	Quadratic Regularization
RANCOR	Registration via Convex Relaxation
RF	Random Forest
RMSE	Root-mean-squared Error
ROI	Region of Interest
RV	Right ventricle, Right-ventricular
RVOT	Right-ventricular Outflow Tract
SAX	Short-Axis
SD	Standard Deviations
sGM	Subcortical Gray Matter
SI	Signal Intensity
SPM_D	Statistical Parametric Mapping DARTEL Toolbox
SSFP	Steady-state Free Precession
SSM	Statistical Shape Model
STRM	Signal-Threshold-To-Reference-Mean
SVM	Support Vector Machine
T1w	T1-weighted

TI	Inversion Time
TO	Target Overlap
TOF	Tetralogy of Fallot
TVR	Total-Variation Regularization
US	Ultrasound
V	Ventricle
VS	Volume Similarity
VT	Ventricular Tachycardia
VTK	Visualization Toolkit
WM	White Matter
WML	White Matter Lesion
WH	Whole-Heart

Chapter 1

An Introduction to Medical Image Segmentation

The introduction of computerized methods to the acquisition of medical images in the last half of the 20th century facilitated the non-invasive mapping of the human anatomy. Magnetic resonance imaging (MRI), computed tomography (CT), ultrasonography (US) and many other imaging modalities are nowadays in routine clinical use to diagnose diseases, plan and guide interventions, model morphologies, etc...

As stated in the early 2000's [1], the growth in size and number of these images necessitate the use of computers to facilitate processing and analysis. With recent technological advances, the scale of the data has increased due to improved spatial resolution and the ability to acquire volume series temporally. This increase has led to improvements in the ability to resolve pathological phenomena and diagnose disease at earlier stages faster and with higher accuracy. However, the increase in data demands robust and efficient means of automatically identifying anatomical structures or pathologies for diagnostic purposes.

We define the task of extracting one or more objects of interest from an image as segmentation. In this chapter, an introduction to medical image segmentation is given to provide the reader with a historical and theoretical foundation in segmentation, on which the terminology

and methods proposed in Chapter 2 to 5 rely.

1.1 The image as a function

Let us adopt the definition of a medical image volume from Birkfellner [2] as a discrete N-dimensional (ND) mathematical function storing physical phenomena of the imaged anatomy as gray values in smaller volume elements, called voxels (vx).

1.2 What is a segment?

Segmentation problems are commonly defined over the image domain Ω, where Ω is partitioned into non-overlapping regions, or segments, S [1]. For K regions, determining the sets or objects $S_k \subset \Omega$ within the image domain, such that

$$\Omega = \bigcup_{k=1}^{K} S_k \,, \tag{1.1}$$

i.e. the union of regions making up the entire image domain and none of the sets S_k and S_j overlap:

$$S_k \cap S_j = \emptyset; \; for \, k \neq j \,. \tag{1.2}$$

The segments S_k can represent objects such as anatomical structures, cavities and pathological phenomena. We distinguish objects or regions of interest as foreground from non-relevant regions, the background. In the simplest case, the binary segmentation problem ($k = 2$), we aim at distinguishing a single object of interest S_{FG} from the rest of the image domain Ω, the background S_{BG}. In a multi-region segmentation problem, where there can be several foreground and background objects, we do not necessarily distinguish between them and simply refer to them as objects.

We represent all segments as a proper discrete mathematical function with dimensionality and size of the image domain Ω we derived it from, called a label map. The label map represents a segmentation of the image and each object is represented by a pre-defined integer value (i.e. for multi-region segmentation a segmentation with K segments will typically contain integer values from $L(x) = k, if x \in S_k$.

1.3 Clinical rationale

Image segmentation in the clinical practice is widely used as a tool to quantify information about the anatomy and function of a patient. It can range from simple applications, such as measurement of tissue volumes [3, 4] to determine whether the patient's anatomical and physiological parameters lie within or outside normal ranges, to complex disease classification procedures, where human interpretation of the images is not feasible. A common purpose of segmentation methods is to locate and quantify pathologies [5, 6, 7, 8] and use the additional information to aid diagnosis [9, 10, 11, 12]. Imaging and image-based quantification of anatomical structures allow us to model morphology of the human and better understand human development [13, 14] and underlying pathological processes [15, 16, 17].

Further, segmentation of medical images can be frequently found in interventional work flows to facilitate measurements for surgical planning [18], modelling of pre-operative data [19, 20] or use during image-guided interventions [21, 22, 23], in particular for surgical navigation [24, 25].

Lastly, the generation of representative virtual models of the human anatomy is required for virtual surgery simulation [26, 27, 28], where novice interventionists are able to develop skills and master new techniques before applying them in the operating room.

1.4 Medical Image Segmentation Techniques

Similar to other fields, new techniques in medical image segmentation have been developed over time to address new problems or to overcome limitations of previous methods. We attempt to categorize commonly found techniques into two groups and review developments within each group to better explain the choice of methods used in Chapters 2-5. Medical image segmentation techniques can be split into two major tracks: I) boundary-based and II) voxel-based segmentation techniques. This is not a perfect split. Methods have been developed which take aspects of both tracks, but these tracks allow for the progress of segmentation research in the past two decades to be more readily described.

1.4.1 Boundary-based image segmentation techniques

Initial attempts in medical image segmentation include methods based on evolving boundaries from an initial set of labelled voxels to a boundary delineating an object of interest. In this section we review some of the most commonly used techniques for segmentation and elaborate on the limitations that motivated further development.

Region-growing

In the 1990's, region-growing, in particular seeded region growing, was a widely clinically used method due to its simplicity in computation and its generality in application. One of the initial studies [29] describes an algorithm growing a region from an initial seed to an object of interest. Given an initial region, or seed, at each iteration the boundary voxels, are compared with respect to their similarity with their neighbouring voxels and if there is a high similarity with the boundary voxel, the region grows to include similar neighbours for the next iteration [29],

$$T = \left\{ x \notin \bigcup_{n=1}^{n} A | N(x) \cap , \bigcup_{n=1}^{n} A \neq \emptyset \right\} \tag{1.3}$$

where $A_0, A_1 \ldots A_n$ are the current seeds and T is the set of not allocated voxels bordering at the current seeding region and $N(x)$ the neighbourhood around voxel x. Typically, within a volume, 6- or 26-connectedness is employed. A similarity measure δ is defined to identify which neighbours in $N(x)$ are assimilated to the region A_i. A simple and commonly used metric for δ is the absolute value of differences of the voxel intensity, $g(x)$, and the mean of the region A_i:

$$\delta(x) = |g(x) - \underset{y \in A_i(x)}{\text{mean}} [g(y)]| . \tag{1.4}$$

This metric ensures that A_i adopts similar neighbouring voxels and grows to delineate a region of interest with uniform intensity. The method is widely used in clinically motivated studies and variants and adaptation can be found in abdominal [30, 31, 32, 33], cardiothoracic [34, 35], vascular [36, 37, 38], neurological [39, 40], musco-skeletal [41], and mammography [42, 43] applications.

A major limitation of this technique is that regions of interest can have very similar intensity distributions (i.e. muscle tissue and blood in CT have very similar Houndsfield units and so are not even visually distinguishable). If two anatomical structures share a boundary and the same intensity distribution, the growing region will 'leak' into undesirable regions. If the regions have uniform intensities and clear boundaries, region-growing can be a parameter-free and quick solution to many segmentation problems.

Many improvements have been proposed to overcome limitations of this method, such as dependence on raster-order processing [44], extension to volumes specifically for medical image segmentation [45], multi-spectral data [46], inclusion of homogeneity criteria [47], etc... However, leaking remains a major limitation of this method, promoting the inclusion of boundary or smoothness costs into methods.

Active Contour Models

Active contour models (ACM) or *snakes* [48] are techniques to evolve a spline towards an optimal region, by minimization of an energy. This energy combines information about the image or from the user, so-called *external forces* with information derived from the contour itself, the *internal forces*. It evolves from an initial position to a state of minimal energy, where the snake evolution is often optimized via gradient descent. As described in [48], we can formulate the snake parametrically as $v(s) = (x(s), y(s))$ and the associated energy E_{snake} along the spline s, such that,

$$E_{snake}* = \int_0^1 E_{snake}(v(s))ds = \int_0^1 \underbrace{E_{int}(v(s))ds}_{\text{Internal forces}} + \underbrace{E_{image}(v(s))ds + E_{con}(v(s))ds}_{\text{External forces}}, \tag{1.5}$$

E_{snake} is a summation of the *internal* and *external* forces. E_{int} is defined as

$$E_{int} = \left(\alpha(s)\left|\frac{dv(s)}{ds}\right|^2 + \beta(s)\left|\frac{d^2v(s)}{ds^2}\right|^2\right)/2, \tag{1.6}$$

where $\alpha(s)$ and $\beta(s)$ are weights for the first order and second order terms, respectively. The first order term enforces membrane-like behaviour and the second makes the snake behave like a thin plate [48]. The snake evolves to a lower energetic state by minimizing E_{snake}. This can be done via local optimization methods such as gradient descent. We note that through modifying E_{int} by adjusting α and β we can enforce some kind of regularization to the region the snake delineates, avoiding 'leaking' into undesired regions.

E_{image} encourages the snake to adhere to edges in the image, a simple example could be $E_{image} = -|\nabla I(x, y)|^2$, where $I(x, y)$ is the image intensity. E_{con} represents contraction forces of the snake, which penalize or encourage growth. One example is the constant length penalty, $E_{con} = \gamma|\frac{dv}{ds}|$, where γ is a constant.

A major disadvantage of using snakes for applications in medical imaging is that the snake

often gets stuck in local minima and does not converge properly to the object of interest. More recent developments aimed at addressing these problems, such as *Gradient Vector Flow Snakes* [49]. Also, additional forces have been employed as in *Balloon Snakes* [50] or incorporation of statistical models in *Diffusion Snakes* [51]. An inherent limitation of classical snakes is that the formulation does not allow a change in topology, i.e. the snake cannot split to segment non-connected segments. *T-Snakes* [52] aim at overcoming the inherent limitation of a snake, however, more advanced representations of curves, such as *level-sets* are nowadays commonly employed.

In spite of these limitations, snakes, due to their simplicity in implementation and use, are often found as a solution to medical image segmentation problems [53]. Lastly, we highlight the implementation of a 3D ACM in the open-source segmentation software *ITK-SNAP* [54] (*http://www.itksnap.org/*), which is also a powerful tool to generate manual segmentations.

Statistical Shape Models

Since the introduction of Active Shape Models (ASM) in 1995 [55] and of Active Appearance Models in 1998 by Cootes et al. [56], *Statistical Shape Models (SSM)* are widely established in medical image segmentation. *SSMs* model shapes by statistically analyzing point sets from a series of annotated training data. A recent review from Heimann and Meinzer [57] gives an excellent introduction to developments on *SSMs* and is taken as a basis for this section.

Construction of SSMs

A shape can be represented as a set of landmarks or points distributed on a surface of an object of interest. The term Point Distribution Model (PDM) [58] is frequently used interchangeably with landmarks. A requirement for construction of an *SSM* is the availability of corresponding landmarks across training datasets for statistical analysis. The construction of an *SSM* consists of extraction of a mean geometry of a shape and several statistical modes of variation within the geometry.

Spatial Alignment

Shape is defined as a property that is invariant to similarity transforms, i.e. invariant to translation, rotation and scaling [57]. Creating a mean shape representation consist of alignment of all training landmarks in a common coordinate frame. This can be done via generalized Procrustes analysis [59, 60] and the well-known iterative closest point algorithm [61], which minimizes the squared distance between two point sets analytically.

Dimensionality Reduction

The aligned sets of corresponding points is then subject to dimensionality reduction to extract the most descriptive set of modes for the variation of points in the *SSM*. Assuming a Gaussian distribution, we can use Principal Component Analysis (PCA) to extract these modes and order them by their variances. Approximate retrieval of each individual shape can then be done via linear combination of these modes. In order to constrain the variation each mode has to be limited to a valid range of parameters, commonly ± 3 standard deviations.

Segmentation using ASMs

In most cases in medical image analysis, an *SSM* is used to segment new image data. For this purpose, Cootes et al's [55] employed ASMs initially used a gradient-based term as appearance model to drive the segmentation, however soon after introduced AAMs [56] to incorporate more advanced appearance models.

Limitations

While *SSM*s are known to be robust for many segmentation problems, a general disadvantage is the requirement of large training databases to cover all variations in geometry. Additionally, the robust identification of such landmarks in a new subject image can be challenging, even when user interactions are employed [57].

Level sets

Initially introduced for shape tracking [62], *level set methods (LSM)* were adapted in the field of image segmentation, because of inherent advantages of the formulation in the evolution of surfaces, in particular overcoming limitations of *ACMs*, when changes in topology are required.

As mentioned previously, the classical formulation of *ACMs* does not allow the contour to split and merge as it is often required by segmentation problems. As in [63], the *LSM* formulates the contour γ as a zero level set of the higher-dimensional level set function ϕ, such that

$$\gamma = \{ x \in \Omega \,|\, \phi(x) = 0 \}, \tag{1.7}$$

and the region membership is determined by the sign of the level set function ϕ [63]:

$$R_{Object} = \{ x \in \Omega \,|\, \phi(x) > 0 \} \tag{1.8}$$

$$R_{Background} = \{ x \in \Omega \,|\, \phi(x) < 0 \} \tag{1.9}$$

The contour γ as the zero level set can then be evolved over time t via

$$\frac{\partial \phi}{\partial t} = V|\nabla \phi|, \tag{1.10}$$

where V is a designed velocity or speed function to evolve γ throughout the image domain. We note that through this implicit formulation γ is able to readily change its topology and so address a far wider range of segmentation problems.

With increasing data and its dimensionality, the computation of the curve evolution via the *LSM* becomes increasingly expensive. Many approaches to optimize implementations, such as using a narrow-band [64], sparse field [65] *LSM* representations have been introduced to improve computational efficiency. Due to their tendency to incorrectly converge to local optima, iterative max-flow methods have been studied and compared against LSM for evolution of surfaces [66]. In particular, evolution methods directly relying on flow-maximization allow a substantial reduction in evolution steps to convergence and allow fast GPU-based implementations have been subject of recent research [67]. Due to the popularity of *LSM*s, several comparative studies and surveys describe and review improvements for *LSM*s in the recent past

[68, 69, 63].

Because of their inherent advantages, *LSM*s are widely used in medical image segmentation and are frequently found in complex problems, such as segmentation of the left [66, 70, 71, 72] and right ventricles [73, 74, 75] in cardiac diagnostics and neuroimaging applications [76, 77, 78, 79].

1.4.2 Voxel-based image segmentation techniques

Thresholding

The simplest of all segmentation techniques is the binarization by a threshold, i.e. the partitioning of the image domain by its intensity $I(x)$ via the threshold T, such that

$$g(x) = \begin{cases} 1, & \text{if } I(x) > or < T. \\ 0, & \text{otherwise.} \end{cases} \tag{1.11}$$

where $g(x)$ is the segmentation result. This concept can of course be extended to threshold within two bounds to extract regions. This is particularly helpful in situations where the employed modality is able to image the object of interest with high contrast, such as bony structures or air compartments in CT [80], structures with acoustic impedance in US [81] or post-enhancement imaging in cardiac MRI [82]. A widely referenced survey article on thresholding techniques can be found in Sahoo et al [83].

Thresholding is also applied to images with multiple channels [84], as in color photographs, where a threshold is employed on each channel separately and then combined by computing the intersection of all thresholded channels. This concept can be readily employed in medical images, such as those from multiple MRI sequences, dual-energy CTs or digital histo-pathological scans.

Often a threshold T is determined via user interaction, by interactively varying T until the result is satisfactory. This however, introduces a potential bias from the operator, which has

to be separately assessed on its robustness. Automated approaches include the well-known Otsu's method [85] or agreed standards such as the Full-Width-At-Half-Maximum (FWHM) method [86]. The latter appears frequently in the segmentation of myocardial scar from Late-enhancement cardiac MRI and it and other methods are constantly subject to comparative performance analyses [82].

Clustering

A sub-field of algorithms in image segmentation is based on cluster analysis methods. Clustering methods aim to partition sets of objects in observed data into groups, such that each object in a group is more similar to each other than to those in other groups. In particular, methods using centroid-based and distribution-based clustering models appear frequently in medical image segmentation pipelines. In this section we briefly review three clustering methods: the *k-means* algorithm, *fuzzy c-means* and *expectation-maximization*.

K-means clustering

The standard algorithm MacQueen [87] introduced as *k-means* is also known as Lloyd's algorithm [88] and aims at partitioning n objects x the set $S = S_1, S_2, ..., S_k$ into k partitions, such that

$$\arg\min_{s} \sum_{i=1}^{k} \sum_{x_j \in S_i} \left\| I(x_j) - \mu_i \right\|^2 , \tag{1.12}$$

where μ_i is the mean intensity of objects in S_i. *K-means* clusters the objects into k sets, such that the L2-norm of each object towards the mean is minimized. We choose k initial means μ_i and assign all objects to each mean according to shortest distance. In a second step, we update all means μ_i to the mean of all assigned objects. The algorithm iteratively assigns and updates the sets S until no points are re-assigned. Note that the resulting partitioning is dependent on the initially set means μ, which are assigned randomly. Different initialization procedures were proposed by several studies [88, 89] to obtain more consistent results.

Fuzzy c-means clustering

The *fuzzy c-means* [90, 91] algorithm operates similarly to *k-means* and models the relationship of objects probabilistically, where each objects is assigned a membership weight w of belonging to a cluster. Similarly to *k-means*, the update step re-assigns cluster centres μ, but under consideration of their membership weights w. The assignment step then adjusts the membership weights, where m is a fuzzyfying parameter that determines cluster fuzziness:

$$\mu_k = \frac{\sum_x w_k(x)^m I(x)}{\sum_x w_k(x)^m} \,. \tag{1.13}$$

A good algorithmic comparison can be found in [92, 93] and several approaches in medical image segmentation employ this algorithm [94, 95, 96]

Expectation maximization

In contrast to the centroid or mean-based cluster analysis as the *fuzzy c-means* or *k-means* algorithms, the *expectation maximization* algorithm [97] is a distribution-based clustering method that models a fixed number of Gaussian distributions and, as the above methods, is iteratively optimized to fit the observed data. Similar to the *fuzzy c-means* approach it returns a fuzzy result, which can be discretized according to the most likely Gaussian. This algorithm has demonstrated better robustness towards the random initialization than *fuzzy c-means* [1]. A good tutorial on the method can be found at Western University's Computer Science Department [98] and published review papers [99, 100]. Due to its generality and the improved robustness it has been frequently appearing in medical image segmentation literature [101, 102, 103, 104, 105, 106, 107, 108].

Classifiers

A classifier partitions a feature space into sub-populations of given labelled training data [109, 1]. In medical image segmentation such a feature space is commonly derived from image intensities, either from a single intensity dimension (i.e. filters encoding neighbourhood information, gradients, etc) or multiples (i.e. dual CT energies, multiple MRI sequences, pre- and post-contrast enhancement imaging, etc), but can also contain binary or categorical measures.

The general dependency on available training data makes classifier-based pipelines supervised segmentations methods.

K-nearest neighbours

The *K-nearest neighbour (KNN)* algorithm [110] is a simple and parameter-free classification method, where a sample s is assigned a class according to majority vote of the $k \in \mathcal{Z}^+$ nearest neighbours in the feature space. Typically, the Euclidean distance is used to determine the closest samples and the k training samples can be weighted in their contribution to the vote by it. It is often employed together with dimensionality reduction techniques, such as *principal component analysis* if the distance to the nearest neighbours is too large due to the high dimensionality of the feature space, i.e. the majority of training samples are equidistant [111].

Support vector machines

Classification mechanisms employing *Support vector machines (SVM)* [112] aim at constructing a set of hyperplanes in N-dimensional (ND) feature space to partition this space into two sets of ND samples, that maximizes the distance of each ND sample to each of the (N - 1) dimensional hyperplanes, respectively. It was originally proposed to be a linear classifier and extended to be able to solve non-linear classification problems by operating linearly in a transformed feature space, which might result in non-linear classification in the original feature space [113].

Multi-class problems are commonly addressed by a series of binary classification problems and several proposed strategies [114, 115] can be found as solutions medical image segmentation problems [116, 117, 118].

Artificial Neural Networks

The term *Artificial Neural Networks (ANN)* summarizes loose group of methods simulating biological learning via parallel networks of nodes [1, 119]. Approaches in image segmentation employ *ANN*s as classification methods [120, 121] in a supervised manner, i.e. learning on how to segment new patient data based on a training sample. Alternatively, *ANN*s can be used in an unsupervised manner, as clustering methods [122, 121, 1].

Decision Trees and Random forests

Decision Trees (DT) are trained predictive models that in a segmentation setting aim to classify each voxel according to some input features, where the leaves of the tree represent the label or category, respectively. If more than one tree is involved in the classification, i.e. several *DT*s are trained on subsets of the initial training data, we term this a 'forest'.

Recently, *Random Forests (RF)* classifiers [123, 124, 125] have gained attention in medical image segmentation [126, 127, 128, 129], where the initial training data is randomly split into sub-samples for building the *DT*s. A particular advantage of this method is, that via the randomization it is able to prevent over-fitting to the training data, i.e. it does not excessively adapt to the training information and fail to classify new data. The gained robustness make *RF* a preferred classifier particularly in medical segmentation problems.

Markov-Random Field Models

Markov random field (MRF) modelling is a probabilistic method commonly used together with other segmentation methods modelling spatial interactions between voxels and regularizing segmentations to obtain more contiguous results. The *MRF* models image domain as an undirected graph where all voxels are represented as vertices and the neighbourhood interactions are modelled using edges between these vertices.

This is of particular importance in voxel-wise methods, such as clustering and thresholding, where local intensity inconsistencies, such as noise or artifacts from acquisitions can cause small spurious regions [1]. Particularly in combination with fuzzy clustering methods [130, 131], where probabilistic results can be directly modelled as an objective function, the use of *MRF* is often modelled with a Bayesian prior maximizing the a posteriori probability [132]. This approach is also frequently found in multi-atlas-based segmentation methods, where registered atlas label need to be regularized and fused simultaneously [133, 134].

While *MRF* methods been valuable in the above applications, they nevertheless require computationally expensive solvers, which becomes even more challenging with an increase in

data.

1.5 Max-Flow-based Segmentation Techniques

With the introduction of *MRF*s as regularization mechanisms for image segmentation, graphical methods found their way into the field of medical image segmentation. In particular, graph cuts, i.e. the partitioning of graph vertices into disjoint sub-sets, have gained attention in the recent years, as dual (or mathematically equivalent) formulations have emerged in the field to directly solve complex energy minimization problems efficiently.

In the field of computer vision, graph cuts are mainly employed to solve a variety of low-level vision problems that can be formulated as an energy minimization problem [135]. This includes regularized image segmentation, stereo vision and smoothing problems. Here, we mainly focus on image segmentation and introduce the *max-flow/min-cut* theorem to ease the reader into different max-flow-based segmentation methods.

Given the image domain Ω, every voxel $v \in \Omega$ must be assigned a label in some finite set $\mathcal{L}$. The goal is to find a labelling f that assigns each voxel $v \in \Omega$ a label $f_v \in \mathcal{L}$. We formulate a problem as an energy to be minimized,

$$E(f) = E_{data}(f) + E_{smooth}(f)\,, \tag{1.14}$$

where the total energy to be minimized consists of an energy data term, measuring the disagreement of f and the observed data and a regularization term E_{smooth}, that measures the extent of smoothness [136]. The data term E_{data} in image segmentation is commonly formulated as

$$E_{data}(f) = \sum_{v \in \Omega} D_v(f_v)\,, \tag{1.15}$$

where D_v measures, how well f_p fits the voxel v given observed data [136]. Figure 1.1 depicts an artificial 3x3 pixel color image, from which we can derive an example data term D_v.

A very simple D_v could be the L1 norm from an observed mean of an object of interest, i.e $D_v = |\mu - I(v)|$, where $I(v)$ is the image intensity at the voxel v and the observed mean μ is known or calculated from a sample of the object.

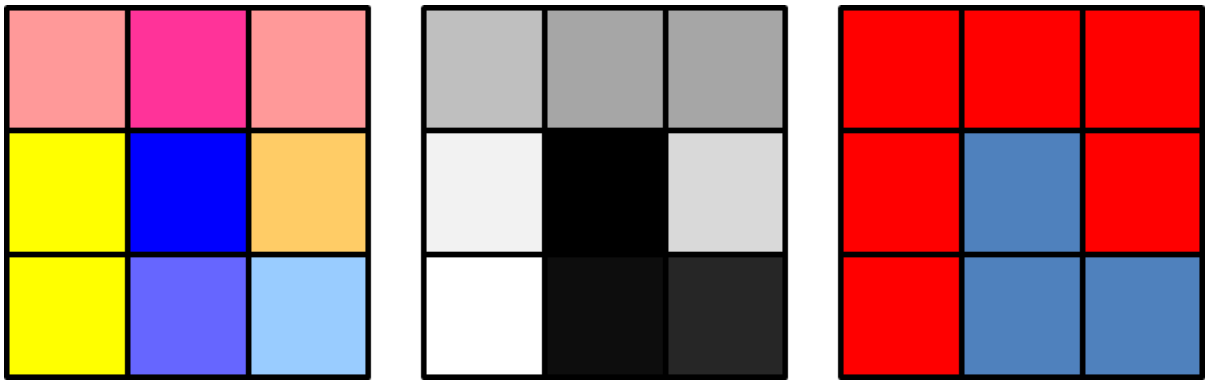

Figure 1.1: An artificial example of a 3x3 pixel color image (left), associated data term D_v (middle) and obtained segmentation result (right).

1.5.1 Binary graph cuts

In the early 2000's Boykov and Kolmogorov [135] popularized the use of graph cuts in medical image segmentation, by proposing an efficient dual algorithm for an energy minimization, considering an energy in the form of

$$E(f) = \underbrace{\sum_{v \in \Omega} D_v(f_v)}_{E_{data}} + \underbrace{\sum_{\{u,v\} \in \mathcal{N}} V_{u,v}(f_u, f_v)}_{E_{smooth}}, \tag{1.16}$$

where $\mathcal{N}$ is the set of interacting pairs of voxels v and u, often a neighbourhood. We note that the terms in (1.16) are associated with the general energy formulation in (1.14).

Commonly in image segmentation, each vertex V in the graph $G = V, E$ represents a voxel and the edge E model the pairwise voxel interactions in 6-connected neighbourhood N. Additionally, two specialized nodes (in the binary segmentation case), called terminals, the source s and the sink t, are connected to each vertex V. These terminals correspond to a set of labels [135].

The graph associated with the example in Figure 1.1 is shown in Figure 1.2 (left). Note, how the data term D_v in Figure 1.1 (middle) is expressed as capacities of the source and sink connections.

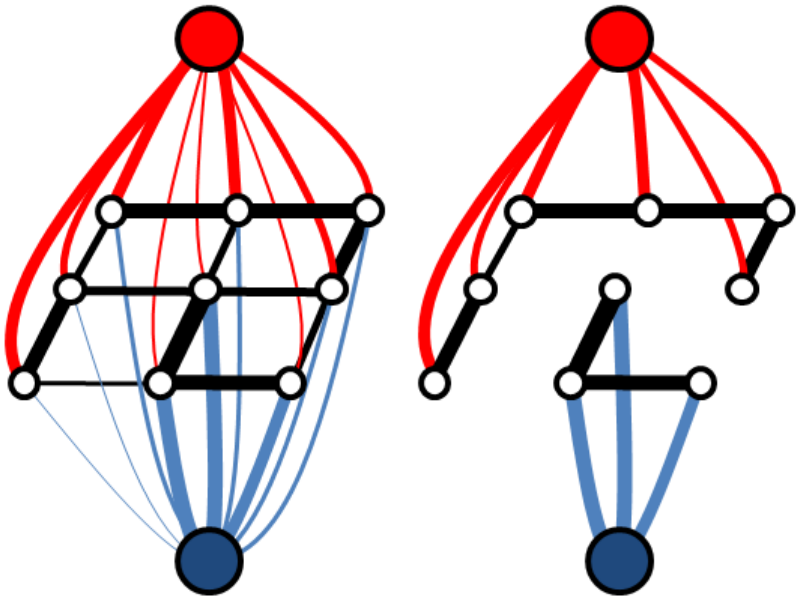

Figure 1.2: Corresponding graph to the segmentation problem in Figure 1.1. The source (red) and sink (blue) nodes and the graph vertices V (black) are connected to a flow network (left). A graph cut (right) is achieved by removal of edges, such that no flow can flow from the source to the sink and the removed edges sum up to a minimum.

Solvers aim at partitioning the graph into two sets of vertices, so that there is no connection between the source and the sink, by finding the minimum cut cost through all connected edges. This problem is called a *min-cut* problem and is commonly solved over a (computationally advantageous) dual, i.e. a mathematically equivalent formulation. The *min-cut/max-flow* theorem, independently proven in 1956 by Elias et al [137] and Ford and Fulkerson [138], states that in a flow network as the graph G, computing the *maximum-flow* throughout the network is dual to the computation of *minimum-cut*.

Dual formulations are commonly computationally less expensive and allow for implementation of inexpensive solvers to such complex problems. Ford and Fulkerson proposed the *augmenting paths algorithm* [138] to solve the max-flow problem and are followed by many others including the well-known *push-relabel* [139] algorithms.

An important advantage of such energy minimization via *max-flow* is, that the resulting segmentation is (approximately) globally optimal and so overcomes a limitation of many contour propagation methods (*LSM*, *ASM*, etc), which converge to local (and potentially incorrect) optima.

However, there are several drawbacks to such discrete, graphical approaches: i) algorithms need to load the graph $G = V, E$ into the memory, which can be extensive in volume images; ii) the setup of the graph with 6-connected neighbourhood N causes inherent metrication artifacts. This might be overcome by increasing the neighbourhood layout to resemble a sphere, i.e. 26-connectedness [140], but will result in an even higher memory load; and iii) the formulated pair-wise voxel interactions in E_{smooth} can cause elongated structures to shrink. This is particularly undesirable in many medical segmentation problems dealing with elongated objects, such as vasculature, airway trees, nerve fibres, etc.

Applications of graph cuts in medical image segmentation are frequently found in a wide spectrum of applications, particularly where probabilistic costs are employed, such as interactive [141, 142, 143] and atlas-based methods [133, 144, 145].

1.5.2 Continuous Max-Flow

An inherent disadvantage of discrete max-flow methods, such as [136, 135], is the appearance of metrication artifacts in resulting labellings. This is due to the fact that the pair-wise interaction potentials penalize more strongly along the component directions of the graph than in other directions. Because of this, recent studies have proposed to solve this energy minimization problem in continuous space, where this limitation does not exist. While the idea of continuous max-flow was first introduced by Strang [146, 147], we focus our attention on the method presented in Yuan et al [148], from which the methods in Chapters 2-5 evolved from.

Yuan et al. [148] introduced the continuous counterpart of the discrete max-flow model, the continuous max-flow and proved its duality to the continuous min-cut model.

$$\min_{S} \underbrace{\int_{S} C_s(x)dx}_{\text{source terminal connections}} + \underbrace{\int_{\Omega/S} C_t(x)dx}_{\text{sink terminal connections}} + \underbrace{\int_{\delta S} C_e(x)dx}_{\text{object boundary}}, \tag{1.17}$$

where C can be seen as the flow capacity of the voxel. This is analogous to the discrete max-flow formulation, where we build a graph $G = V, E$ of vertices V and a set of edges E, where each vertex v is connected via spatial edges e. Again we connect all x (analogous to v) to two specialized terminals, the source s and the sink t, via the terms $\int_S C_s(x)dx$ and $\int_{\Omega/S} C_t(x)dx$ respectively [148]. The weighted object boundary is analogous to the edges cut from E, but reformulated for the continuous domain.

As with the discrete case, this problem can be addressed as the dual of a flow maximization problem:

$$\max_{p_s, p_t, p_e} \int_{\Omega} p_s(x)dx \tag{1.18}$$

through a flow network subject to constraints, such as a capacity constraint of the flow p_s and p_t passing the source and sink connections respectively,

$$\begin{aligned} 0 \leq p_s(x) \leq C_s(x) \\ 0 \leq p_t(x) \leq C_t(x) \end{aligned} \tag{1.19}$$

and capacity constraints of spatial flows p_e:

$$|p_e(x)| \leq C_e(x), \ . \tag{1.20}$$

Further, in each node x the flow is conserved such that all incoming flows and all outgoing flows are balanced,

$$\underbrace{\operatorname{div} p_e(x)}_{\text{spatial flows}} - \underbrace{p_s(x)}_{\text{source flows}} + \underbrace{p_t(x)}_{\text{sink flows}} = 0, \tag{1.21}$$

The flow-maximization problem is solved via convex relaxation, where all imposed constraints

are formulated as augmented Lagrangian functions. After convergence, the resulting segmentation is obtained via the continuous labelling or indicator function $\lambda \in [0, 1]$, which can be thresholded to obtain binary result $\{0, 1\}$.

A major advantage of this method is that large parts of the max-flow method is inherently parallel, which suggests its implementation on parallel computation architectures, such as CUDA (NVIDIA Corp, Santa Clara, CA) or OpenCL (Khronos Group, Beaverton, OR) via GPGPU. Such implementations allow for substantial improvements in run times on inexpensive, commercially available graphics hardware, where even real-time performance on volume images is feasible [149].

1.5.3 Potts Model to Multi-Region Segmentation

Initially proposed in statistical physics [150] to describe interaction of spins in a lattice, the *Potts model* gained attention in image and signal processing. It can be used to describe the minimization problem of multi-region partitioning in image segmentation [151, 136, 152] and reduces itself to a binary problem when used with two labels. For three or more labels the problem is NP-hard. NP stands for *non-deterministic polynomial-time* and is used to describe problems where a provided solution can be verified in polynomial time, i.e. verification is computationally feasible, even if finding such a solution to verify is not. NP-hard describes the class of problems that are at least as hard as any NP problem, and the existence of exact solver for any problem in this class is unknown. Instead of computing the exact solutions, global optimum to the Potts problem can be approximated [136]. Yuan et al. introduced a dual max-flow solver to the continuous *Potts model* problem [152], possessing the same favourable advantages as the continuous binary solver [148]: It avoids metrication artifacts and can be readily implemented using GPGPU to create a fast (approximately) globally optimal solver for image segmentation problems.

Analogous to the binary formulation, the energy in a continuous multi-region case can be

formulated as,

$$\min_{\{\Omega_i\}_{i=1}^n} \underbrace{\sum_{i=1}^{n} \int_{\Omega_i} D(l_i, x)dx}_{\text{Data term}} + \underbrace{\lambda \sum_{i=1}^{n} |\partial\Omega_i|}_{\text{Regularization term}} , \tag{1.22}$$

subject to,

$$\cup_{i=1}^{n} \Omega_i = \Omega \,\text{and}\, \Omega_k \cap \Omega_l = \emptyset,\ \forall k \neq l\,, \tag{1.23}$$

where Ω is the image domain to be partitioned into n segments, $D(l_i)$ is the data penalty term for label i and λ the parameter to weight the contribution of the regularization term to the total energy. The perimeter of each segment can be computed by

$$|\partial\Omega_i| = \int_{\Omega} |\nabla u_i| dx,\ i = 1...n \tag{1.24}$$

and the *Potts model* energy from (1.22) rewritten to

$$\min_{u_i(x)\in\{0,1\}} \sum_{i=1}^{n} \int_{\Omega} \{\underbrace{u_i(x)D(l_i, x)}_{\text{Data term}} + \underbrace{\lambda|\nabla u_i|}_{\text{Smoothness term}} \} dx, \tag{1.25}$$

subject to (as in (1.23))

$$\sum_{i=1}^{n} u_i(x) = 1 \,\text{and}\, u_i(x) \geq 0,\ \forall x \in \Omega\,, \tag{1.26}$$

according to [152].

The issue of energy minimization of such problem is described in the Appendix of Chapter 2. A recent review of the *Potts model* in both the discrete and continuous space can be found in [153].

1.5.4 Ishikawa model

Another graph configuration to address multi-region problems has been introduced by Ishikawa [154] in the discrete space and recently described in the continuous setting [155]. The *Ishikawa model* allows for a linear ordering to be defined over the labels, such that one label has to be a

subset of predecessor on lower level and can be formulated in the continuous space as,

$$\min_{u_i(x)\in\{0,1\}} \underbrace{\sum_{i=1}^{n}\int_\Omega (u_{i-1}-u_i)D_i dx}_{\text{Data term}} + \underbrace{\sum_{i=1}^{n}\int_\Omega \lambda_i|\nabla u_i| dx}_{\text{Smoothness term}} . \tag{1.27}$$

subject to (as in (1.23))

$$u_0(x) = 1 \text{ and } u_{i-1}(x) \geq u_i(x) \text{ and } u_n(x) \geq 0,\ \forall x \in \Omega\,, \tag{1.28}$$

Such ordering constraints allow to arrange labels in a manner to reflect the topology of anatomical compartments, for example, the whole heart in a volume scan contains the myocardium, which further contains the blood pool. Note, that in comparison with the formulation of the *Potts model*, in (1.25) the *Ishikawa model* has the regularization weight λ indexed per label, allowing for different smoothness on each of the n levels (see (1.27)).

1.5.5 Hierarchical models

In the course of this thesis, we will investigate the ability of flow-maximization methods in the continuous space and the ability to arrange labels to be segmented under similar topological constraints to better segment the anatomy of interest. For this purpose, we will combine aspects of the continuous Ishikawa and Potts problems and extend it to arbitrary labelling hierarchies.

In the course of the following chapters, we demonstrate that such optimization problems can be solved rapidly and be used to address open segmentation problems of clinical interest.

1.6 Validation of Segmentation Techniques

To evaluate the performance of a segmentation technique, we can differentiate between desired aspects of a proposed method to solve a problem. Generally, newly developed methods attempt to overcome limitations of former methods or are employed on new image data. For this

purpose, we aim to compare newly developed methods in terms of different aspects of performance against existing methods or several variants of proposed methods to establish trade-offs in these aspects.

Compared methods can be validated in terms of accuracy, run time, amount of user interaction required, robustness towards initialization, size of a training database or stability and range of employed parameters. Definitions of performance in each of these aspects is entirely dependant on what is clinically required and in most cases expert users determine what is an acceptable range of performance.

In these sections, we will introduce metrics to quantitatively compare methods within an experimental trial and consider caveats of employing them for different segmentation problems.

Gold standard

A gold standard method can be considered a benchmark to test against, however actual ground truth knowledge is often not available. Over time, it has been established that a gold standard method is not the perfect test, but the best one available [156]. In particular in medical imaging, this gold standard is an expert interpretation of an image in the form of a manual annotation. This can be in the form of anatomical landmarks to be identified, classification of diseases from images or, as commonly found in the image segmentation literature, label maps resulting from manual segmentations.

Run times

Run times are a crucial aspect within the clinical work flow. Especially, time sensitive problems that often arise in interventional therapies, require special solutions to be applicable, however any study can potentially benefit from improvements in run times to overcome limitations of use.

When assessing a module of a pipeline, partial and total run times can be stated and quantitatively compared, when configured using hardware with the same specifications. Compu-

tational complexity, convergence rates or different initializations can cause differences in run times and worst cases have to be assessed to estimate computation time of an experimental design. Different paradigms on implementation, such as user interactions or computation using parallel architectures, have a substantial influence on pipeline execution times and can largely contribute to the clinical feasibility of a methodology.

Accuracy

For accuracy validation of a new method, we aim to compare it against a gold standard method by computing one or more metrics and resulting mean scores of them. In the literature, the accuracy of a segmentation method is determined in its score against a gold standard benchmark in terms of a specific metric. Such a validation metric allows the accuracy of a segmentation to be quantified, subject to limitations. For this purpose, we commonly complement metrics measuring different aspects of the segmentation to get a more holistic assessment of the performance.

We can categorize metrics measuring different aspects of accuracy into three groups: Regional metrics, often determining an overlap ratio of a computed region A with the Gold standard region B, distance-based metrics, describing an distance error of the contour or surface of region A and B, and volume-based metrics, comparing resulting volumes of the two regions. In particular, volume-based metrics are commonly found in the clinical literature.

Regional metrics

There are three commonly employed overlap metrics to evaluate an algorithm-generated region R_A with that of a gold standard region R_G and obtain a fraction of overlap:

Target overlap (TO) [157] ratio:

$$TO = \frac{|R_A \cap R_G|}{|R_G|}, \tag{1.29}$$

Dice Similarity Coefficient (DSC) as a mean overlap ratio: [158, 159]:

$$DSC = \frac{2\,|R_A \cap R_G|}{|R_A| + |R_G|}\,, \tag{1.30}$$

and the

Jaccard Index (JI) [160, 159] as a union overlap ratio:

$$JI = \frac{|R_A \cap R_G|}{|R_A| \cup |R_G|}\,. \tag{1.31}$$

While overlap ratio measures are commonly found in the literature, they are limited to be used in comparison between different objects of interest, because of their inherent bias towards volume size, meaning that larger regions generally yield higher overlap ratios than thin, elongated ones.

Distance-based metrics

Distance-based metrics can be calculated from either boundary voxels or vertices generated from surfaces of regions R_A and R_G. To compute the average minimal distance between two regions we employ the *Mean Absolute Distance (MAD)* error in mm.

$$MAD = \frac{1}{N_g}\sum_{i=1}^{N_g} |d(g_i, A)|\,, \tag{1.32}$$

where g_i is the set of gold standard points $\{g_i : i = 1, ..., N_g\}$, $A = \{a_i : i = 1, ..., N_A\}$ the set of the algorithm points and d the Euclidean distance in *mm*.

To assess a worst-case scenario, we can complement the *MAD* results with those of the *Hausdorff distance (HD)*, representing the maximum minimal distance of two point sets:

$$HD = \max_{i\in[1,N_g]} \{|d(g_i, A)|\}, \tag{1.33}$$

However, a maximum state value is a rather unstable measure, as it requires only one voxel per region to be an outlier. To sidestep this limitation, a 95%-ile HD is computed for increased robustness towards outliers.

Volume-based metric

As measured volumes are frequently employed in assisting diagnoses, volume-derived metrics are often computed as a part of validation experiments to evaluate image segmentation methods. The total deviation of R_A from R_G can be computed as real δV_E or absolute volume errors $|\delta V_E|$, or a percentage-wise error δV_P and $|\delta V_P|$, respectively.

Total volume error:

$$\delta V_E = V_A - V_G \tag{1.34}$$

Percentage volume error:

$$\delta V_P = \frac{(V_A - V_G)}{V_G} \times 100\% \,. \tag{1.35}$$

Measured volumes alone do not include information of how well two regions spatially coincide, and merely represent if volume measures derived from the tested segmentation algorithm are associated with those of the gold standard.

Robustness

Robustness is the ability of a processing pipeline to cope with errors during execution and has different impact depending on the application. For segmentation algorithms employed within interventional settings, failure of execution can have a safety-specific ramifications, directly impacting patient care. Within computer-aided diagnostics, incorrectly calculated metrics can cause misdiagnosis, or at best an increase in time spent to resolve the issue.

We distinguish between several forms of robustness and can state descriptive statistics in experiments to describe the expected number of outliers on a specific database.

Initialization

Many advanced algorithms require proper initialization to yield acceptable accuracies. This can be in form of user interaction, pre-processing, learning, etc. and the algorithm should be tested for its ability to perform when such conditions are not ideal, as often happens in practice. When clinical performance standards are available, outliers can defined as occurrences of performance outside clinically acceptable margins. As an alternative, outliers determined via descriptive statistics can be stated and potential limitations of methods examined.

Training versus Testing

When a pipeline is dependent on prior information, such as learning of algorithm-specific parameters, or models from training data, it must be evaluated on an independent testing dataset. Statistical significant differences in for accuracy metrics can indicate learned elements were over-fitted to the training data and are not generalizable to other data. Further, the method can be applied the same problem using other data (i.e. acquired from a different scanner, with another acquisition method, from another center or entirely different modality).

Operator variability

Many segmentation algorithms rely on initialization or guidance via user interactions. These are often subject to great variations, depending on training and experience of the operator interacting with the segmentation pipeline and the potential impact on accuracy outcomes has to be assessed. For this purpose, operator variability experiments are conducted to describe the impact on accuracy between and within operators. Intra- and inter-operator variabilities and can be stated via descriptive statistics, such as the *Intra-class correlation coefficient (ICC)* [161] or via the range of one or more accuracy metrics. Measures often employed clinically also include the *Minimum Detectable Difference (MDD)*, Bland-Altman difference plots [162] or the Coefficient of Variation [67].

Range of parameters

Most advanced segmentation methods require a series of parameters to be adapted to a specific problem. Determination of proper parameters is often a complicated problem and subject of research in image segmentation [163, 164]. Parameter ranges used in segmentation pipeline and associated accuracy metrics can be stated to assess the parameters' effect on results [66].

1.7 Thesis Outline

The focus of this thesis is the development of fast and robust segmentation algorithms for use in planning of cardiac resynchronization therapy and characterization of brain tissue. In the methodological Chapters 2-5, I was responsible for conducting experiments, analyses, study design and was the principle contributor to the manuscript. Note that each chapter would not have been possible without the expertise of the many people involved and so within this thesis, I refer not to myself, but the authors or 'we'. This in particularly refers to Chapter 5, where I share the principal authorship with J.S.H Baxter, who contributed equally to the contents of that chapter.

Chapter 2 proposes a new interactive method to segment myocardial scar tissue from Late-Enhancement (LE) MRI and tests it based on performance, accuracy, and repeatability. It develops the theory of hierarchical flow maximization as an extension to the well-known Potts model in continuous space. This concept is further generalized and applied to brain images in Chapter 5. Chapter 3 aims at comparing quantified scar volumes obtained from clinically established segmentation methods on 2D and 3D LE-MRI acquisitions and assesses the reproducibility of standard clinical approaches on the new 3D LE-MRI data. Chapter 2 is closely based upon a journal article recently published in *IEEE Transactions on Medical Imaging* [7] and Chapter 3 is currently under review in *The International Journal of Cardiovascular Imaging*.

Chapters 4 introduces a new approach to deformable image registration based on total vari-

ation regularization. It develops the theory and compares it against a smooth quadratic regularization method. Both methods are then tested on their accuracy and run times when employed in pair-wise brain registration, a problem occurring in multi-atlas segmentation pipelines. This chapter has been submitted to *IEEE Transactions on Medical Imaging* and is currently under revision.

Lastly, Chapter 5 employs the registration method developed in Chapter 4 within a multi-atlas pipeline to segment brain tissue from multi-channel MRI. It generalizes the theoretical contributions of Chapter 2 and 4 and contributes developed methods back to the community in form of open source software libraries. This chapter is currently under review in *Medical Image Analysis*.

Bibliography

[1] Dzung L Pham, Chenyang Xu, and Jerry L Prince. Current methods in medical image segmentation 1. *Annual review of biomedical engineering*, 2(1):315–337, 2000.

[2] Wolfgang Birkfellner. *Applied medical image processing: a basic course*. Taylor & Francis, 2011.

[3] R Grant Steen, Courtney Mull, Robert Mcclure, Robert M Hamer, and Jeffrey A Lieberman. Brain volume in first-episode schizophrenia systematic review and meta-analysis of magnetic resonance imaging studies. *The British Journal of Psychiatry*, 188(6):510–518, 2006.

[4] R Sacha Bhatia, Jack V Tu, Douglas S Lee, Peter C Austin, Jiming Fang, Annick Haouzi, Yanyan Gong, and Peter P Liu. Outcome of heart failure with preserved ejection fraction in a population-based study. *New England Journal of Medicine*, 355(3):260–269, 2006.

[5] Timothy Spencer, John A Olson, Kenneth C McHardy, Peter F Sharp, and John V Forrester. An image-processing strategy for the segmentation and quantification of microa-

neurysms in fluorescein angiograms of the ocular fundus. *Computers and biomedical research*, 29(4):284–302, 1996.

[6] Ingrid Sluimer, Mathias Prokop, and Bram Van Ginneken. Toward automated segmentation of the pathological lung in CT. *Medical Imaging, IEEE Transactions on*, 24(8): 1025–1038, 2005.

[7] M. Rajchl, J. Yuan, J. White, E. Ukwatta, J. Stirrat, C. Nambakhsh, F. Li, and T. Peters. Interactive hierarchical max-flow segmentation of scar tissue from late-enhancement cardiac MR images. *IEEE Transactions on Medical Imaging*, 33(1):159–172, 2014.

[8] J Stirrat, M Rajchl, L Bergin, T Peters, and JA White. 136 3-dimensional late gadolinium enhancement scar imaging for surgically corrected tetrology of fallot: Clinical feasibility of scar segmentation. *Canadian Journal of Cardiology*, 28(5):S141, 2012.

[9] Theodoros D Karamitsos, Jane M Francis, Saul Myerson, Joseph B Selvanayagam, and Stefan Neubauer. The role of cardiovascular magnetic resonance imaging in heart failure. *Journal of the American College of Cardiology*, 54(15):1407–1424, 2009.

[10] Andrew M Taylor, Sara A Thorne, Michael B Rubens, Permi Jhooti, Jennifer Keegan, Peter D Gatehouse, Frank Wiesmann, Frank Grothues, Jane Somerville, and Dudley J Pennell. Coronary artery imaging in grown up congenital heart disease complementary role of magnetic resonance and x-ray coronary angiography. *Circulation*, 101(14):1670–1678, 2000.

[11] Kunio Doi. Computer-aided diagnosis in medical imaging: historical review, current status and future potential. *Computerized medical imaging and graphics*, 31(4-5):198–211, 2007.

[12] James A. White, Martin Rajchl, John Butler, R. Terry Thompson, Frank S. Prato, and Gerald Wisenberg. Active cardiac sarcoidosis: First clinical experience of simultaneous

positron emission tomography–magnetic resonance imaging for the diagnosis of cardiac disease. *Circulation*, 127(22):e639–e641, 2013.

[13] Adolf Pfefferbaum, Daniel H Mathalon, Edith V Sullivan, Jody M Rawles, Robert B Zipursky, and Kelvin O Lim. A quantitative magnetic resonance imaging study of changes in brain morphology from infancy to late adulthood. *Archives of neurology*, 51(9):874–887, 1994.

[14] Piotr A Habas, Kio Kim, James M Corbett-Detig, Francois Rousseau, Orit A Glenn, A James Barkovich, and Colin Studholme. A spatiotemporal atlas of mr intensity, tissue probability and shape of the fetal brain with application to segmentation. *Neuroimage*, 53(2):460–470, 2010.

[15] A Vita, L De Peri, C Silenzi, and M Dieci. Brain morphology in first-episode schizophrenia: a meta-analysis of quantitative magnetic resonance imaging studies. *Schizophrenia research*, 82(1):75–88, 2006.

[16] F Eckstein, Flavia Cicuttini, J-P Raynauld, JC Waterton, and C Peterfy. Magnetic resonance imaging (MRI) of articular cartilage in knee osteoarthritis (OA): morphological assessment. *Osteoarthritis and cartilage*, 14:46–75, 2006.

[17] Joelle Dennie, Joseph B Mandeville, Jerrold L Boxerman, Scott D Packard, Bruce R Rosen, and Robert M Weisskoff. Nmr imaging of changes in vascular morphology due to tumor angiogenesis. *Magnetic resonance in medicine*, 40(6):793–799, 1998.

[18] Michael W Vannier and Jeffrey L Marsh. Three-dimensional imaging, surgical planning, and image-guided therapy. *Radiologic Clinics of North America*, 34(3):545–563, 1996.

[19] Martin Rajchl, Kamyar Abhari, John Stirrat, Eranga Ukwatta, Diego Cantor, Feng P Li, Terry M Peters, and James A White. Distribution of guidance models for cardiac resynchronization therapy in the setting of multi-center clinical trials. In *SPIE Medical Imaging*, pages 90361V–90361V. International Society for Optics and Photonics, 2014.

[20] Jiro Inoue, Allan C Skanes, James A White, Martin Rajchl, and Maria Drangova. Patient-specific left atrial wall-thickness measurement and visualization for radiofrequency ablation. In *SPIE Medical Imaging*, pages 90361N–90361N. International Society for Optics and Photonics, 2014.

[21] Kevin Cleary and Terry M Peters. Image-guided interventions: technology review and clinical applications. *Annual review of biomedical engineering*, 12:119–142, 2010.

[22] Stefan Hassfeld and Joachim Mühling. Computer assisted oral and maxillofacial surgery–a review and an assessment of technology. *International journal of oral and maxillofacial surgery*, 30(1):2–13, 2001.

[23] Terry Peters and Kevin Cleary. *Image-guided interventions: technology and applications*. Springer, 2008.

[24] J. T. Moore, M. W. A. Chu, B. Kiaii, D. Bainbridge, G. Guiraudon, C. Wedlake, M. Currie, M. Rajchl, R. V. Patel, and T. M. Peters. A navigation platform for guidance of beating heart transapical mitral valve repair. *IEEE Transactions on Biomedical Engineering*, 60(4):1034–1040, 2013.

[25] Feng P Li, Martin Rajchl, John Moore, and Terry M Peters. Ultrasound based mitral valve annulus tracking for off-pump beating heart mitral valve repair. In *SPIE Medical Imaging*, pages 90361M–90361M. International Society for Optics and Photonics, 2014.

[26] Stéphane Cotin, Hervé Delingette, and Nicholas Ayache. Real-time elastic deformations of soft tissues for surgery simulation. *Visualization and Computer Graphics, IEEE Transactions on*, 5(1):62–73, 1999.

[27] Leanne M Sutherland, Philippa F Middleton, Adrian Anthony, Jeffrey Hamdorf, Patrick Cregan, David Scott, and Guy J Maddern. Surgical simulation: a systematic review. *Annals of surgery*, 243(3):291, 2006.

[28] Alan Liu, Frank Tendick, Kevin Cleary, and Christoph Kaufmann. A survey of surgical simulation: applications, technology, and education. *Presence: Teleoperators and Virtual Environments*, 12(6):599–614, 2003.

[29] Rolf Adams and Leanne Bischof. Seeded region growing. *Pattern Analysis and Machine Intelligence, IEEE Transactions on*, 16(6):641–647, 1994.

[30] Jie Wu, Skip Poehlman, Michael D Noseworthy, and Markad V Kamath. Texture feature based automated seeded region growing in abdominal MRI segmentation. In *BioMedical Engineering and Informatics, 2008. BMEI 2008. International Conference on*, volume 2, pages 263–267. IEEE, 2008.

[31] Yingyi Qi, Wei Xiong, Wee Kheng Leow, Qi Tian, Jiayin Zhou, Jiang Liu, Thazin Han, Sudhakar K Venkatesh, and Shih-chang Wang. Semi-automatic segmentation of liver tumors from CT scans using bayesian rule-based 3D region growing. In *MiDAS Journal (MICCAI 2008 Workshop: Grand Challenge Liver Tumor Segmentation)*, 2008.

[32] M Mazonakis, J Damilakis, H Varveris, P Prassopoulos, and N Gourtsoyiannis. Image segmentation in treatment planning for prostate cancer using the region growing technique. *British journal of radiology*, 74(879):243–249, 2001.

[33] Ellen Day, James Betler, David Parda, Bodo Reitz, Alexander Kirichenko, Seyed Mohammadi, and Moyed Miften. A region growing method for tumor volume segmentation on PET images for rectal and anal cancer patients. *Medical physics*, 36(10):4349–4358, 2009.

[34] Mustafa A Alattar, Nael F Osman, and Ahmed S Fahmy. Myocardial segmentation using constrained multi-seeded region growing. In *Image Analysis and Recognition*, pages 89–98. Springer, 2010.

[35] Jamshid Dehmeshki, D Amin, Manlio Valdivieso, and Xujiong Ye. Segmentation of

pulmonary nodules in thoracic CT scans: a region growing approach. *Medical Imaging, IEEE Transactions on*, 27(4):467–480, 2008.

[36] Yuusuke Tuduki, Kenya Murase, Masanori Izumida, H Miki, K Kikuchi, K Murakami, and J Ikezoe. Automated seeded region growing algorithm for extraction of cerebral blood vessels from magnetic resonance angiographic data. In *Engineering in Medicine and Biology Society, 2000. Proceedings of the 22nd Annual International Conference of the IEEE*, volume 3, pages 1756–1759. IEEE, 2000.

[37] M Elena Martínez-Pérez, Alun D Hughes, Alice V Stanton, Simon A Thom, Anil A Bharath, and Kim H Parker. Retinal blood vessel segmentation by means of scale-space analysis and region growing. In *Medical Image Computing and Computer-Assisted Intervention–MICCAI99*, pages 90–97. Springer, 1999.

[38] M Elena Martinez-Perez, Alun D Hughes, Alice V Stanton, Simon A Thom, Anil A Bharath, and Kim H Parker. Segmentation of retinal blood vessels based on the second directional derivative and region growing. In *Image Processing, 1999. ICIP 99. Proceedings. 1999 International Conference on*, volume 2, pages 173–176. IEEE, 1999.

[39] R Kyle Justice and Ernest M Stokely. 3-D segmentation of MR brain images using seeded region growing. In *Engineering in Medicine and Biology Society, 1996. Bridging Disciplines for Biomedicine. Proceedings of the 18th Annual International Conference of the IEEE*, volume 3, pages 1083–1084. IEEE, 1996.

[40] Rik Stokking, Koen L Vincken, and Max A Viergever. Automatic morphology-based brain segmentation (MBRASE) from MRI-T1 data. *NeuroImage*, 12(6):726–738, 2000.

[41] David Pasquier, Thomas Lacornerie, Maximilien Vermandel, Jean Rousseau, Eric Lartigau, and Nacim Betrouni. Automatic segmentation of pelvic structures from magnetic resonance images for prostate cancer radiotherapy. *International Journal of Radiation Oncology* Biology* Physics*, 68(2):592–600, 2007.

[42] Jawad Nagi, S Abdul Kareem, Farrukh Nagi, and Syed Khaleel Ahmed. Automated breast profile segmentation for ROI detection using digital mammograms. In *Biomedical Engineering and Sciences (IECBES), 2010 IEEE EMBS Conference on*, pages 87–92. IEEE, 2010.

[43] Predrag R Bakic, Cuiping Zhang, and Andrew DA Maidment. Development and characterization of an anthropomorphic breast software phantom based upon region-growing algorithm. *Medical physics*, 38(6):3165–3176, 2011.

[44] Andrew Mehnert and Paul Jackway. An improved seeded region growing algorithm. *Pattern Recognition Letters*, 18(10):1065–1071, 1997.

[45] R Kyle Justice, Ernest M Stokely, John S Strobel, Raymond E Ideker, and William M Smith. Medical image segmentation using 3D seeded region growing. In *Medical Imaging 1997*, pages 900–910. International Society for Optics and Photonics, 1997.

[46] Geng-Cheng Lin, Wen-June Wang, Chung-Chia Kang, and Chuin-Mu Wang. Multispectral MR images segmentation based on fuzzy knowledge and modified seeded region growing. *Magnetic resonance imaging*, 30(2):230–246, 2012.

[47] Regina Pohle and Klaus D Toennies. Segmentation of medical images using adaptive region growing. In *Medical Imaging 2001*, pages 1337–1346. International Society for Optics and Photonics, 2001.

[48] Michael Kass, Andrew Witkin, and Demetri Terzopoulos. Snakes: Active contour models. *International journal of computer vision*, 1(4):321–331, 1988.

[49] Chenyang Xu and Jerry L Prince. Snakes, shapes, and gradient vector flow. *Image Processing, IEEE Transactions on*, 7(3):359–369, 1998.

[50] Laurent D Cohen. On active contour models and balloons. *CVGIP: Image understanding*, 53(2):211–218, 1991.

[51] Daniel Cremers, Florian Tischhäuser, Joachim Weickert, and Christoph Schnörr. Diffusion snakes: Introducing statistical shape knowledge into the Mumford-Shah functional. *International journal of computer vision*, 50(3):295–313, 2002.

[52] Tim McInerney and Demetri Terzopoulos. T-snakes: Topology adaptive snakes. *Medical image analysis*, 4(2):73–91, 2000.

[53] Tim McInerney and Demetri Terzopoulos. Deformable models in medical image analysis: a survey. *Medical image analysis*, 1(2):91–108, 1996.

[54] Paul A Yushkevich, Joseph Piven, Heather Cody Hazlett, Rachel Gimpel Smith, Sean Ho, James C Gee, and Guido Gerig. User-guided 3D active contour segmentation of anatomical structures: significantly improved efficiency and reliability. *Neuroimage*, 31 (3):1116–1128, 2006.

[55] Timothy F Cootes, Christopher J Taylor, David H Cooper, and Jim Graham. Active shape models-their training and application. *Computer vision and image understanding*, 61(1):38–59, 1995.

[56] Timothy F Cootes, Gareth J Edwards, and Christopher J Taylor. Active appearance models. In *Computer Vision – ECCV98*, pages 484–498. Springer, 1998.

[57] Tobias Heimann and Hans-Peter Meinzer. Statistical shape models for 3D medical image segmentation: A review. *Medical image analysis*, 13(4):543–563, 2009.

[58] Timothy F Cootes, Christopher J Taylor, David H Cooper, and Jim Graham. Training models of shape from sets of examples. In *BMVC92*, pages 9–18. Springer, 1992.

[59] John C Gower. Generalized procrustes analysis. *Psychometrika*, 40(1):33–51, 1975.

[60] Colin Goodall. Procrustes methods in the statistical analysis of shape. *Journal of the Royal Statistical Society. Series B (Methodological)*, pages 285–339, 1991.

[61] Paul J Besl and Neil D McKay. Method for registration of 3-D shapes. In *Robotics-DL tentative*, pages 586–606. International Society for Optics and Photonics, 1992.

[62] Stanley Osher and James A Sethian. Fronts propagating with curvature-dependent speed: algorithms based on Hamilton-Jacobi formulations. *Journal of computational physics*, 79(1):12–49, 1988.

[63] Amar Mitiche and Ismail Ben Ayed. *Variational and level set methods in image segmentation*, volume 5. Springer, 2010.

[64] David Adalsteinsson and James A Sethian. A fast level set method for propagating interfaces. *Journal of computational physics*, 118(2):269–277, 1995.

[65] Ross T Whitaker. A level-set approach to 3D reconstruction from range data. *International Journal of Computer Vision*, 29(3):203–231, 1998.

[66] Cyrus Nambakhsh, Jing Yuan, Kumaradevan Punithakumar, Aashish Goela, Martin Rajchl, Terry M Peters, and Ismail Ben Ayed. Left ventricle segmentation in MRI via convex relaxed distribution matching. *Medical image analysis*, 17(8):1010–1024, 2013.

[67] Eranga Ukwatta, Jing Yuan, Martin Rajchl, Wu Qiu, David Tessier, and Aaron Fenster. 3-D carotid multi-region MRI segmentation by globally optimal evolution of coupled surfaces. *Medical Imaging, IEEE Transactions on*, 32(4):770–785, 2013.

[68] Jasjit S Suri, Kecheng Liu, Sameer Singh, Swamy N Laxminarayan, Xiaolan Zeng, and Laura Reden. Shape recovery algorithms using level sets in 2-D/3-D medical imagery: a state-of-the-art review. *Information Technology in Biomedicine, IEEE Transactions on*, 6(1):8–28, 2002.

[69] Daniel Cremers, Mikael Rousson, and Rachid Deriche. A review of statistical approaches to level set segmentation: integrating color, texture, motion and shape. *International journal of computer vision*, 72(2):195–215, 2007.

[70] Nikos Paragios. A level set approach for shape-driven segmentation and tracking of the left ventricle. *Medical Imaging, IEEE Transactions on*, 22(6):773–776, 2003.

[71] Michael Lynch, Ovidiu Ghita, and Paul F Whelan. Segmentation of the left ventricle of the heart in 3-D+ t MRI data using an optimized nonrigid temporal model. *Medical Imaging, IEEE Transactions on*, 27(2):195–203, 2008.

[72] Cristiana Corsi, Roberto M Lang, Federico Veronesi, Lynn Weinert, Enrico G Caiani, Peter MacEneaney, Claudio Lamberti, and Victor Mor-Avi. Volumetric quantification of global and regional left ventricular function from real-time three-dimensional echocardiographic images. *Circulation*, 112(8):1161–1170, 2005.

[73] Elsa D Angelini, Shunichi Homma, Gregory Pearson, Jeffrey W Holmes, and Andrew F Laine. Segmentation of real-time three-dimensional ultrasound for quantification of ventricular function: a clinical study on right and left ventricles. *Ultrasound in medicine & biology*, 31(9):1143–1158, 2005.

[74] Karl D Fritscher, Roland Pilgram, and Rainer Schubert. Automatic cardiac 4D segmentation using level sets. In *Functional Imaging and Modeling of the Heart*, pages 113–122. Springer, 2005.

[75] Damien Grosgeorge, Caroline Petitjean, Jérôme Caudron, Jeannette Fares, and Jean-Nicolas Dacher. Automatic cardiac ventricle segmentation in mr images: a validation study. *International journal of computer assisted radiology and surgery*, 6(5):573–581, 2011.

[76] Caroline Baillard, Pierre Hellier, and Christian Barillot. Segmentation of brain 3D MR images using level sets and dense registration. *Medical image analysis*, 5(3):185–194, 2001.

[77] Cybèle Ciofolo and Christian Barillot. Brain segmentation with competitive level sets

and fuzzy control. In *Information processing in medical imaging*, pages 333–344. Springer, 2005.

[78] Sean Ho, Elizabeth Bullitt, and Guido Gerig. Level-set evolution with region competition: automatic 3-D segmentation of brain tumors. In *Pattern Recognition, 2002. Proceedings. 16th International Conference on*, volume 1, pages 532–535. IEEE, 2002.

[79] Leonid Zhukov, Ross Whitaker, Ken Museth, David Breen, and Alan H Barr. Level set modeling and segmentation of diffusion tensor magnetic resonance imaging brain data. *Journal of Electronic Imaging*, 12(1):125–133, 2003.

[80] Shiying Hu, Eric A Hoffman, and Joseph M Reinhardt. Automatic lung segmentation for accurate quantitation of volumetric X-ray CT images. *Medical Imaging, IEEE Transactions on*, 20(6):490–498, 2001.

[81] Ruey-Feng Chang, Wen-Jie Wu, Woo Kyung Moon, and Dar-Ren Chen. Automatic ultrasound segmentation and morphology based diagnosis of solid breast tumors. *Breast Cancer Research and Treatment*, 89(2):179–185, 2005.

[82] Andrew S Flett, Jonathan Hasleton, Christopher Cook, Derek Hausenloy, Giovanni Quarta, Cono Ariti, Vivek Muthurangu, and James C Moon. Evaluation of techniques for the quantification of myocardial scar of differing etiology using cardiac magnetic resonance. *JACC: cardiovascular imaging*, 4(2):150–156, 2011.

[83] Prasanna K Sahoo, SAKC Soltani, and Andrew KC Wong. A survey of thresholding techniques. *Computer vision, graphics, and image processing*, 41(2):233–260, 1988.

[84] Heng-Da Cheng, XH Jiang, Ying Sun, and Jingli Wang. Color image segmentation: advances and prospects. *Pattern recognition*, 34(12):2259–2281, 2001.

[85] Nobuyuki Otsu. A threshold selection method from gray-level histograms. *Automatica*, 11(285-296):23–27, 1975.

[86] André Schmidt, Clerio F Azevedo, Alan Cheng, Sandeep N Gupta, David A Bluemke, Thomas K Foo, Gary Gerstenblith, Robert G Weiss, Eduardo Marbán, Gordon F Tomaselli, et al. Infarct tissue heterogeneity by magnetic resonance imaging identifies enhanced cardiac arrhythmia susceptibility in patients with left ventricular dysfunction. *Circulation*, 115(15):2006–2014, 2007.

[87] James MacQueen et al. Some methods for classification and analysis of multivariate observations. In *Proceedings of the fifth Berkeley symposium on mathematical statistics and probability*, volume 1, pages 281–297. California, USA, 1967.

[88] Edward W Forgy. Cluster analysis of multivariate data: efficiency versus interpretability of classifications. *Biometrics*, 21:768–769, 1965.

[89] Paul S Bradley and Usama M Fayyad. Refining initial points for K-Means clustering. In *ICML*, volume 98, pages 91–99, 1998.

[90] James C Bezdek. *Pattern recognition with fuzzy objective function algorithms*. Kluwer Academic Publishers, 1981.

[91] James C Bezdek, Robert Ehrlich, and William Full. FCM: The fuzzy c-means clustering algorithm. *Computers & Geosciences*, 10(2):191–203, 1984.

[92] Richard Nock and Frank Nielsen. On weighting clustering. *Pattern Analysis and Machine Intelligence, IEEE Transactions on*, 28(8):1223–1235, 2006.

[93] Robert L Cannon, Jitendra V Dave, and James C Bezdek. Efficient implementation of the fuzzy c-means clustering algorithms. *Pattern Analysis and Machine Intelligence, IEEE Transactions on*, (2):248–255, 1986.

[94] Mohamed N Ahmed, Sameh M Yamany, Nevin Mohamed, Aly A Farag, and Thomas Moriarty. A modified fuzzy c-means algorithm for bias field estimation and segmentation of MRI data. *Medical Imaging, IEEE Transactions on*, 21(3):193–199, 2002.

[95] Keh-Shih Chuang, Hong-Long Tzeng, Sharon Chen, Jay Wu, and Tzong-Jer Chen. Fuzzy c-means clustering with spatial information for image segmentation. *computerized medical imaging and graphics*, 30(1):9–15, 2006.

[96] Dao-Qiang Zhang and Song-Can Chen. A novel kernelized fuzzy c-means algorithm with application in medical image segmentation. *Artificial intelligence in medicine*, 32 (1):37–50, 2004.

[97] Arthur P Dempster, Nan M Laird, Donald B Rubin, et al. Maximum likelihood from incomplete data via the EM algorithm. *Journal of the Royal statistical Society*, 39(1): 1–38, 1977.

[98] Sean Borman. The expectation maximization algorithm-a short tutorial, 2009.

[99] Geoffrey McLachlan and Thriyambakam Krishnan. *The EM algorithm and extensions*, volume 382. John Wiley & Sons, 2007.

[100] Richard A Redner and Homer F Walker. Mixture densities, maximum likelihood and the EM algorithm. *SIAM review*, 26(2):195–239, 1984.

[101] Alvaro R De Pierro. A modified expectation maximization algorithm for penalized likelihood estimation in emission tomography. *IEEE Transactions on Medical Imaging*, 14 (1):132, 1995.

[102] Yongyue Zhang, Michael Brady, and Stephen Smith. Segmentation of brain MR images through a hidden Markov random field model and the expectation-maximization algorithm. *Medical Imaging, IEEE Transactions on*, 20(1):45–57, 2001.

[103] Emanuel Levitan and Gabor T Herman. A maximum a posteriori probability expectation maximization algorithm for image reconstruction in emission tomography. *Medical Imaging, IEEE Transactions on*, 6(3):185–192, 1987.

[104] Maria Lorenzo-Valdés, Gerardo I Sanchez-Ortiz, Andrew G Elkington, Raad H Mohiaddin, and Daniel Rueckert. Segmentation of 4D cardiac MR images using a probabilistic atlas and the EM algorithm. *Medical Image Analysis*, 8(3):255–265, 2004.

[105] Tobias Heimann, Bram Van Ginneken, Martin A Styner, Yulia Arzhaeva, Volker Aurich, Christian Bauer, Andreas Beck, Christoph Becker, Reinhard Beichel, György Bekes, et al. Comparison and evaluation of methods for liver segmentation from CT datasets. *Medical Imaging, IEEE Transactions on*, 28(8):1251–1265, 2009.

[106] Koen Van Leemput, Frederik Maes, Dirk Vandermeulen, and Paul Suetens. Automated model-based tissue classification of MR images of the brain. *Medical Imaging, IEEE Transactions on*, 18(10):897–908, 1999.

[107] Simon K Warfield, Kelly H Zou, and William M Wells. Validation of image segmentation and expert quality with an expectation-maximization algorithm. In *Medical Image Computing and Computer-Assisted Intervention – MICCAI 2002*, pages 298–306. Springer, 2002.

[108] Torsten Rohlfing, Daniel B Russakoff, and Calvin R Maurer Jr. Performance-based classifier combination in atlas-based image segmentation using expectation-maximization parameter estimation. *Medical Imaging, IEEE Transactions on*, 23(8):983–994, 2004.

[109] James C Bezdek, LO Hall, LP Clarke, et al. Review of MR image segmentation techniques using pattern recognition. *Medical Physics*, 20:1033–1033, 1993.

[110] Naomi S Altman. An introduction to kernel and nearest-neighbor nonparametric regression. *The American Statistician*, 46(3):175–185, 1992.

[111] Kevin Beyer, Jonathan Goldstein, Raghu Ramakrishnan, and Uri Shaft. When is nearest neighbor meaningful? In *Database Theory – ICDT99*, pages 217–235. Springer, 1999.

[112] Corinna Cortes and Vladimir Vapnik. Support-vector networks. *Machine learning*, 20 (3):273–297, 1995.

[113] Bernhard E Boser, Isabelle M Guyon, and Vladimir N Vapnik. A training algorithm for optimal margin classifiers. In *Proceedings of the fifth annual workshop on Computational learning theory*, pages 144–152. ACM, 1992.

[114] Kai-Bo Duan and S Sathiya Keerthi. Which is the best multiclass SVM method? an empirical study. In *Multiple Classifier Systems*, pages 278–285. Springer, 2005.

[115] Chih-Wei Hsu and Chih-Jen Lin. A comparison of methods for multiclass support vector machines. *Neural Networks, IEEE Transactions on*, 13(2):415–425, 2002.

[116] AG van Opbroek, F van der Lijn, and Marleen de Bruijne. Automated brain-tissue segmentation by multi-feature SVM classification. 2013.

[117] Min Hyeok Bae, Teresa Wu, and Rong Pan. Mix-ratio sampling: Classifying multiclass imbalanced mouse brain images using support vector machine. *Expert Systems with Applications*, 37(7):4955–4965, 2010.

[118] Keyvan Kasiri, Kamran Kazemi, Mohammad Javad Dehghani, and Mohammad Sadegh Helfroush. Atlas-based segmentation of brain MR images using least square support vector machines. In *Image Processing Theory Tools and Applications (IPTA), 2010 2nd International Conference on*, pages 306–310. IEEE, 2010.

[119] JW Clark. Neural network modelling. *Physics in Medicine and Biology*, 36(10):1259, 1991.

[120] Lawrence O Hall, Amine M Bensaid, Laurence P Clarke, Robert P Velthuizen, Martin S Silbiger, and James C Bezdek. A comparison of neural network and fuzzy clustering techniques in segmenting magnetic resonance images of the brain. *Neural Networks, IEEE Transactions on*, 3(5):672–682, 1992.

[121] Wilburn E Reddick, John O Glass, Edwin N Cook, T David Elkin, and Russell J Deaton. Automated segmentation and classification of multispectral magnetic resonance images of brain using artificial neural networks. *Medical Imaging, IEEE Transactions on*, 16 (6):911–918, 1997.

[122] James C Bezdek, LO Hall, and L_P Clarke. Review of MR image segmentation techniques using pattern recognition. *Medical physics*, 20(4):1033–1048, 1992.

[123] Leo Breiman. Random forests. *Machine learning*, 45(1):5–32, 2001.

[124] Yali Amit and Donald Geman. Shape quantization and recognition with randomized trees. *Neural computation*, 9(7):1545–1588, 1997.

[125] Antonio Criminisi, Jamie Shotton, and Ender Konukoglu. Decision forests: A unified framework for classification, regression, density estimation, manifold learning and semi-supervised learning. *Foundations and Trends in Computer Graphics and Vision*, 7(2–3): 81–227, 2012.

[126] Victor Lempitsky, Michael Verhoek, J Alison Noble, and Andrew Blake. Random forest classification for automatic delineation of myocardium in real-time 3D echocardiography. In *Functional Imaging and Modeling of the Heart*, pages 447–456. Springer, 2009.

[127] Ezequiel Geremia, Bjoern H Menze, Olivier Clatz, Ender Konukoglu, Antonio Criminisi, and Nicholas Ayache. Spatial decision forests for MS lesion segmentation in multi-channel MR images. In *Medical Image Computing and Computer-Assisted Intervention–MICCAI 2010*, pages 111–118. Springer, 2010.

[128] Juergen Gall and Victor Lempitsky. Class-specific hough forests for object detection. In *Decision Forests for Computer Vision and Medical Image Analysis*, pages 143–157. Springer, 2013.

[129] Sérgio Pereira, José H Correia, and Carlos A Silva. Automatic segmentation of brain tissues using Random Forests. *MRBrainS 2013 - MICCAI Grand Challenge on MR Brain Segmentation 2013*, 2014.

[130] Jagath C Rajapakse, Jay N Giedd, and Judith L Rapoport. Statistical approach to segmentation of single-channel cerebral MR images. *Medical Imaging, IEEE Transactions on*, 16(2):176–186, 1997.

[131] Thrasyvoulos N Pappas. An adaptive clustering algorithm for image segmentation. *Signal Processing, IEEE Transactions on*, 40(4):901–914, 1992.

[132] Karsten Held, E Rota Kops, Bernd J Krause, WMIII Wells, Ron Kikinis, and H-W Muller-Gartner. Markov random field segmentation of brain MR images. *Medical Imaging, IEEE Transactions on*, 16(6):878–886, 1997.

[133] Fedde van der Lijn, Tom den Heijer, Monique Breteler, and Wiro J Niessen. Hippocampus segmentation in MR images using atlas registration, voxel classification, and graph cuts. *Neuroimage*, 43(4):708–720, 2008.

[134] Jyrki MP Lötjönen, Robin Wolz, Juha R Koikkalainen, Lennart Thurfjell, Gunhild Waldemar, Hilkka Soininen, and Daniel Rueckert. Fast and robust multi-atlas segmentation of brain magnetic resonance images. *Neuroimage*, 49(3):2352–2365, 2010.

[135] Yuri Boykov and Vladimir Kolmogorov. An experimental comparison of min-cut/max-flow algorithms for energy minimization in vision. *Pattern Analysis and Machine Intelligence, IEEE Transactions on*, 26(9):1124–1137, 2004.

[136] Yuri Boykov, Olga Veksler, and Ramin Zabih. Fast approximate energy minimization via graph cuts. *Pattern Analysis and Machine Intelligence, IEEE Transactions on*, 23 (11):1222–1239, 2001.

[137] Peter Elias, Amiel Feinstein, and Claude E Shannon. A note on the maximum flow through a network. *Information Theory, IRE Transactions on*, 2(4):117–119, 1956.

[138] Lester R Ford and Delbert R Fulkerson. Maximal flow through a network. *Canadian journal of Mathematics*, 8(3):399–404, 1956.

[139] Andrew V Goldberg and Robert E Tarjan. A new approach to the maximum-flow problem. *Journal of the ACM (JACM)*, 35(4):921–940, 1988.

[140] Yuri Boykov and Vladimir Kolmogorov. Computing geodesics and minimal surfaces via graph cuts. In *Computer Vision, 2003. Proceedings. Ninth IEEE International Conference on*, pages 26–33. IEEE, 2003.

[141] Yuri Boykov and Marie-Pierre Jolly. Interactive organ segmentation using graph cuts. In *Medical Image Computing and Computer-Assisted Intervention–MICCAI 2000*, pages 276–286. Springer, 2000.

[142] Yuri Boykov and Gareth Funka-Lea. Graph cuts and efficient ND image segmentation. *International journal of computer vision*, 70(2):109–131, 2006.

[143] Yuri Y Boykov and M-P Jolly. Interactive graph cuts for optimal boundary & region segmentation of objects in ND images. In *Computer Vision, 2001. ICCV 2001. Proceedings. Eighth IEEE International Conference on*, volume 1, pages 105–112. IEEE, 2001.

[144] Robin Wolz, Paul Aljabar, Daniel Rueckert, Rolf A Heckemann, and Alexander Hammers. Segmentation of subcortical structures and the hippocampus in brain MRI using graph-cuts and subject-specific a-priori information. In *Biomedical Imaging: From Nano to Macro, 2009. ISBI'09. IEEE International Symposium on*, pages 470–473. IEEE, 2009.

[145] Akinobu Shimizu, Keita Nakagomi, Takuya Narihira, Hidefumi Kobatake, Shigeru Nawano, Kenji Shinozaki, Koich Ishizu, and Kaori Togashi. Automated segmentation of 3D CT images based on statistical atlas and graph cuts. In *Medical Computer Vision. Recognition Techniques and Applications in Medical Imaging*, pages 214–223. Springer, 2011.

[146] Gilbert Strang. Maximal flow through a domain. *Mathematical Programming*, 26(2): 123–143, 1983.

[147] Gilbert Strang. Maximum flows and minimum cuts in the plane. *Journal of Global Optimization*, 47(3):527–535, 2010.

[148] Jing Yuan, Egil Bae, and Xue-Cheng Tai. A study on continuous max-flow and min-cut approaches. In *Computer Vision and Pattern Recognition (CVPR), 2010 IEEE Conference on*, pages 2217–2224. IEEE, 2010.

[149] M Rajchl, J Yuan, and TM Peters. Real-time segmentation in 4d ultrasound with continuous max-flow. In *SPIE Medical Imaging*, pages 83141F–83141F. International Society for Optics and Photonics, 2012.

[150] Renfrey Burnard Potts. Some generalized order-disorder transformations. In *Mathematical Proceedings of the Cambridge Philosophical Society*, volume 48, pages 106–109. Cambridge Univ Press, 1952.

[151] Tony F Chan, Selim Esedoglu, and Mila Nikolova. Algorithms for finding global minimizers of image segmentation and denoising models. *SIAM Journal on Applied Mathematics*, 66(5):1632–1648, 2006.

[152] Jing Yuan, Egil Bae, Xue-Cheng Tai, and Yuri Boykov. A continuous max-flow approach to potts model. In *Computer Vision–ECCV 2010*, pages 379–392. Springer, 2010.

[153] Claudia Nieuwenhuis, Eno Töppe, and Daniel Cremers. A survey and comparison of discrete and continuous multi-label optimization approaches for the Potts model. *International journal of computer vision*, 104(3):223–240, 2013.

[154] Hiroshi Ishikawa. Exact optimization for Markov random fields with convex priors. *Pattern Analysis and Machine Intelligence, IEEE Transactions on*, 25(10):1333–1336, 2003.

[155] M Rajchl, J Yuan, E Ukwatta, and TM Peters. Fast interactive multi-region cardiac segmentation with linearly ordered labels. In *Biomedical Imaging (ISBI), 2012 9th IEEE International Symposium on*, pages 1409–1412. IEEE Conference Publications, 2012.

[156] E Versi. "Gold standard" is an appropriate term. *BMJ: British Medical Journal*, 305 (6846):187, 1992.

[157] Arno Klein, Jesper Andersson, Babak A Ardekani, John Ashburner, Brian Avants, Ming-Chang Chiang, Gary E Christensen, D Louis Collins, James Gee, Pierre Hellier, et al. Evaluation of 14 nonlinear deformation algorithms applied to human brain MRI registration. *Neuroimage*, 46(3):786–802, 2009.

[158] Kelly H Zou, Simon K Warfield, Aditya Bharatha, Clare Tempany, Michael R Kaus, Steven J Haker, William M Wells III, Ferenc A Jolesz, and Ron Kikinis. Statistical validation of image segmentation quality based on a spatial overlap index: scientific reports. *Academic radiology*, 11(2):178–189, 2004.

[159] William R Crum, Oscar Camara, and Derek LG Hill. Generalized overlap measures for evaluation and validation in medical image analysis. *Medical Imaging, IEEE Transactions on*, 25(11):1451–1461, 2006.

[160] Paul Jaccard. The distribution of the flora in the alpine zone. 1. *New phytologist*, 11(2): 37–50, 1912.

[161] John J Bartko. The intraclass correlation coefficient as a measure of reliability. *Psychological reports*, 19(1):3–11, 1966.

[162] J Martin Bland and DouglasG Altman. Statistical methods for assessing agreement between two methods of clinical measurement. *The lancet*, 327(8476):307–310, 1986.

[163] John SH Baxter, Martin Rajchl, A Jonathan McLeod, Ali R Khan, Jing Yuan, and Terry M Peters. Smoothness parameter tuning for generalized hierarchical continuous max-flow segmentation. In *SPIE Medical Imaging*, pages 903410–903410. International Society for Optics and Photonics, 2014.

[164] Chris McIntosh and Ghassan Hamarneh. Optimal weights for convex functionals in medical image segmentation. *Advances in Visual Computing*, pages 1079–1088, 2009.

Chapter 2

Interactive Hierarchical Max-Flow Segmentation of Scar Tissue from Late-Enhancement Cardiac MR Images

2.1 Introduction

Late gadolinium enhancement (LE) cardiac MRI is a well-established clinical tool for visualizing and quantifying myocardial fibrosis, or 'scar' in both ischemic and non-ischemic cardiomyopathy. As shown in [1], all patients with ischemic cardiomyopathy (ICM) and approximately one-third of patients with dilated cardiomyopathy (DCM) have myocardial scar by LE-MRI. Both of these conditions are associated with significant morbidity and mortality including hospitalization for severe congestive heart failure (CHF), arrhythmia, and sudden cardiac death. The clinical interest in myocardial scar imaging using LE-MRI has dramatically increased over

This Chapter is adapted from a published article. ©[2014] IEEE. Reprinted, with permission, from M. Rajchl, J. Yuan, J.A.White, E. Ukwatta, J. Stirrat, C. Nambakhsh, F. Li, and T.M.Peters (2014). *Interactive Hierarchical Max-Flow Segmentation of Scar Tissue from Late-Enhancement Cardiac MR Images.* IEEE Transactions on Medical Imaging, 33(1), 159–172.

Paper	Dim	Constraint Seg. & Extr. Method	data *N*	Time
Breeuwer[4]	2D	Manual contours & man. adj. thresh.	10 humans	-
O'Donnell[5]	2D	Siemens Argus & SVM	14 humans	-
Dikici[6]	2D	[7] w/ man. corr. & SVM	45 humans	-
Kolipaka[8]	2D	Manual contours & thresholding	23 humans	-
Positano [9]	2D	GVF snakes & fuzzy c-mean clustering	15 humans	-
Hsu[10]	2D	Manual contours & FACT	11 canine	-
Säring[11]	2D	Manual contours on cine MRI & STRM	6 humans	-
Hennemuth[12]	2D	Live wire w/ Watershed Segmentation	21 humans	-
Bogun[13]	2D	-	14 humans	-
Lehmann[14]	2D	Model-based segmentation	20 humans	-
Neizel[15]	2D	Manual contours & thresholding	62 humans	1.6±0.2min
Elagouni[16]	2D	[17] & thresholding with morph. cleaning	11 humans	0.2s/slc
Tao[18]	2D	Manual contours & conn. filtering, RG	20 humans	-
Elnakib[19]	2D	- & Joint MGRF	168 slices	8 min/pat.
Flett[20]	2D	Manual contours & thresholding	60 humans	-
Neizel[21]	3D	Model-based segmentation	20 humans	-
Barbarito[22]	3D	Atlas-based semi-automated segmentation using [23]	10 humans	- -

Table 2.1: Previous studies on extraction of non-viable myocardial tissue.

the past decade, while recent evidence has demonstrated the ability of myocardial scar imaging to predict patient response to medical, surgical, and device therapies.

Moreover, extensive studies of using LE-MRI to predict response to cardiac resynchronization therapy (CRT) and implantable cardioverter defibrillator (ICD) therapy, e.g. [2, 3], showed that the presence of LE predicted worse prognosis for ICD/CRT patients and for CRT therapy and confirmed the critical factor of quantifying the location and extent of the scar. On the other hand, LE-MRI can also be applied to guide the delivery of cardiac electrophysiology procedures, such as ablative therapies for elimination of atrial or ventricular arrhythmias. However, the translation of such information into the clinical practice is challenging.

2.1.1 Previous Studies

In this section, we summarize previous studies on segmentation of myocardial scar tissue from LE-MRI. We can categorize them into two groups based on image acquisition: *2D LE-MRI*

slice stacks and *3D whole-heart (WH) LE-MRI acquisitions* (as shown in Table 2.1.1).

2D LE-MRI slice stacks

The application of highly anisotropic LE-MRI images in clinical practice has been established since the introduction of ventricular viability assessment in the early 2000s [24]. While the in-plane resolution of these short-axis (SAX) images is 1-2mm, the acquired slice thickness is around 8-10mm along the long-axis (LAX). This property suggests the use of algorithms that operate slice-by-slice on SAX views and interpolate resulting scar regions in LAX direction.

A common strategy for scar segmentation of 2D slices include myocardial segmentation to limit the search of scar tissue (see Table 2.1.1) to valid regions. This approach can be found in all 2D methods, except for [19] (see Table 2.1.1). The myocardial boundaries were either segmented manually [4, 10, 21, 20] or semi-automatically [5, 9, 8, 12, 16] directly on the 2D LE-MRI or obtained from other spatially registered images, such as cine MRI [6, 11, 18].

Within the given myocardial region, the differentiation between viable and non-viable (scar) tissue can then be performed with the use of intensity thresholds, such as full-width-at-half-maximum (FWHM) [8, 15, 20], signal-threshold-to-reference-mean (STRM) [8, 11, 20] or manually adjusted thresholds [4, 8, 15, 20]. Other proposed scar extraction approaches include decision making via SVM [5, 6], clustering [9], watershed segmentation [12] or morphological operations with region growing [18] or region competition [16].

3D whole-heart LE-MRI acquisitions

In the past five years, several studies [25, 26, 27] proposed techniques to acquire LE-MRI with WH coverage with potential to image scar tissue with high isotropic resolution. Such 3D WH techniques have been extensively compared to their 2D predecessor in terms of their image characteristics and have been attested the ability to better delineate lesions [28, 29], to image

with higher scar signal intensity (SI) [29], better contrast [28, 29], improved image quality [30], superior diagnostic quality scores [31, 28] and reduced acquisition times [32, 33**?**] than clinically standard 2D acquisitions.

In particular the ability to better resolve small lesions [26, 34, 35] is preferable in patients with surgically corrected Tetralogy of Fallot (TOF) (N_{RV}), where the scar is mostly found in the thin myocardial wall of the right-ventricular outflow tract (RVOT). Recently, there have been interventional studies making use of 3D WH LE-MRI in ventricular interventions, such as ventricular tachycardia (VT) ablation [36, 37] and planning and image-guidance for CRT [38, 39] at different field strengths. In particular the high resolution of cardiovascular magnetic resonance (CMR) imaging deems it preferable for visualization of fibrosis in image-guided interventional procedures [36, 37, 40].

However, these image-guided interventional therapies rely on accurate quantification of scar from 3D LE-MRI. Recently, several approaches, e.g. [21, 22], were proposed to segment the left ventricular (LV) scar tissue from such high-resolution 3D WH LE-MRI. Similar to most 2D approaches, these methods require prior identification of the myocardium to constrain subsequent intensity thresholding operations for scar segmentation. These myocardial segmentations can be performed on early contrast enhancement (CE) MRI, which are intrinsically spatially registered with the later acquired WH LE-MR images. However, errors appearing in the additional myocardium segmentation do affect the accuracy of the subsequent scar tissue segmentations. Errors due to early contrast enhanced endocardial boundaries and patient movement between the acquisition time point of the CE MRI and the LE-MRI can potentially affect the accuracy of the subsequently extracted scar.

Distinct from the above approaches, in this work we demonstrate a novel method to extract the 3D cardiac scar tissue region efficiently and accurately from a single input LE-MRI, *without* any additional prior segmentation of myocardial boundaries.

2.1.2 Contributions

In this chapter, we propose a novel multi-region segmentation method to extract myocardial scar tissue directly from a single 3D WH LE-MR image, by enforcing a customized ordering of the regions specific to the anatomy. The segmentation algorithm is initialized via user-specified seeds over a graphical user interface (GUI) and allows quick recomputations to progressively obtain high accuracy scar segmentation results in a semi-automated manner. For this purpose, we introduce a new partially-ordered Potts (POP) model to multi-region segmentation, that is customized to the anatomical configuration and distinct intensity appearances in 3D LE-MRI.

We solve the proposed combinatorial optimization problem of the POP model by means of convex relaxation. In this regard, we propose a new continuous max-flow formulation along with a novel two-level flow configuration, namely the *hierarchical continuous max-flow (HMF) model*, and demonstrate its duality or equivalence to the studied convex relaxed POP model. The proposed HMF model implicitly encodes the specified cardiac region order/layout by additional dual flows, which avoids tackling the challenging cardiac region order constraint explicitly. The HMF model also directly derives an efficient HMF (duality)-based algorithm by modern convex optimization theories, which can be implemented on GPUs and achieve a high numerical efficiency on the commercially available graphics hardware.

Experiments were performed over 3D WH LE-MRI datasets (N_{LV}=35) obtained on a Siemens Trio 3T MRI scanner in subjects with prior myocardial infarction and additionally on subjects presenting with the right-ventricular (RV) scar in post-operative Tetralogy of Fallot (TOF) repair images (N_{RV}=15). Accuracy and preliminary operator variability experiments were conducted and results compared to conventional region-constrained methods, e.g. the FWHM (full-width at half-maximum) or the STRM (signal-threshold-to-reference-mean) method for which prior myocardial segmentation is required. Both FWHM and STRM are methods where the differentiation of scar and healthy tissue is determined via intensity thresholds. The FWHM method determines this threshold by the maximum intensity in a sampled region within the myocardium, while the STRM's threshold is defined from a mean healthy myocardial intensity

+2-6 standard deviations.

This chapter is an extension of a preliminary study that appeared in [41]. Here we extend our prior work with a more extensive discussion of the optimization theory and numerical implementation, and have added material related to the formulations and propositions. Evaluation of the procedure was performed on an additional 40 datasets to comprehensively validate the approach and compare its performance with others reported in the literature.

2.2 Methods

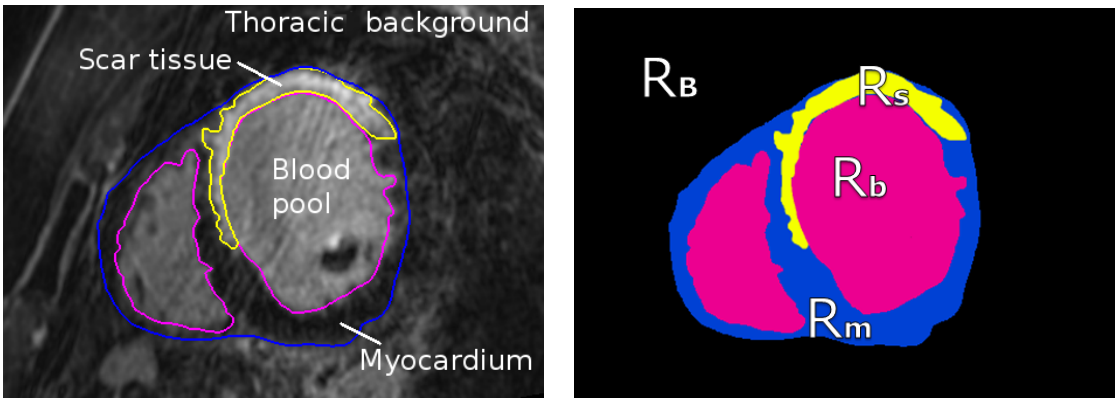

(a) (b)

Figure 2.1: Proposed label ordering based on anatomic spatial consistency **??** and contours overlaid on a LE-MRI slice (b). The region constraining the heart is divided into three sub-regions: myocardium (R_m), blood (R_b) and scar tissue (R_s). R_B represents the thoracic background.

Given a 3D LE-MRI, two disjoint anatomical regions can be identified (see Fig. **??** and 2.1(b)): the cardiac region R_C and the thoracic background R_B:

$$\Omega = \mathcal{R}_C \cup \mathcal{R}_B, \quad \mathcal{R}_C \cap \mathcal{R}_B = \emptyset, \tag{2.1}$$

where the cardiac region R_C further contains three spatially coherent sub-regions: the my-

ocardium R_m, the blood pool R_b and the scar-tissue R_s, i.e.

$$\mathcal{R}_C = \mathcal{R}_s \cup \mathcal{R}_m \cup \mathcal{R}_b \,; \tag{2.2}$$

and the three cardiac sub-regions R_m, R_b and R_s are mutually disjoint

$$\mathcal{R}_m \cap \mathcal{R}_b = \emptyset \,, \quad \mathcal{R}_m \cap \mathcal{R}_s = \emptyset \,, \quad \mathcal{R}_b \cap \mathcal{R}_s = \emptyset \,. \tag{2.3}$$

Typically, each of the sub-regions R_m, R_b and R_s has its distinct appearance, constituting the complex appearance model of the whole cardiac region $\mathcal{R}_C$. This fact makes it challenging to directly extract the boundaries of $\mathcal{R}_C$ from the given LE-MRI image without any further appearance knowledge and, in turn, identify its inherent sub-region of scar tissue $\mathcal{R}_s$ correctly. In this chapter, we propose to encode the appearance of the cardiac region $\mathcal{R}_C$ by three distinct *independent and identically distributed (i.i.d.) models* of intensities w.r.t. $R_{m,b,s}$, and integrate it into the new *POP model* which properly enforces the anatomical region layout prior (2.1) - (2.3) (we refer to the Appendix A for a short review of the general Potts model without such region order constraint).

Many studies [42, 43, 44, 45, 46, 47, 48, 49] have shown that incorporating such prior knowledge of inter-region relationships greatly helps to improve the accuracy of the multi-region segmentation problem.

In this section, we introduce the novel approach to accurately and efficiently extract the scar tissue region $\mathcal{R}_s$ from the input 3D LE-MRI volume, which jointly locates the five anatomically relevant regions $\mathcal{R}_{C,B}$ and $\mathcal{R}_{m,b,s}$ by employing the a priori anatomical region layout (2.1) and (2.2).

We solve the challenging combinatorial optimization problem associated to the proposed *POP model* by means of convex relaxation, for which we propose the new and efficient continuous max-flow approach along with a novel hierarchical flow maximization structure, also called the *continuous HMF model*.

To simplify the notation, we define the label sets: $L_1 := \{ C , B \}$ and $L_2 := \{ s , m , b \}$, i.e. L_2 represents the label set of the three cardiac sub-regions enclosed by the cardiac region $\mathcal{R}_C$;

2.2.1 Partially-Ordered Potts Model and Convex Relaxation

In this chapter, we study the segmentation of the input LE-MRI $I(x)$ through the intensity appearance models of the regions $\mathcal{R}_i$, $i \in L_1 \cup L_2$, i.e. the respective probability density functions (PDFs) of intensities. Such intensity appearance models provide a global descriptor of the objects of interest in statistics, which can be learned from either sampled pixels or specified training datasets.

In particular, the intensity appearance of each cardiac sub-region $\mathcal{R}_i$, $i \in L_2$, is distinct from each other and visually more homogeneous within each corresponding local sub-region.

Let $\omega_i(I(x))$, $i \in L_2$, be the PDF of the cardiac sub-region $\mathcal{R}_i$, which gives the possibility that each pixel $x \in \Omega$ belongs to $\mathcal{R}_i$ and depends upon the local intensity information $I(x)$. The PDF can be computed from regions of interest, for example user-specified seeds. Accordingly, all the functions $\omega_i(I(x))$, $i \in L_2$, in combination present a complex intensity description of the whole cardiac region $\mathcal{R}_C$. Such a complex intensity model is shown to be more appropriate than the often-used Gaussian mixture model (GMM) of intensities or appearances in practice [50]. In addition, let the function $\omega_B(I(x))$ encode the intensity appearance model for the background region $\mathcal{R}_B$.

We therefore define the cost functions ρ_i, $i \in B \cup L_2$, of labelling each pixel x to be in the cardiac sub-regions $\mathcal{R}_i$, $i \in L_2$, or the background region $\mathcal{R}_B$, by the log-likelihoods of the respective PDFs [51], i.e.

$$\rho_i(x) \; = \; - \log \left(\omega_i(I(x)) \right) , \quad i \in B \cup L_2 \, . \tag{2.4}$$

Given the inclusion of three disjoint sub-regions (2.2) and (2.3) of the cardiac region $\mathcal{R}_C$, labelling the pixel $x \in \Omega$ to be in any cardiac sub-region $\mathcal{R}_{s,m,b}$ directly enforces it to belong

to the cardiac region $\mathcal{R}_C$, and its labelling cost is readily given by the cost to the respective labelled sub-region $\mathcal{R}_{s,m,b}$. Hence, the total labelling cost, for segmenting the input LE-MRI $I(x)$ into the regions

$$\mathcal{R}_C \cup \mathcal{R}_B := \{\mathcal{R}_s \cup \mathcal{R}_m \cup \mathcal{R}_b\} \cup \mathcal{R}_B\,, \tag{2.5}$$

can be consequently formulated by

$$\sum_{i\in B\cup L_2} \int_{\mathcal{R}_i} \rho_i(x)\, dx\,. \tag{2.6}$$

To this end, we propose to segment the given 3D LE-MRI $I(x)$ by achieving the minimum total labelling costs along with minimal partitioning length between the regions such that

$$\min_{\mathcal{R}_{C,B},\mathcal{R}_{s,m,b}} \quad \sum_{i\in B\cup L_2} \int_{\mathcal{R}_i} \rho_i(x)\, dx \;+\; \sum_{i\in L_1\cup L_2} \int_{\partial\mathcal{R}_i} ds\,, \tag{2.7}$$

subject to the constraints of the region order layout (2.1) - (2.3).

We call (2.7) the *POP model*, which is in contrast to the commonly-used Potts model as discussed in the Appendix A.

Let $u_i(x) \in \{0,1\}$, $i \in L_1 \cup L_2$, be the indicator or labelling function of the corresponding region $\mathcal{R}_i$, such that

$$u_i(x) := \begin{cases} 1\,, & \text{where } x \text{ is inside } \mathcal{R}_i \\ 0\,, & \text{otherwise} \end{cases}\,, \quad i \in L_1 \cup L_2\,.$$

Then we can equally formulate the region constraint (2.1) by

$$u_C(x) + u_B(x) = 1\,, \quad \forall x \in \Omega \tag{2.8}$$

and the constraints (2.2)-(2.3) of the cardiac sub-regions by

$$u_s(x) + u_m(x) + u_b(x) = u_C(x)\,, \quad \forall x \in \Omega\,. \tag{2.9}$$

Therefore, the *POP model* (2.7) can be equivalently represented by the labelling functions $u_i(x) \in \{0, 1\}$, $i \in L_1 \cup L_2$, as follows

$$\min_{u(x)\in\{0,1\}} \sum_{i\in B\cup L_2} \langle u_i, \rho_i \rangle + \sum_{i\in L_1\cup L_2} \int_\Omega g(x)\, |\nabla u_i(x)|\, dx \tag{2.10}$$

subject to the labelling constraints (2.8) and (2.9), where $g(x) \geq 0$ represents the weight function of the total-variation term that measures the weighted area of each surface $\partial\mathcal{R}_i$, $i \in L_1 \cup L_2$. We denote the inner product in a Hilbert function space by $\langle \cdot, \cdot \rangle$, i.e. for two functions $f(x)$ and $g(x)$, $\langle f, g \rangle := \int f(x)g(x)\, dx$.

In this work, we solve the *POP model*-associated combinatorial optimization problem (2.10) by its convex relaxation:

$$\min_{u(x)\in[0,1]} \sum_{i\in B\cup L_2} \langle u_i, \rho_i \rangle + \sum_{i\in L_1\cup L_2} \int_\Omega g(x)\, |\nabla u_i(x)|\, dx \tag{2.11}$$

subject to the linear equality constraints (2.8) and (2.9). Note, the indicator function u in (2.11) is now in continuous space, i.e. $u(x) \in [0, 1]$.

The binary-valued labelling functions $u_i(x) \in \{0, 1\}$, $i \in L_1 \cup L_2$, in the *POP model* (2.7) are relaxed into the convex constraint $u_i(x) \in [0, 1]$ in (2.11).

Given the convex energy function of (2.11) and the linear equality constraints (2.8) and (2.9), the challenging combinatorial optimization problem (2.10) is then reduced to the convex optimization problem (2.11).

We call (2.11) the *convex relaxed POP model*.

2.2.2 Hierarchical Continuous Max-Flow Model

In this section, we introduce a novel continuous max-flow approach to solving the proposed *convex relaxed POP model* (2.11) efficiently, where a new spatially continuous flow-maximization model is introduced as a dual/equivalent to the *convex relaxed partially-ordered Potts model* (2.11).

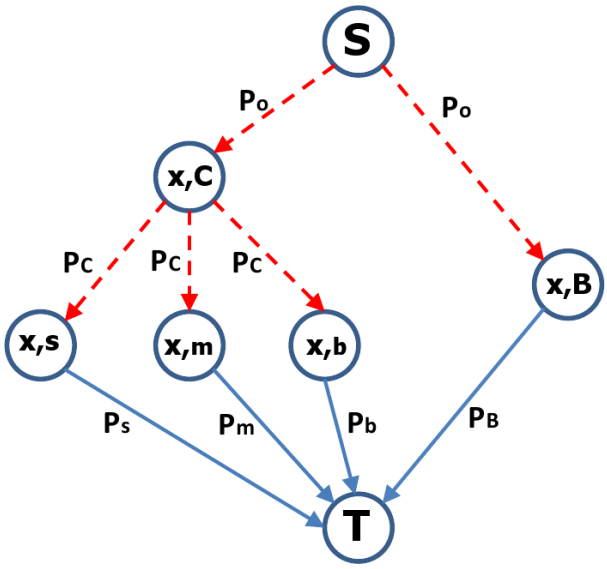

Figure 2.2: The flow configuration of the proposed *hierarchical continuous max-flow model*: links between terminals and the image domains, the source flow $p_o(x)$, the cardiac flow $p_C(x)$ and the sink flows $p_i(x)$, $i \in B \cup L_2$. Note that, unconstrained flows are red connections and data costs for each label are blue.

We first specify the new two-level hierarchical flow configuration in the spatially continuous setting (see Fig. 2.2), which is inspired by the proposed continuous max-flow approach [52, 53] to the classical Potts model and min-cut problem:

– We add two terminals s and t as the source and sink of the flows, the two image copies Ω_C and Ω_B w.r.t. $\mathcal{R}_C$ and $\mathcal{R}_B$ in parallel at the upper level, and the three image copies $\Omega_{s,m,b}$ w.r.t. $\mathcal{R}_{s,m,b}$ in parallel at the bottom level.

– We link the source s to the same position x of Ω_C and Ω_B, along which an unconstrained source flow $p_o(x)$ is defined. We link any $x \in \Omega_C$ to the same pixel x at each of $\Omega_{s,m,b}$, along which an unconstrained cardiac flow $p_C(x)$ is defined. In addition, we link each pixel x of Ω_B and $\Omega_{s,m,b}$ to the sink t, along which the sink flow $p_i(x)$, $i \in B \cup L_2$, is given.

– Additionally, the spatial flow $q_i(x)$, $i \in L_1 \cup L_2$, is specified at x within each image domain Ω_i.

Based upon the above settings of flows, we propose the *HMF model* which maximizes the total flow streaming from the source s to the sink t, i.e.

$$\max_{p,q} \quad \int_{\Omega} p_o(x)\, dx \tag{2.12}$$

subject to

– *Flow capacity constraints*: the sink flows $p_i(x)$, $i \in B \cup L_2$ suffice:

$$p_i(x) \;\leq\; \rho_i(x)\,, \quad i \in B \cup L_2\,, \tag{2.13}$$

and the spatial flows $q_i(x)$, $i \in L_1 \cup L_2$ suffice:

$$|q_i(x)| \;\leq\; g(x)\,, \quad i \in L_1 \cup L_2\,. \tag{2.14}$$

– *Flow conservation constraints*: the total flow residue vanishes at each x within any upper-level image domain Ω_i, $i \in L_1 = \{C, B\}$, i.e.

$$G_i(x) \;:=\; (\operatorname{div} q_i - p_o + p_i)(x) \;=\; 0\,, \quad i \in \{C, B\}\,; \tag{2.15}$$

and the total flow residue also vanishes at each x within any bottom-level image domain Ω_i, $i \in L_2 (= \{s, m, b\})$, i.e.

$$G_i(x) \;:=\; (\operatorname{div} q_i - p_C + p_i)(x) \;=\; 0\,, \quad i \in \{s, m, b\}\,. \tag{2.16}$$

As defined above, the source flow function $p_o(x)$ and the cardiac flow function $p_C(x)$ are both free of constraints.

Through analysis, we can prove the duality between the *continuous HMF model* (2.12) and the *convex relaxed POP model* (2.11):

Proposition 2.2.1 *The* hierarchical continuous max-flow (HMF) model (2.12) *and the* convex

relaxed partially-ordered Potts (POP) model (2.11) *are dual (equivalent) to each other, i.e.*

$$(2.12) \iff (2.11)\,.$$

Proof Introduce the multiplier functions $u_i(x)$, $i \in L_1 \cup L_2$, to each respective flow residue functions $G_i(x)$ in the flow conservation constraints (2.15) and (2.16). We can then express the *continuous HMF formulation* (2.12) equivalently as follows:

$$\min_{u} \max_{p.q} \; L(u; p, q) := \int_{\Omega} p_o(x)\, dx + \sum_{i \in L_1 \cup L_2} \langle u_i, G_i \rangle \;, \tag{2.17}$$

subject to the flow capacity constraints (2.13) and (2.14), where the flow functions $p_o(x)$, $p_i(x)$ and $q_i(x)$, $i \in L_1 \cup L_2$, are abbreviated by p, q for short.

Clearly, the energy function $L(u; p, q)$ of (2.17) just gives the Lagrangian function of (2.12). In the following steps, we take similar analysis as in [52, 53].

To compute the saddle point of (2.17), we first maximize (2.17) over the sink flows $p_i(x)$, $i \in B \cup L_2$, subject to (2.13), which gives rise to

$$u_i(x) \;\geq\; 0\,, \quad i \in B \cup L_2\,;$$

then maximize (2.17) over the free source flows $p_o(x)$ and $p_C(x)$, which results in

$$u_C(x) + u_B(x) = 1\,, \quad u_C(x) - (u_s + u_m + u_b)(x) = 0\,;$$

and maximize (2.17) over the spatial flows $q_i(x)$, $i \in L_1 \cup L_2$, subject to (2.14), which directly amounts to the sum of the weighted total variation functions of $u_i(x)$, $i \in L_1 \cup L_2$. Through simple computation and reorganization, then the *convex relaxed POP model* (2.11) follows.

Therefore, we have

$$(2.12) \iff (2.17) \iff (2.11)\,.$$

The proposition is proved.

2.2.3 Hierarchical Continuous Max-Flow Algorithm

By Prop. 2.2.1, it is easy to see that the *convex relaxed POP model* (2.11) can be solved equally by computing the *continuous HMF model* (2.12). Moreover, as shown in the proof of Prop. 2.2.1, the labelling functions $u_i(x)$, $i \in L_1 \cup L_2$, act as the optimum multipliers to the respective flow conservation constraints of (2.15) and (2.16), which derives the new *hierarchical continuous max-flow algorithm* proposed in this section through the modern convex optimization technique [54].

The *hierarchical continuous max-flow algorithm* enjoys numerical advantages in that it successfully avoids directly tackling non-smooth total-variation functions in the energy of the *convex relaxed POP model* (2.11) by the projections to some simple convex sets; in addition, it also implicitly adapts the labelling constraints (2.8) and (2.9) into the introduced flow configurations (as illustrated in Fig. 2.2).

Clearly, the primal-dual optimization problem (2.17) is equivalent to the *HMF model* (2.12), where the labelling functions $u_i(x)$, $i \in L_1 \cup L_2$, work as the multipliers to the linear equality constraints (2.15) and (2.16) of flow conservation, and the energy function of (2.17) is just the associated Lagrangian function of the flow-maximization problem (2.12) constrained by flow conservations (2.15) and (2.16).

Hence, by the theory of augmented multiplier algorithms [54], an efficient *continuous HMF algorithm* can be derived, which iteratively optimizes the following augmented Lagrangian function:

$$\max_{p,q} \min_{u} L_c(u; p, q) := L(u; p, q) - \frac{c}{2} \sum_{i \in L_1 \cup L_2} \|G_i\|^2 ,$$

subject to the flow capacity constraints (2.13) and (2.14), where $L(u; p, q)$ is the Lagrangian function (2.17) associated with the *continuous HMF model* (2.12).

The *HMF algorithm* explores the following steps at each k-th iteration:

- Maximize $L_c(u; p, q)$ over the spatial flows $|q_i(x)| \leq g(x)$, $i \in L_1 \cup L_2$, while fixing the other variables $(u; p)^k$, which amounts to

$$q_i^{k+1} := \arg\max_{|q_i(x)| \leq g(x)} -\frac{c}{2} \left\| \operatorname{div} q_i - F_i^k \right\|^2 ,$$

where $F_i^k(x)$, $i \in L_1 \cup L_2$, is directly computed from the fixed variables.

This can be computed by the gradient-projection iteration:

$$q_i^{k+1} = \operatorname{Proj}_{|q_i(x)| \leq g(x)}(q_i^k + \tau \nabla(\operatorname{div} q_i^k - (F_i^k)) ; \tag{2.18}$$

where $\tau > 0$ is the step-size for convergence [55].

- Maximize $L_c(u; p, q)$ over the source flow $p_o(x)$, while fixing the other variables $(u; p_i, q)^k$, which amounts to

$$(p_o)^{k+1} := \arg\max_{p_o} \int_\Omega p_o \, dx - \frac{c}{2} \sum_{i \in \{B,C\}} \left\| p_o - J_i^k \right\|^2 ,$$

where $J_i^k(x)$, $i \in \{B, C\}$, is directly computed from the fixed variables. This can be solved exactly by:

$$(p_o)^{k+1}(x) = (J_B^k(x) + J_C^k(x) + 1/c)/2 . \tag{2.19}$$

- Maximize $L_c(u; p, q)$ over the cardiac flow $p_C(x)$, while fixing the other variables $(u; p_o, p_{B,s,m,b}, q)^k$, which amounts to

$$(p_C)^{k+1} := \arg\max_{p_C} -\frac{c}{2} \sum_{i \in C \cup L_2} \left\| p_C - T_i^k \right\|^2 ,$$

where $T_i^k(x)$, $i \in C \cup L_2$, is directly computed by the fixed variables. This can be solved exactly by:

$$(p_C)^{k+1}(x) = \frac{1}{4} \sum_{i \in C \cup L_2} T_i^k(x) . \tag{2.20}$$

- Maximize $L_c(u; p, q)$ over $p_i(x) \leq \rho_i(x)$, $i \in B \cup L_2$, while fixing the other variables $(u; p_o, p_C, q)^k$, which amounts to

$$(p_i)^{k+1} := \underset{p_i(x) \leq \rho_i(x)}{\arg\max} -\frac{c}{2} \left\| p_i - H_i^k \right\|^2 ,$$

where $H_i^k(x)$, $i \in B \cup L_2$, is directly computed from the fixed variables. This can be solved exactly by:

$$(p_i)^{k+1}(x) = \min(H_i^k(x), \rho_i(x)) . \tag{2.21}$$

- Update the labelling functions $u_i(x)$, where $i \in L_1 \cup L_2$, by

$$u_i^{k+1} = u_i^k - c\, G_i^k(x) , \quad i \in L_1 \cup L_2$$

where $G_i^k(x)$, $i \in L_1 \cup L_2$, stands for the respective flow residue function.

Experiments have shown, that a single gradient-projection step (2.18) is needed to achieve convergence, greatly improving numerical efficiency. After convergence, $u_i(x)$ can be discretized by determining a maximum of $u_i(x)$ across $i = 1 \ldots n$.

2.3 Experiments

2.3.1 Study Subjects and Image Acquisition

Study subjects were recruited for the CMCR program at Robarts Research Institute of Western University (London, ON) during which they received coronary CE-MRI examination using a whole-heart, respiratory navigated, 3D inversion-recovery gradient echo pulse sequence (Siemens 3T Trio, Erlangen, GER) during and 30 minutes following infusion of 0.2 mmol/kg Gadovist (Bayer, Toronto, ON) (see details in Section 3.2.1). 35 subjects presenting with myocardial infarction and 15 subjects with surgically corrected TOF were imaged according to

this protocol which was approved by the Research Ethics Board of Western University, after receiving written consent.

Table 2.3.1 shows the parameters of the imaging protocol. One patient exhibiting LV scar and one patient with TOF were visually uninterpretable due to severe imaging artifacts and had to be excluded for quantitative analysis.

Acquisition Parameter	Field
Manufacturer	Siemens Medical
Model	MAGNETOM Trio w/ Tim
Field strength	3 Tesla
Echo Time	1.3 ms
Flip angle	20°
Pixel Spacing	1.3 x 1.3 mm
Slice Thickness	1.3 mm
Pulse Sequence	Inversion-recovery gradient echo

Table 2.2: Imaging Parameters for 3D WH LE-MRI

2.3.2 Interactive Segmentation Pipeline

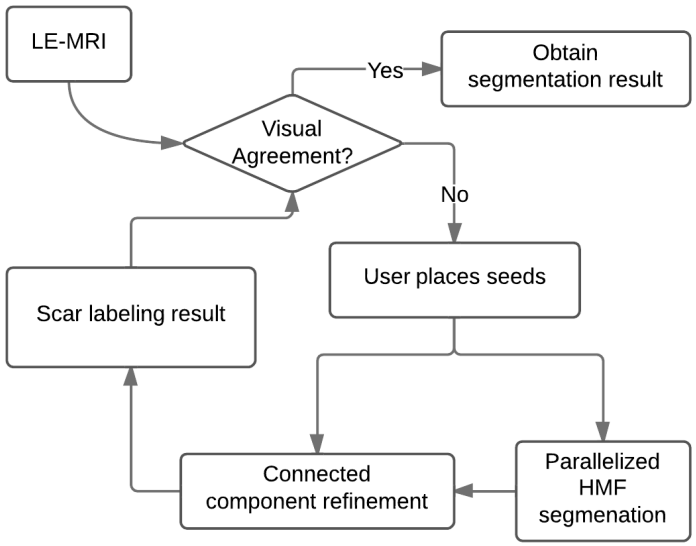

Figure 2.3: Proposed interactive segmentation pipeline. A user interactively seeds and computes segmentation results until the there the result is satisfactory (visual agreement).

We developed a graphical user interface in C++ (see Fig. 2.4) with open source libraries

Qt (Qt Development Frameworks, Oslo, NOR), VTK and ITK (Kitware Inc, Clifton Park, NY) for interactions with the image data, and implemented the proposed optimization algorithm on a parallel computing architecture (CUDA, NVIDIA Corp., Santa Clara, CA) for a significant computing speed-up and best possible interactivity. The user has access to standard image visualization features such as window-level, opacity sliders for label and a 2D brush tool. Additionally, a multi-planar reconstruction view is available for the user to display a surface-rendered resulting scar volume and quickly spot misclassifications. With the help of the brush tool, the user can sample intensities within each region of $\mathcal{R}_i$, $i \in B \cup L_2$ on three orthogonal slice views, and calculate the respective 64-bin normalized histogram $\omega_i(I(x))$.

We obtain the cost function from the computed histograms with a log-likelihood calculation [51], i.e. $\rho_i(x) = -\log \omega_i(I(x))$. Additionally, we use the user input seeds as hard constraints, providing the ability to interactively correct for intensity inconsistencies, such as artifacts or uncertain regions and give the user end-control over the results.

The label l_s, representing the non-viable scar tissue, is subsequently refined to all connected components containing seeds (see Fig. 2.3 'Connected component refinement'). This step is different from the post-processing morphological operations described in [18] and merely ensures that only regions annotated with seeds are classified as scar tissue while other high intensity regions (for example from the valvular apparatus or epicardial fatty tissue) are excluded.

It reduces user interactions required to account for false positives and is intended to reduce the overall time spent with user interactions.

In the experiments, the total variation penalties $g(x)$ in (2.11) were given depending the local image edge information, such that $g(x) = \lambda_1 + \lambda_2 \exp(-\lambda_3 |\nabla I(x)|^2)$, where $\lambda_{1,2,3} \geq 0$ can be adjusted by the user to improve segmentation results. Values are limited from 0.05 - 1. and defaulted to $\lambda_1^{C,B} = 0.35$, $\lambda_2^{C,B} = 0.5$, $\lambda_1^{s,m,b} = 0.15$ and $\lambda_2^{s,m,b} = 0.5$. λ_3 was fixed to the value of 10, heuristically determined to be appropriate for the applied images.

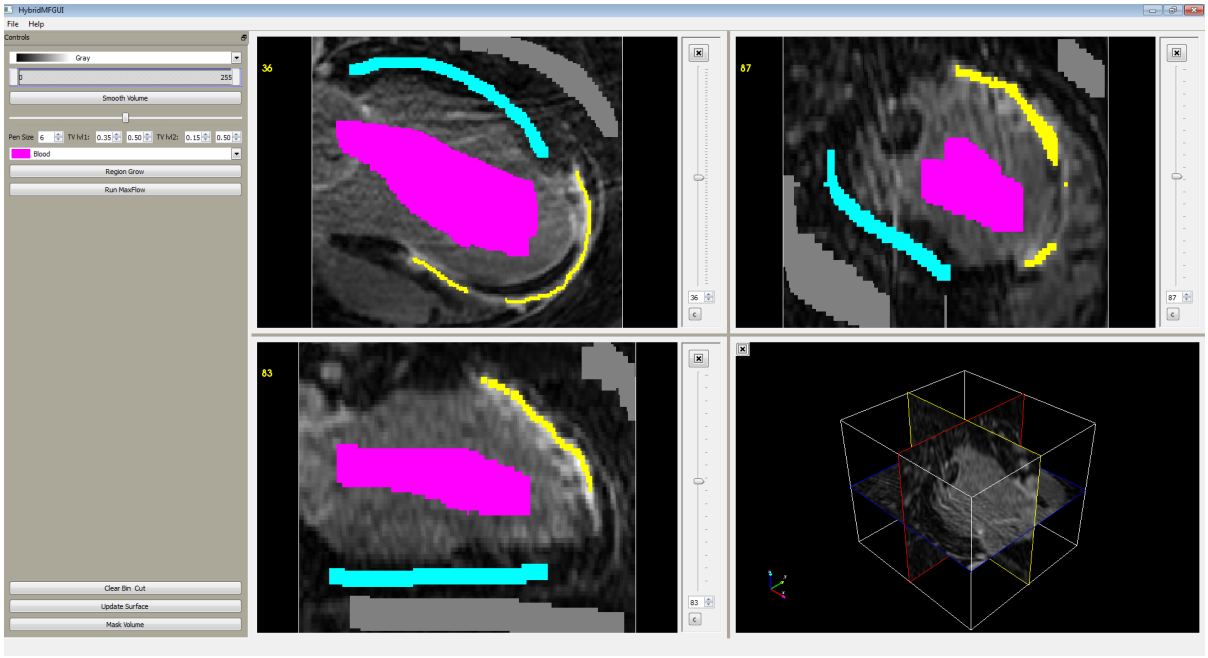

Figure 2.4: Graphical user interface with 2D seeds in orthogonal slice views for segmentation: R_B (grey), R_b (magenta), R_m (cyan) and R_s (yellow).

2.3.3 Comparative Experiments

Studies found in the current literature (see Table 2.1.1) utilize model- or atlas-based segmentations to limit the search for scar tissue to the myocardium. To minimize the methodological bias we employed 3D *manual* expert constraint segmentations to simulate such model- or atlas-based approach without bias of the respective method. Given myocardial segmentations, the scar can be extracted by threshold-based methods such as a FWHM or an STRM approach. To obtain a stable maximum the user marks a hyper-enhanced region of interest and scar tissue is subsequently determined by $\geq 50\%$ of the obtained maximum [56]. In the case of STRM, the user selects a region of remote viable myocardium and the scar is thresholded by an obtained mean +X standard deviations (SD). For our comparative accuracy experiments, we calculate results for FWHM, STRM +3SD and STRM +6SD.

2.3.4 Validation metrics

To assess the performance of the proposed algorithm, we compared our results against single-user expert manual segmentations. We chose region-, volume- and surface-based measures to determine the accuracy and reproducibility of the method and compared its performance on datasets presenting with LV scar tissue with the FWHM and STRM methods, respectively.

Regional metric

We used the Dice similarity coefficient as a measure of overlap of compared regions, representing the percentage of true-positives identified by the tested method.

$$DSC = \frac{2(R_M \cap R_A)}{R_M + R_A}, \tag{2.22}$$

R_M defines the manually segmented region and R_A is the region obtained from the algorithm output.

Surface-based metrics

As surface-based metric we used root-mean-squared-error (RMSE) from vertex points of iso-surfaces generated from the label maps of the algorithm output and the manual segmentations:

$$RMSE = \sqrt{\frac{1}{N_m}\sum_{i=1}^{N_m} d(m_i, A)^2}, \tag{2.23}$$

where m_i is the set of manual vertex points $\{m_i : i = 1, ..., N_m\}$, $A = \{a_i : i = 1, ..., N_A\}$ the set of the algorithm output and d the Euclidean distance in *mm*. Additionally, the Hausdorff distance (HD) is calculated to measure the maximum distance in a dataset:

$$HD = \max_{i \in [1, N_m]} \{d(m_i, A)\}, \tag{2.24}$$

Volume-based metric

A total volume error $\delta V_E = V_A - V_M$ and percentage volume error (δV_P) serves as volume-based measure.

$$\delta V_P = \frac{(V_A - V_M)}{V_M} \times 100\% \tag{2.25}$$

Additionally we compute absolute values of these two metrics to better reflect the deviation from the manually segmented gold standard.

2.3.5 Operator variability

A randomly sampled subset of the database was used to estimate inter- and intra-operator variabilities. This subset includes five datasets from N_{LV} and five from N_{RV} which was repeatedly segmented three times by two users. To minimize the systematic bias, we let one user $U1$ segment the entire database manually to establish a gold standard segmentation, while two other users $U2$ and $U3$ were testing all compared methods blindly. The resulting segmentations are subject to accuracy and operator variability assessment. We calculate an Intraclass correlation coefficient (ICC) and a coefficient of variation (CV) from the operator variability results to estimate variability within and between users.

2.3.6 Effect of user interaction

Additionally, we conducted experiments to demonstrate the effects of repeated user interaction and visual inspection of the proposed method to characterize its bias. For this purpose, a user ($U1$) was asked to segment a subset of 10 datasets of N_{LV} and record the segmentation result for each interaction (the placement of seeds and subsequent HMF computation is considered an interaction) with the interface. We calculate a DSC and RMSE for each of the first five interactions to determine the intermediate accuracy and compare it to FWHM and STRM methods.

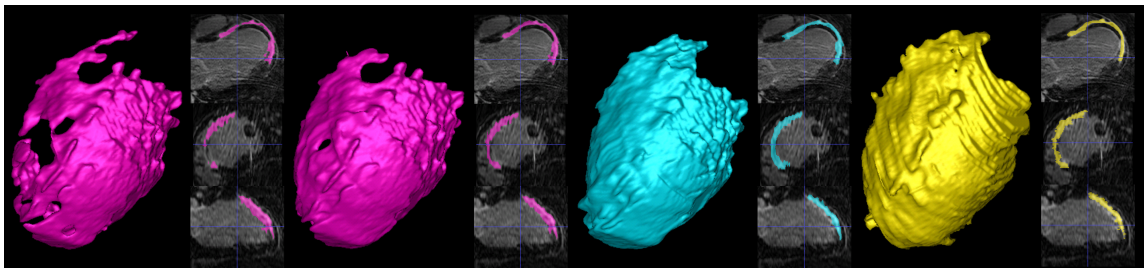

Figure 2.5: Intermediate results after one (magenta, left) and three recomputations (magenta, right), final algorithm result after 5 recomputations (cyan) with the proposed method and manual expert segmentation (yellow). Accompanying slice views show the respective label on transverse (top), sagital (middle) and coronal (bottom) cut planes.

2.4 Results

3D LE-MR imaging protocols were completed for all 50 patients. Image quality was scored acceptable in 34 of 35 patients presenting with LV scar and 14 of 15 patients with TOF. Two cases were excluded due to severe image artifacts related to respiratory gating and diaphragmal ghosting, respectively. Fig. 2.5 depicts intermediate results with progressive user interaction on an example dataset. Fig. 2.6 shows results of all compared methods and demonstrates drawbacks of each techniques in this example dataset. The proposed HMF method overestimates the scar volume endocardially (Fig. 2.6, row 3, column 1), while FWHM and STRM +6SD fail to identify scar (Fig. 2.6, row 4&6, column 2&3) and STRM +3SD, generally overestimates the scar volume and additionally being prone to respiratory artifacts (Fig. 2.6, row 5).

2.4.1 Segmentation Time

Segmentation	time[min]
HMF_{LV}	6.5 ± 2.3
HMF_{RV}	9.4 ± 3.2
Myocardial constraint segmentations	54.7 ± 17.6
Manual scar segmentations	42.0 ± 16.4

Table 2.3: Segmentation time [min]

Table 2.3 shows the average time in minutes to complete the respective tasks. HMF_{LV} segmentation times decreased in average from those reported in [41]. All segmentations were

performed on a Windows workstation with 3.33 GHz Xeon processors (Intel, Santa Clara, CA) with 48 GB RAM and a NVIDIA Tesla C2070 GPU. For each max-flow recomputation, the time required for calculation of the data term was less than 1.4s, less than 1.1s for the calculation of the regularization weights and less than 12s in average for the CUDA-based continuous max-flow optimization.

2.4.2 Accuracy

		DSC (%)	**RMSE** (mm)	**HD** (mm)
LV	HMF	76.0 ± 3.6	1.02 ± 0.29	10.62 ± 6.37
	FWHM	58.9 ± 13.7	5.35 ± 8.00	54.20 ± 27.21
	STRM +3SD	53.5 ± 17.0	16.41 ± 11.32	74.13 ± 15.42
	STRM +6SD	68.0 ± 12.7	7.74 ± 9.31	67.95 ± 18.26
RV	HMF	71.3 ± 4.5	0.70 ± 0.15	8.12 ± 3.74

Table 2.4: Accuracy results for N_{LV} and N_{RV}. Dice Similarity coefficient (DSC), root-mean-squared error (RMSE), Haussdorff distance (HD)

		$\lvert\delta\mathbf{V_E}\rvert$ (ml)	$\lvert\delta\mathbf{V_P}\rvert$ (%)	$\delta\mathbf{V_E}$ (ml)	$\delta\mathbf{V_P}$ (%)
LV	HMF	4.05 ± 3.58	16.97 ± 13.46	3.36 ± 4.25	12.91 ± 17.49
	FWHM	12.77 ± 14.81	39.81 ± 25.83	−11.99 ± 15.47	−32.48 ± 34.82
	STRM +3SD	34.57 ± 14.68	229.57 ± 259.32	34.57 ± 14.68	229.57 ± 259.32
	STRM +6SD	8.13 ± 6.46	45.14 ± 48.89	2.20 ± 10.23	27.69 ± 60.81
RV	HMF	1.02 ± 1.20	11.43 ± 12.64	0.90 ± 1.30	8.86 ± 14.69

Table 2.5: Accuracy results for N_{LV} and N_{RV}. Total volume errors (δV_E) and volume percentage errors (δV_P)

The mean and standard deviations of the metrics described in Section 2.3.4 for all methods can be found in Tables 2.4 & 2.5. The proposed algorithm outperformed the comparative methods in all metrics for all N_{LV}. The mean RMSE plus one standard deviation for both N_{LV} and N_{RV} was within the voxel resolution of $1.3mm$. The DSC reflecting the true-positives of identified scar tissue was $76.0 \pm 3.6\%$ and $71.3 \pm 4.5\%$ respectively. The DSC metric however is biased towards volume size, i.e. larger regions of interest generally yield higher DSC overlaps.

		Pearson r	95%-CI	p-value
LV	HMF	.987	0.974 – 0.993	< 0.001
	FWHM	.602	0.336 – 0.779	< 0.001
	STRM +3SD	.856	0.731 – 0.925	< 0.001
	STRM +6SD	.851	0.723 – 0.923	< 0.001
RV	HMF	.989	0.978 – 0.995	< 0.001

Table 2.6: Pearson's correlation coefficients and confidence intervals for scar volumes

This is reflected in the lower DSC for N_{RV}, where there are typically smaller scar regions, with simultaneously lower mean RMSE surface error.

Pearson correlations were calculated with SPSS 20 (IBM Corp., Armonk, NY). Table 2.6 shows the correlation coefficient and 95% confidence intervals of volumes of the proposed algorithm and comparative methods with the manually segmented volumes. All results were considered significant when the probability of making a type I error was less than 5% ($p < 0.05$).

2.4.3 Operator variability

To assess the inter- and intra-operator variabilities, we calculated the CV to estimate the variability relative to the mean of the repeated segmentation with the proposed method. Table 2.7 also shows the calculated ICC, a single measure of absolute agreement using a two-way mixed study.

	LV			RV		
UID	CV[%]	ICC[0,1]	DSC[%]	CV[%]	ICC[0,1]	DSC[%]
U2	6.52	0.923	77.5 ± 1.7	8.59	0.984	71.2 ± 3.8
U3	5.76	0.938	72.8 ± 3.6	9.86	0.978	66.0 ± 3.9
Inter	8.70	0.941	76.2 ± 2.6	13.0	0.983	69.4 ± 4.6

Table 2.7: Inter- and intra-observer variability results for the HMF algorithm. Coefficient of variation (CV), Intra-class correlation coefficient (ICC) and Dice Similarity Coefficient (DSC)

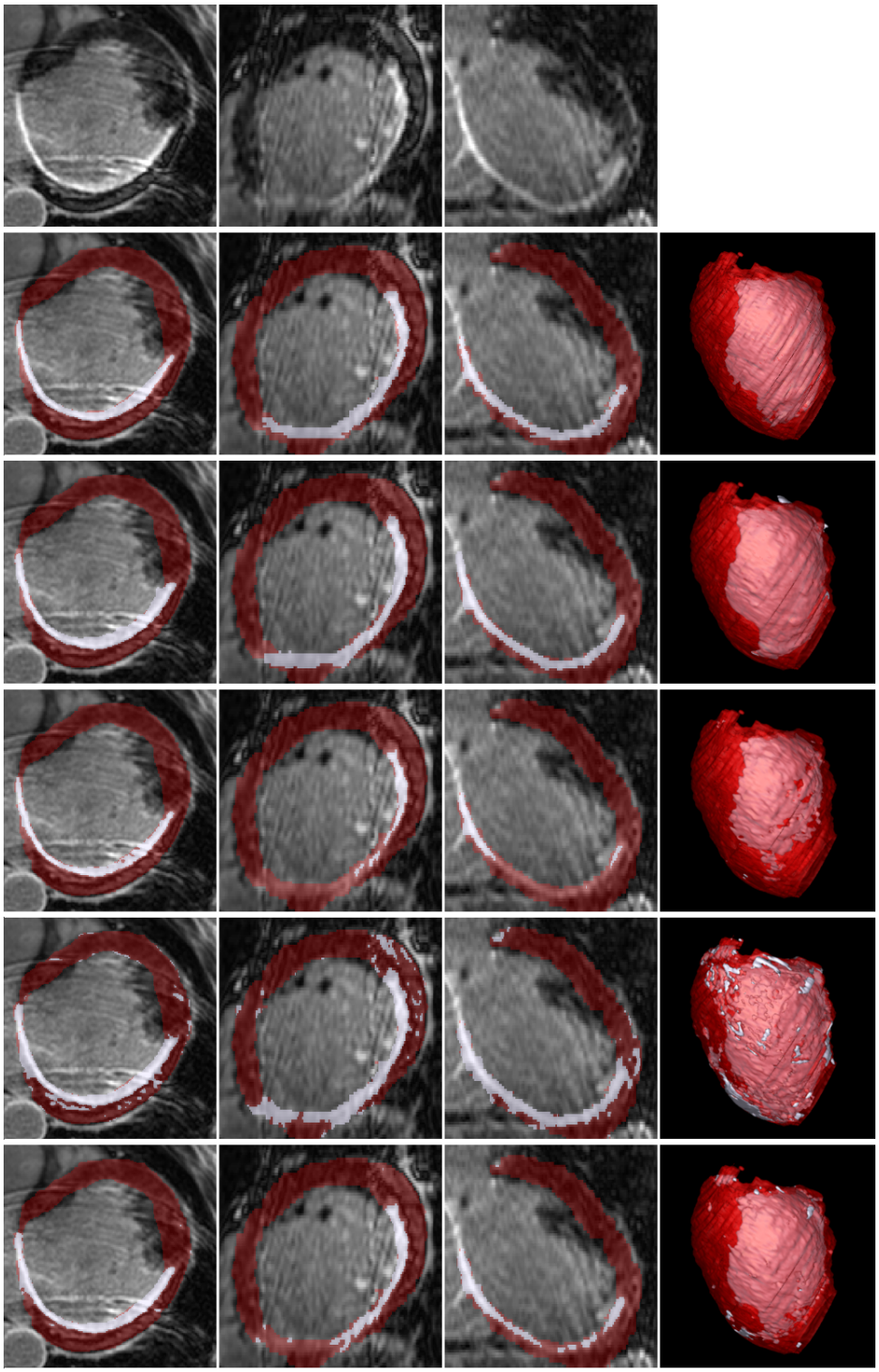

Figure 2.6: Segmentation results on orthogonal slice views (column 1-3) and surface rendered results (column 4). From top to bottom, scar segmentation results (white) and myocardium (red) : a) original image, b) expert manual segmentation, c) HMF, d) FWHM, e) STRM+3SD, f) STRM+6SD.

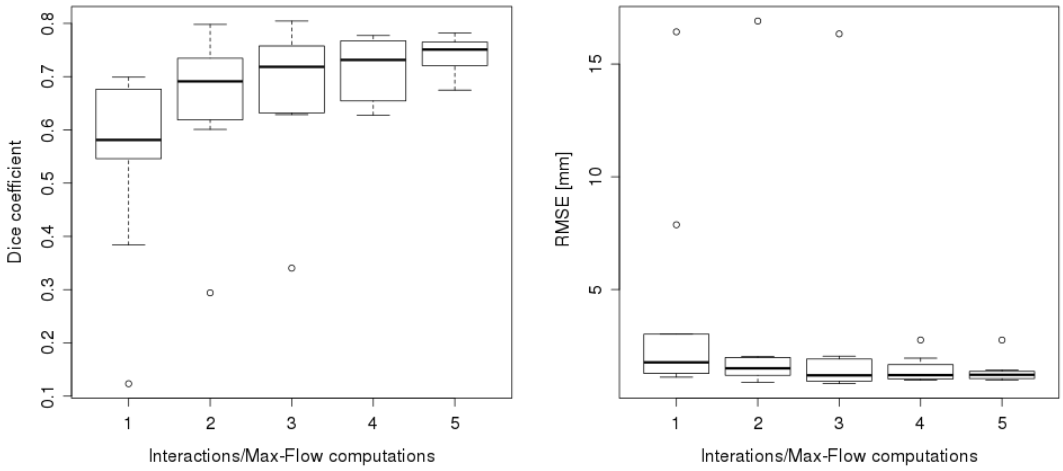

Figure 2.7: HMF segmentation accuracy results on 10 datasets in terms of Dice Coefficient (DSC) and root mean squared error (RMSE) in mm with increasing user interaction.

2.4.4 Effect of user interaction

Table 2.8 states the resulting DSC and RMSE with progressive user interactions and the corresponding comparative FWHM and STRM methods on the 10 dataset of N_{LV}. Figure 2.7 depicts the box plots demonstrating that two datasets presented as outliers, which the user was able to correct for after 4 interactions.

		Interactions	**DSC** (%)	**RMSE** (mm)
LV	HMF	1	54.9 ± 17.3	3.91 ± 5.24
		2	65.7 ± 14.3	3.02 ± 4.90
		3	68.7 ± 14.0	2.76 ± 4.79
		4	71.4 ± 6.7	1.44 ± 0.62
		5	73.4 ± 4.3	1.39 ± 0.62
		done	77.6 ± 3.3	1.07 ± 0.18
	FWHM		52.4 ± 10.2	4.53 ± 9.24
	STRM +3SD		63.0 ± 16.1	13.34 ± 10.95
	STRM +6SD		72.1 ± 8.9	8.08 ± 11.60

Table 2.8: Accuracy results with increasing user interactions on 10 datasets of N_{LV} for HMF and comparative accuracy results on these data for FWHM, STRM +3SD and STRM +6SD stated as Dice Similarity coefficient (DSC), root-mean-squared error (RMSE).

2.5 Discussion

We developed and validated a new semi-automated approach to segmenting myocardial scar tissue from 3D WH LE-MRI, based on a novel *POP model*, which essentially enforces the anatomically consistent layout of cardiac regions to constrain searching the scar tissue boundaries and properly utilizes the distinct intensity appearance models of cardiac regions. This method can be directly applied to LE-MRI without relying on additional imaging modalities or prior segmentations, thus reducing secondary influences and additional potential sources of errors. This challenging combinatorial optimization problem is solved efficiently by convex relaxation, for which a novel *continuous HMF model* is proposed.

In addition, the *continuous HMF algorithm* is implemented on commercially available graphics hardware, which allows a rapid 3D multi-region segmentation and fast refinements of the three cardiac regions. The user can easily retain the overall control of the entire segmentation process. We compare the proposed algorithm with the FWHM and STRM approaches, which are widely employed in the literature, in terms of efficiency and accuracy.

2.5.1 Segmentation Time

The average segmentation time by the proposed method was 6.5 minutes for N_{LV} and 9.4 minutes for N_{RV} respectively. We initially reported a greater mean segmentation time for a subset of N_{LV} in [41], which might have been due to a learning effect with using the interface or the sample not being representative in terms of scar extent and image quality. The higher segmentation times for N_{RV} is due to the fact that the scar after surgically corrected TOF is generally smaller in volume and the fibrotic tissue layer thinner, thus requiring more accurate seed placement with the required lower regularization.

2.5.2 Accuracy

The proposed approach outperformed the comparative methods in all accuracy metrics. The mean RMSE for N_{LV} was $1.02 \pm 0.29mm$ and for N_{RV} $0.70 \pm 0.15mm$, both of which were lower than the LE-MRI voxel dimensions of 1.3x1.3x1.3mm and demonstrated excellent agreement between the results with the gold standard in subvoxel range. The increased RMSE for N_{LV} can be due to intensity inconsistencies from diaphragmatic ghosting artifacts, small inclusions of fibrotic papillary muscles, chordae tendineae or the valve apparatus, which are not all present in the right ventricular outflow tract (RVOT) scars found in TOF patients. This is also reflected in the HD distance results of N_{LV} and N_{RV}. The increased HD errors in the comparative methods result from the use of a simple intensity threshold to distinguish between viable and non-viable tissue, that does not account for scar contiguity and image artifacts. Despite the low surface errors, the maximal average DSC over all methods compared was 0.76 for LV HMF segmentations, due to the typically thin and elongated appearance of myocardial scar and the known bias of the DSC towards volume size.

The clinically relevant volume errors reflect the results of the other metrics well. Pearson correlation of segmented volumes correlated well with manually segmented scar ($r_{LV} = 0.987, p < 0.001$ and $r_{RV} = 0.989, p < 0.001$). The comparative threshold-based volumes correlated less with $r_{FWHM} = 0.602$ ($p < 0.001$), and $r_{STRM3} = 0.856$ ($p < 0.001$) and $r_{STRM6} = 0.851$ ($p < 0.001$), respectively.

Neizel *et al* [21] reported an average infarct mass of $15 \pm 14g$ versus $19 \pm 15g$ by manual tracing, resulting in an average 21.05% error on 20 patients. Their calculated concordance correlation coefficient for scar masses was 0.94. For both N_{LV} and N_{RV} the HMF algorithm overestimates the volumes by $12.93 \pm 17.49\%$ and $8.86 \pm 14.69\%$, which might be due to regularization weights being set too high.

2.5.3 Operator variability

The repeatability experiments were performed using the clinically relevant scar volumes. The high intra-operator ICC values for both N_{LV} and N_{RV} volumes, show that there is a high agreement between users employing the proposed method for volume measurements. The slightly higher ICC for N_{RV} can be explained again by the presence of image artifacts in the mid-apical regions of the ventricle. Also the inter-operator ICC strongly suggested that there is low variability between users based on examined subset.

2.5.4 Effects of user interaction

Experiments determining the bias of repeated visual assessment and correction of seeds by a user showed that 2 of 10 datasets initially did not yield high accuracy results. These low results were due to respiratory ghosting artifacts and due to endocardial scar 'leaking' into the blood pool due to incorrect or insufficient seeding. However, the user was able to correct for these errors after 4 interactions. These results demonstrate, that user interaction is helpful to correct for inconsistencies and artifacts in the image and that after 5 interactions the proposed method was able to outperform all comparative methods in each dataset *without requiring prior myocardial segmentation masks*.

2.5.5 Comparative Methods

Model- or atlas-based segmentation methods

Because of excessive total time requirements, manual expert constraint segmentation is not an option for 3D WH LE-MRI. Two approaches found in the literature propose methods for scar segmentation on these images: Barbarito *et al.* [22] proposed an atlas-based and Neizel *et al.* [21] a model-based segmentation technique with subsequent intensity thresholding on the myocardial region. The FWHM V_p error shows that this technique is generally underestimating the scar volume. Since the scar can be modelled as a Gaussian distribution [12], the increased

sample size in 3D WH LE MRI leads to a more volatile maximum, hence a less reliable intensity threshold. In contrast, since the STRM-based methods do not rely on a single intensity maximum, their performance in terms of DSC is higher. In particular the STRM+6 method yields the lowest absolute volume error and highest DSC of all comparative methods. However, as shown in Figure 2.6 it can underestimate hyperenhanced regions. Accuracy results in Tables 2.4, 2.5 and 2.6 show that the proposed HMF-based method outperforms an idealized constraint segmentation and thresholding approach. Further, the example visual results in Figure 2.6 suggest that a simple thresholding technique might be insufficient to deal with artifacts and intensity inconsistencies commonly found in WH LE-MRI.

Discrete Graph-Cut Methods

The Potts modelled multi-region image segmentation problem can be also formulated over a specified discrete graph and solved by graph-cuts, for example alpha-expansion [57].

Such a discrete optimization approach, however, is known to have the following disadvantages: I) Grid bias is a metrication error that occurs due to the nature of the discrete graph resulted staircase-like boundaries; II) segmenting a 3D medical image often results in a huge 3D discrete graph and a high memory load and the popular approaches, such as the Boykov-Kolmogorov algorithm [57], cannot be fully implemented on parallel computing platforms, so cannot be accelerated to meet the requirements of most 3D medical imaging tasks.

On the other hand, the recently developed convex-relaxation technique, as proposed here, successfully avoids the existing difficulties of the classical graph-cuts and obtains a high numerical performance in practice. Additionally, the HMF regularizes each hierarchy level separately, allowing to account for the variations in smoothness of different objects, with minimal additional computational burden to a Potts model approach.

2.6 Conclusions

In conclusion, the proposed semi-automated algorithm is able to accurately segment myocardial scar tissue from WH LE-MR images without relying on constraint segmentations introducing additional sources of error. The avoidance of constraint segmentations opens its applications to other regions such as the right ventricle in patients presenting with scar after surgically repaired TOF. We demonstrated that, the HMF-based algorithm is able to outperform methods commonly found in the literature in terms of accuracy. In future studies, a generalized form of the hierarchical max-flow principle can potentially be adapted to solve other problems in medical image segmentation, where there is often prior knowledge of the appearance of anatomic regions and individual regularization of regions/labels is required. Lastly, the volume relationship of scar quantified from 2D and 3D LE-MRI remains unclear. Chapter 3 aims at shedding light on this missing link.

Bibliography

[1] Tevfik F Ismail, Sanjay K Prasad, and Dudley J Pennell. Prognostic importance of late gadolinium enhancement cardiovascular magnetic resonance in cardiomyopathy. *Heart*, 98(6):438–442, 2012.

[2] P. Gao, R. Yee, L. Gula, AD. Krahn, A. Skanes, P. Leong-Sit, GJ. Klein, J. Stirrat, N. Fine, L. Pallaveshi, G. Wisenberg, TR. Thompson, F. Prato, M. Drangova, and JA. White. Prediction of arrhythmic events in ischemic and dilated cardiomyopathy patients referred for implantable cardiac defibrillator. *Circulation: Cardiovascular Imaging*, 5(4):448–456, 2012.

[3] N.A. Marsan, J.J.M. Westenberg, C. Ypenburg, R.J. Van Bommel, S. Roes, V. Delgado, L.F. Tops, R.J. Van Der Geest, E. Boersma, A. De Roos, M.J. Schalij, and J.J. Bax. Magnetic resonance imaging and response to cardiac resynchronization therapy: Relative

merits of left ventricular dyssynchrony and scar tissue. *Eur Heart J*, 30(19):2360–2367, 2009.

[4] M Breeuwer, I Paetsch, E Nagel, R Muthupillai, S Flamm, S Plein, and J Ridgway. The detection of normal, ischemic and infarcted myocardial tissue using MRI. *International Congress Series*, 1256(0):1153 – 1158, 2003.

[5] Thomas P. O'Donnell, Ning Xu, Randolph M. Setser, and Richard D. White. Semi-automatic segmentation of nonviable cardiac tissue using cine and delayed enhancement magnetic resonance images. volume 5031, pages 242–251. SPIE, 2003.

[6] Engin Dikici, Thomas ODonnell, Randolph Setser, and Richard D White. Quantification of delayed enhancement mr images. In *Medical Image Computing and Computer-Assisted Intervention–MICCAI 2004*, pages 250–257. Springer, 2004.

[7] M.-P. Jolly, N. Duta, and G. Funka-Lea. Segmentation of the left ventricle in cardiac mr images. In *Computer Vision, 2001. ICCV 2001. Proceedings. Eighth IEEE International Conference on*, volume 1, pages 501 –508 vol.1, 2001.

[8] A. Kolipaka, G. P. Chatzimavroudis, R. D. White, T. P. O'Donnell, and R. M. Setser. Segmentation of non-viable myocardium in delayed enhancement magnetic resonance images. *Int J Cardiovas Imag*, 21(2-3):303–311, 2005.

[9] Vincenzo Positano, Alessandro Pingitore, Assuero Giorgetti, Brunella Favilli, Maria Filomena Santarelli, Luigi Landini, Paolo Marzullo, and Massimo Lombardi. A fast and effective method to assess myocardial necrosis by means of contrast magnetic resonance imaging. *Journal of Cardiovascular Magnetic Resonance*, 7(2):487–494, 2005.

[10] L. Y. Hsu, A. Natanzon, P. Kellman, G. A. Hirsch, A. H. Aletras, and A. E. Arai. Quantitative myocardial infarction on delayed enhancement MRI. part i: Animal validation of an automated feature analysis and combined thresholding infarct sizing algorithm. *J Magn Reson Imag*, 23(3):298–308, 2006.

[11] D. Säring, J. Ehrhardt, A. Stork, M. Bansmann, G. Lund, and H. Handels. Analysis of the left ventricle after myocardial infarction combining 4d cine-mr and 3D de-mr image sequences. In Heinz Handels, Jan Ehrhardt, Alexander Horsch, Hans-Peter Meinzer, and Thomas Tolxdorff, editors, *Bildverarbeitung fr die Medizin 2006*, Informatik aktuell, pages 56–60. Springer-Verlag, 2006.

[12] A. Hennemuth, A. Seeger, O. Friman, S. Miller, B. Klumpp, S. Oeltze, and H.-O. Peitgen. A comprehensive approach to the analysis of contrast enhanced cardiac mr images. *Medical Imaging, IEEE Transactions on*, 27(11):1592 –1610, 2008.

[13] Frank M. Bogun, Benoit Desjardins, Eric Good, Sanjaya Gupta, Thomas Crawford, Hakan Oral, Matthew Ebinger, Frank Pelosi, Aman Chugh, Krit Jongnarangsin, and Fred Morady. Delayed-enhanced magnetic resonance imaging in nonischemic cardiomyopathyutility for identifying the ventricular arrhythmia substrate. *Journal of the American College of Cardiology*, 53(13):1138–1145, 2009.

[14] H. Lehmann, R. Kneser, M. Neizel, J. Peters, O. Ecabert, H. Kühl, M. Kelm, and J. Weese. Integrating viability information into a cardiac model for interventional guidance. *Lecture Notes in Computer Science (including subseries Lecture Notes in Artificial Intelligence and Lecture Notes in Bioinformatics)*, 5528:312–320, 2009.

[15] Mirja Neizel, Marcus Katoh, Elisabeth Schade, Tienush Rassaf, Gabriele Krombach, Malte Kelm, and Harald Kühl. Rapid and accurate determination of relative infarct size in humans using contrast-enhanced magnetic resonance imaging. *Clinical Research in Cardiology*, 98:319–324, 2009. ISSN 1861-0684.

[16] K. Elagouni, C. Ciofolo-Veit, and B. Mory. Automatic segmentation of pathological tissues in cardiac MRI. In *Biomedical Imaging: From Nano to Macro, 2010 IEEE International Symposium on*, pages 472 –475, 2010.

[17] C. Ciofolo, M. Fradkin, B. Mory, G. Hautvast, and M. Breeuwer. Automatic myocardium

segmentation in late-enhancement MRI. In *Biomedical Imaging: From Nano to Macro, 2008. ISBI 2008. 5th IEEE International Symposium on*, pages 225 –228, May 2008.

[18] Qian Tao, Julien Milles, Katja Zeppenfeld, Hildo J. Lamb, Jeroen J. Bax, Johan H.C. Reiber, and Rob J. van der Geest. Automated segmentation of myocardial scar in late enhancement MRI using combined intensity and spatial information. *Magnetic Resonance in Medicine*, 64(2):586–594, 2010.

[19] Ahmed Elnakib, Garth Beache, Georgy Gimelfarb, and Ayman El-Baz. New automated markovgibbs random field based framework for myocardial wall viability quantification on agent enhanced cardiac magnetic resonance images. *The International Journal of Cardiovascular Imaging (formerly Cardiac Imaging)*, pages 1–16, 2011.

[20] Andrew S. Flett, Jonathan Hasleton, Christopher Cook, Derek Hausenloy, Giovanni Quarta, Cono Ariti, Vivek Muthurangu, and James C. Moon. Evaluation of techniques for the quantification of myocardial scar of differing etiology using cardiac magnetic resonance. *JACC: Cardiovascular Imaging*, 4(2):150–156, 2011.

[21] Mirja Neizel, Yang Boering, Florian Bonner, Jan Balzer, Malte Kelm, and Burkhard Sievers. A fully automatic cardiac model with integrated scar tissue information for improved assessment of viability. *Journal of Cardiovascular Magnetic Resonance*, 14(Suppl 1): M12, 2012.

[22] V. Barbarito, L. Carotenuto, L. Serra, O. Cmara, A. Frangi, J. Fernndez-Armenta, and A. Berruezo. A software application for three-dimensional visualization and quantification of scars and conducting channels based on pre-procedure CE-MRI in patients with ventricular tachycardia. In *Computer Assisted Radiology, 26th International Congress and Exhibition*, volume 7, pages 41–42. Springer, 2012.

[23] C. Tobon-Gomez, C. Butakoff, S. Aguade, F. Sukno, G. Moragas, and A.F. Frangi. Automatic construction of 3D-asm intensity models by simulating image acquisition: Ap-

plication to myocardial gated spect studies. *Medical Imaging, IEEE Transactions on*, 27 (11):1655 –1667, nov. 2008.

[24] R.J. Kim, D.S. Fieno, T.B. Parrish, K. Harris, E.L. Chen, O. Simonetti, J. Bundy, J.P. Finn, F.J. Klocke, and R.M. Judd. Relationship of MRI delayed contrast enhancement to irreversible injury, infarct age, and contractile function. *Circulation*, 100(19):1992–2002, 1999.

[25] Yasuo Amano, Yoshio Matsumura, and Shinichiro Kumita. Free-breathing high-spatial-resolution delayed contrast-enhanced three-dimensional viability mr imaging of the myocardium at 3.0 t: A feasibility study. *Journal of Magnetic Resonance Imaging*, 28(6): 1361–1367, 2008.

[26] Aya Kino, Sven Zuehlsdorff, John J Sheehan, Peter J Weale, Timothy J Carroll, Renate Jerecic, and James C Carr. Three-dimensional phase-sensitive inversion-recovery turbo flash sequence for the evaluation of left ventricular myocardial scar. *American Journal of Roentgenology*, 193(5):W381–W388, 2009.

[27] Kerstin U Bauner, Olaf Muehling, Daniel Theisen, Carmel Hayes, Bernd J Wintersperger, Maximilian F Reiser, and Armin M Huber. Assessment of myocardial viability with 3d mri at 3 t. *American Journal of Roentgenology*, 192(6):1645–1650, 2009.

[28] Kosuke Morita, Daisuke Utsunomiya, Seitaro Oda, Masanori Komi, Tomohiro Namimoto, Toshinori Hirai, Masahiro Hashida, Seiji Takashio, Megumi Yamamuro, and Yasuyuki Yamashita. Comparison of 3d phase-sensitive inversion-recovery and 2d inversion-recovery mri at 3.0 t for the assessment of late gadolinium enhancement in patients with hypertrophic cardiomyopathy. *Academic radiology*, 20(6):752–757, 2013.

[29] Magalie Viallon, Alexis Jacquier, Carmen Rotaru, Bénédicte Delattre, Nathan Mewton, Fabrice Vincent, and Pierre Croisille. Head-to-head comparison of eight late gadolinium-

enhanced cardiac mr (lge cmr) sequences at 1.5 tesla: From bench to bedside. *Journal of Magnetic Resonance Imaging*, 34(6):1374–1387, 2011.

[30] Hidenari Matsumoto, Tetsuya Matsuda, Kenichi Miyamoto, Kenji Nakatsuma, Masataka Sugahara, and Toshihiko Shimada. Feasibility of free-breathing late gadolinium-enhanced cardiovascular mri for assessment of myocardial infarction: Navigator-gated versus single-shot imaging. *International journal of cardiology*, 168(1):94–99, 2012.

[31] Mehmet Akçakaya, Hussein Rayatzadeh, Tamer A Basha, Susie N Hong, Raymond H Chan, Kraig V Kissinger, Thomas H Hauser, Mark E Josephson, Warren J Manning, and Reza Nezafat. Accelerated late gadolinium enhancement cardiac mr imaging with isotropic spatial resolution using compressed sensing: Initial experience. *Radiology*, 264 (3):691–699, 2012.

[32] Robert Goetti, Sebastian Kozerke, Olivio F Donati, Daniel Sürder, Paul Stolzmann, Philipp A Kaufmann, Thomas F Lüscher, Roberto Corti, and Robert Manka. Acute, subacute, and chronic myocardial infarction: quantitative comparison of 2d and 3d late gadolinium enhancement mr imaging. *Radiology*, 259(3):704–711, 2011.

[33] Steve Kecskemeti, Kevin Johnson, Christopher J François, Mark L Schiebler, and Orhan Unal. Volumetric late gadolinium-enhanced myocardial imaging with retrospective inversion time selection. *Journal of Magnetic Resonance Imaging*, 38(5):1276–1282, 2013.

[34] Jan Bogaert and Steven Dymarkowski. Ischemic heart disease. In *Clinical Cardiac MRI*, pages 203–273. Springer, 2012.

[35] Mushabbar A Syed and Raad H Mohiaddin. *Magnetic resonance imaging of congenital heart disease*. Springer, 2012.

[36] David Andreu, Antonio Berruezo, José T Ortiz-Pérez, Etelvino Silva, Lluis Mont, Roger Borràs, Teresa María de Caralt, Rosario Jesús Perea, Juan Fernández-Armenta, Hrvojka Zeljko, et al. Integration of 3d electroanatomic maps and magnetic resonance scar

characterization into the navigation system to guide ventricular tachycardia ablation. *Circulation: Arrhythmia and Electrophysiology*, 4(5):674–683, 2011.

[37] Juan Fernández-Armenta, Antonio Berruezo, David Andreu, Oscar Camara, Etelvino Silva, Luis Serra, Valeria Barbarito, Luigi Carotenutto, Reinder Evertz, José T Ortiz-Pérez, et al. Three-dimensional architecture of scar and conducting channels based on high resolution ce-cmr insights for ventricular tachycardia ablation. *Circulation: Arrhythmia and Electrophysiology*, 6(3):528–537, 2013.

[38] Simon G Duckett, Amedeo Chiribiri, Matthew R Ginks, Stephen Sinclair, Benjamin R Knowles, Rene Botnar, Gerry S Carr-White, Christopher A Rinaldi, Eike Nagel, Reza Razavi, et al. Cardiac mri to investigate myocardial scar and coronary venous anatomy using a slow infusion of dimeglumine gadobenate in patients undergoing assessment for cardiac resynchronization therapy. *Journal of Magnetic Resonance Imaging*, 33(1):87–95, 2011.

[39] Anoop K Shetty, Simon G Duckett, Matthew R Ginks, Yinglaing Ma, Manav Sohal, Julian Bostock, Stam Kapetanakis, Jagmeet P Singh, Kawal Rhode, Matthew Wright, et al. Cardiac magnetic resonance-derived anatomy, scar, and dyssynchrony fused with fluoroscopy to guide lv lead placement in cardiac resynchronization therapy: a comparison with acute haemodynamic measures and echocardiographic reverse remodelling. *European Heart Journal–Cardiovascular Imaging*, 14(7):692–699, 2013.

[40] J. A. White, N. Fine, L. J. Gula, R. Yee, M. Al-Admawi, Q. Zhang, A. Krahn, A. Skanes, A. MacDonald, T. Peters, and M. Drangova. Fused whole-heart coronary and myocardial scar imaging using 3-t cmr. implications for planning of cardiac resynchronization therapy and coronary revascularization. *JACC.Cardiovascular imaging*, 3(9):921–930, 2010.

[41] Martin Rajchl, Jing Yuan, James A White, Cyrus MS Nambakhsh, Eranga Ukwatta, Feng

Li, John Stirrat, and Terry M Peters. A fast convex optimization approach to segmenting 3d scar tissue from delayed-enhancement cardiac mr images. In *Medical Image Computing and Computer-Assisted Intervention–MICCAI 2012*, pages 659–666. Springer Berlin Heidelberg, 2012.

[42] N. Paragios. A variational approach for the segmentation of the left ventricle in cardiac image analysis. *International Journal of Computer Vision*, 50(3):345–362, 2002.

[43] K. Li, X. Wu, D.Z. Chen, and M. Sonka. Optimal surface segmentation in volumetric images-a graph-theoretic approach. *IEEE T. Pattern. Anal.*, 28(1):119–134, 2006.

[44] Andrew Delong and Yuri Boykov. Globally optimal segmentation of multi-region objects. In *International Conference on Computer Vision – ICCV*, pages 285–292, 2009.

[45] Wu Qiu, Jing Yuan, Eranga Ukwatta, Yue Sun, Martin Rajchl, and Aaron Fenster. Efficient 3d multi-region prostate mri segmentation using dual optimization. In *Information Processing in Medical Imaging*, pages 304–315. Springer Berlin Heidelberg, 2013.

[46] Eranga Ukwatta, Jing Yuan, Martin Rajchl, Wu Qiu, David Tessier, and Aaron Fenster. 3d carotid multi-region mri segmentation by globally optimal evolution of coupled surfaces. *IEEE Transactions on Medical Imaging*, 32(4):770–785, 2013.

[47] E. Bae, J. Yuan, X.-C. Tai, and Y. Boycov. A fast continuous max-flow approach to non-convex multilabeling problems. Technical report CAM-10-62, 2010.

[48] J. Ulen, P. Strandmark, and F. Kahl. An efficient optimization framework for multi-region segmentation based on lagrangian duality. *Medical Imaging, IEEE Transactions on*, 32 (2):178–188, 2013.

[49] M. Rajchl, J. Yuan, E. Ukwatta, and T.M. Peters. Fast interactive multi-region cardiac segmentation with linearly ordered labels. In *International Symposium on Biomedical Imaging (ISBI), 2012 International Conference on*. IEEE, 2012.

[50] A. Delong, L. Gorelick, F.R. Schmidt, O. Veksler, and Y. Boykov. Interactive segmentation with super-labels. In *EMMCVPR*, pages 147–162, 2011.

[51] Y.Y. Boykov and M.-P. Jolly. Interactive graph cuts for optimal boundary & region segmentation of objects in N-D images. In *Computer Vision, 2001. ICCV 2001. Proceedings. Eighth IEEE International Conference on*, volume 1, pages 105 –112, 2001.

[52] Jing Yuan, Egil Bae, Xue-Cheng Tai, and Yuri Boykov. A continuous max-flow approach to potts model. In *Computer Vision–ECCV 2010*, pages 379–392. Springer, 2010.

[53] J. Yuan, E. Bae, and X.C. Tai. A study on continuous max-flow and min-cut approaches. In *IEEE Computer Vision and Pattern Recognition – CVPR*, USA, San Francisco, 2010.

[54] Dimitri P. Bertsekas. *Nonlinear Programming*. Athena Scientific, September 1999. ISBN 1886529000.

[55] Antonin Chambolle. An algorithm for total variation minimization and applications. *Journal of Mathematical Imaging and Vision*, 20(1):89–97, January 2004.

[56] André Schmidt, Clerio F Azevedo, Alan Cheng, Sandeep N Gupta, David A Bluemke, Thomas K Foo, Gary Gerstenblith, Robert G Weiss, Eduardo Marbán, Gordon F Tomaselli, et al. Infarct tissue heterogeneity by magnetic resonance imaging identifies enhanced cardiac arrhythmia susceptibility in patients with left ventricular dysfunction. *Circulation*, 115(15):2006–2014, 2007.

[57] Y. Boykov, O. Veksler, and R. Zabih. Fast approximate energy minimization via graph cuts. *Pattern Analysis and Machine Intelligence, IEEE Transactions on*, 23(11):1222–1239, 2001.

Chapter 3

Comparison of Semi-automated Scar Quantification Techniques Using High-Resolution, 3-Dimensional Late-Gadolinium-Enhancement Magnetic Resonance Imaging

3.1 Introduction

Over the past decade, LE cardiac magnetic resonance (CMR) imaging has established itself as a preferred imaging tool for the characterization of myocardial fibrosis or 'scar' [1]. While conventionally performed using sequential 2D image acquisition during separate breath holds,

This Chapter is adapted from an article currently in revision. M. Rajchl, J. Stirrat, M. Goubran, J. Yu, D. Scholl, T.M. Peters and J.A. White (2014). *Comparison of Semi-automated Scar Quantification Techniques Using High-Resolution, 3-Dimensional Late-Gadolinium-Enhancement Magnetic Resonance Imaging.* The International Journal of Cardiovascular Imaging.

free-breathing 3D WH LGE imaging techniques have now become available in the clinical setting. Further, improvements aimed at substantial reduction in image acquisition time favour 3D free-breathing LE as a practical alternative to 2D breath-held acquisition [2, 3, 4, 5]. This migration provides capacity for superior volumetric characterization of myocardial scar at isotropic resolutions approaching $1mm^3$, affording high-quality multi-planar reconstruction, improved anatomic registration, and the potential for accurate volumetric scar quantification and modelling [6, 7, 8, 9, 10, 11]. Such advancements have been primarily pursued to support expanding interest in image-guided therapy, particularly related to the use of scar-based modelling to guide electrophysiology-based procedures, such as; CRT and catheter-based ablation of both ventricular and atrial tachyarrhythmia [6, 7, 8, 9, 10, 11, 12, 13]. A superiority of WH LE over conventional 2D LE sequences has been shown by several recent studies, reporting an improvement in myocardial lesion discrimination, scar signal intensity (SI) and image contrast [14, 15]. In addition, improved image quality [15] and superior diagnostic scores have been attested to this approach [14, 16]. Despite such advantages, the capacity to segment myocardial scar signal from isotropic 3D datasets remains challenging and, while 2D signal segmentation techniques have been explored for their accuracy and reproducibility [17], no such studies have explored 3D imaging approaches. Given inherently different signal-to-noise characteristics attributed by differing k-space ordering, smaller voxel size, and altered signal gradients, the performance of these techniques cannot be assumed to be similar. Further, as existing segmentation techniques commonly sample reference tissue (healthy or scarred) these values will be altered by an expansion in voxel count and reduction in partial volume effects (particularly in the z-axis), leading to a more volatile (i.e. higher) peak signal and lowering of standard deviation estimates. As such, novel standards for scar segmentation using 3D datasets are required. In this study, we conduct a series of experiments to compare semi-automated segmentation methods and determine the optimal technique for quantification of ischemic myocardial scar using 3D isotropic LE imaging. Complementary to the work by Flett, et al. establishing standards for 2D LE segmentation [17], we systematically compare all

known segmentation techniques for both their accuracy and reproducibility. Comparisons are made against the gold standard of expert manual 3D segmentation and cross-correlation of all techniques to conventional 2D LE scar quantification is performed.

3.2 Methods

3.2.1 Patient population

Thirty-five consecutive patients with known ischemic cardiomyopathy, defined as prior myocardial infarction and an LV ejection fraction <50%, referred for LE CMR at the Cardiovascular MRI Clinical Research (CMCR) Centre were recruited. Patients with standard contraindications to cardiac magnetic resonance (CMR) or with a glomerular filtration rate ≤ 30 ml/min/1.73 m^2 were excluded. All patients provided written informed consent, and the study protocol was approved by Western Universitys Research Ethics Board. Image acquisition

All patients underwent an imaging protocol using a 3-Tesla CMR scanner (TRIO, or Verio, Siemens Medical Systems, Erlangen, Germany) using a 32-channel phased-array radiofrequency coil. Cine functional imaging was performed in a standard fashion using a steady state free precession based (SSFP) pulse sequence (TrueFISP) in sequential short-axis slices from the atrioventricular annulus to the left ventricular apex at 10 mm intervals, and in long-axis orientations (slice thickness 6 mm, gap 4 mm, echo time 1.5 ms, repetition time 3.0 ms, flip angle 50°). A 3D whole-heart, inversion-recovery gradient echo pulse sequence with a respiratory navigator pulse placed over the right hemidiaphragm was used to obtain both an early (coronary-enhanced) and late (scar-enhanced) dataset (voxel size 1.3 x 1.3 x 1.3 mm^3, resampled to 0.625 x 0.625 x 1.3 mm^3, echo time 1.3 ms, flip angle 20°, integrated parallel acquisition technique (iPAT) 2). Fat saturation was employed to suppress pericardial fat signal. Imaging volumes were prescribed in the transverse plane from the aortic arch to below the most inferior aspect of the heart (slab thickness 120 to 144 slices) based on multiplanar scout images. Adjustment of trigger delay and number of segments was performed to maintain

image acquisition between the onset and termination of cardiac standstill, as determined from the 4-chamber cine. For coronary-enhanced imaging, an intravenous infusion of 0.2 mmol/kg gadolinium (Gadovist, Bayer Inc., Toronto, Ontario, Canada) was given at 0.3 ml/s, followed by 40 ml of saline at the same rate. Imaging was initiated 25 sec following infusion onset, as previously described [5]. A repeat (scar-enhanced) dataset was then acquired 20 min later, with adjustment of the inversion time (TI) to provide optimal myocardial signal suppression. The TI was set at 200 ms for coronary-enhanced imaging and was adjusted for scar-enhanced imaging (typical range 240 to 280ms). These adjustments were performed using a test-image slab (10-mm thickness) acquired over the mid-ventricle. A series of standard short-axis 2D LE images was obtained between coronary-enhanced and scar-enhanced 3D imaging. This was performed using a standard phase-sensitive inversion recovery pulse sequence (matrix 256 192, slice thickness 6 mm, gap 4 mm).

3.2.2 2-Dimensional scar analysis

Conventional 2D LE images were analyzed according to 5 previously described segmentation techniques. This included the STRM approach, using thresholds defined at >2SD, >3SD, >4SD, and >6SD above reference remote myocardium (manually defined), and the FWHM approach where scar is defined as signal exceeding 50% of the maximal signal intensity for manually labelled scar regions, as previously described [17]. All 2D LE analysis was performed by a blinded and experienced clinician using commercially available software (CVI 42, Circle Imaging, Calgary, AB), and was performed using sequential short-axis views (SAX) views. Manual tracing of the endocardial and epicardial contours was performed followed by the manual exclusion of image artifacts, when present, and labelling of the reference myocardium (on all slices) and scar region. Total scar volume was reported in ml and as a percentage of LV volume for each of the five segmentation techniques.

3.2.3 3-Dimensional scar analysis

All 3D datasets were analyzed in accordance with the same five thresholding techniques reported for 2D imaging, and also using a new 3D segmentation approach. Similar to 2D image analysis demarcation of the endocardial and epicardial borders is required. As the manual segmentation of endocardial and epicardial borders on isotropic datasets is impractical to perform we used a locally-developed, interactive segmentation algorithm to identify these myocardial borders [18], followed by manual refinement by an experienced cardiac imager (J.A.W). Valvular tissue, papillary muscles, and/or mural thrombus, if present, were carefully excluded from the segmentation. User defined regions of interest were placed over reference (normal) myocardium and peak scar signal on a multi-planar reformatted (MPR) image using a 3D brush tool [19]. Constrained to the myocardium a 3D segmentation was then performed using MATLAB 2010b (MathWorks, Natick, MA) to identify myocardial scar using both the STRM and FWHM techniques. Incrementally, a novel semi-automated technique for the segmentation of myocardial scar from 3D LE images was tested. This technique is presented in Chapter 2 and based on HMF optimization [20, 21] and does not require prior segmentation of myocardial borders. This approach identifies scar based its unique signal spectrum relative to both the myocardium and blood pool, requiring a user to interactively sample each tissue via brush strokes. Again, scar volumes were reported in units of ml and also expressed as a percentage of total LV volume.

3.2.4 Inter-observer and Intra-observer Reproducibility

Inter-observer and intra-observer reproducibility for scar volume measurements was performed for each of the 3D segmentation techniques. This involved a first investigator performing scar segmentation for all cases on two separate occasions, with a second investigator repeating the same measurements in random order to provide for inter- and intra-observer variability testing, respectively.

3.2.5 Statistical Analysis

Continuous variables are expressed as mean ± SD, while medians with 25th and 75th percentiles are provided for non-normally distributed data. Categorical variables are expressed as simple proportions. To validate the accuracy of 3D scar quantification techniques several analyses are reported. First, the Pearson correlation coefficients of total scar volume estimates for each of the respective techniques are reported against the gold standard of expert manual segmentation. Second, Bland-Altman analysis is reported to express the mean bias of each technique versus the gold standard. Absolute volume differences (δV_E) are similarly reported. Third, the Dice Similarity coefficient is calculated as a measure of mean region overlap between each techniques segmented region (R_A) and the gold standard segmented region (R_B). All 3D quantification techniques are compared against conventional 2D scar analysis techniques in terms of their bias using Bland-Altman analysis.

To assess intra- and inter-observer variability, the ICCs are calculated on the repeatedly quantified scar volumes. All analyses were performed using SPSS 20 (IBM Corp., New York) and Graph Pad Prism 6 (GraphPad Inc., La Jolla, CA).

3.3 Results

All thirty-five patients completed the imaging protocol. Baseline patient characteristics are shown in Table 3.1 and show a mean age of 51.5 ± 12.6. The mean heart rate at time of imaging was 67.1 ± 11.2 b/min.

3.3.1 Baseline CMR Characteristics and 2D Scar Segmentation Analysis

The mean age and ejection fraction of the population was 51.5 ± 12.6 years and 32.1 ± 12.7%, respectively. By conventional 2D LE, image scar segmentation the mean total scar volume was 23.1 ± 12.3% (range 1.2 to 43.2%) using an STRM >5SD threshold and 19.2 ± 8.5% (range 0.1 to 32.3%) using the FWHM technique.

Characteristics	Total population (N = 35)
Age (years)	51.5 ± 12.6
Male, n(%)	29 (82.8%)
BMI (kg/m^2)	28.2 ± 4.7
HR (bpm)	67.1 ± 11.2
GFR (ml/min)	83.5 ± 20.9
Prior revascularization, n (%)	9 (25.7%)
LV EF (%)	32.1 ± 12.7
LV EDV (ml)	228.7 ± 69.3
LV ESV (ml)	160.5 ± 72.5
RV EF (%)	51.2 ± 11.7

Table 3.1: Baseline characteristics of all included patients. Plus-minus values are means ± standard deviation. Abbreviations used: BMI: body mass index, HR: heart rate, GFR: glomerular filtration rate, LV EF: Left ventricular ejection fraction, LV EDV: Left-ventricular end-diastolic volume, LV ESV: Left-ventricular end-systolic volume, RV EF: Right-ventricular ejection fraction.

3.3.2 3D Scar Segmentation Analysis

3D LE image quality was scored as good or excellent in 34/35 (97%) of patients. One patient demonstrated severe breathing artifacts, introduced by coughing during acquisition, and required exclusion from final analysis. A typical example of 3D LE imaging data is provided in Figure 3.1. Gold standard manual 3D segmentation showed a mean total scar volume for the entire population of 11.4 ± 6.6% (range 1.1 to 24.8%). Pearson correlation estimates of total scar volume for each 3D segmentation technique versus the gold standard are shown in Table 3.2. The highest correlation was seen for the HMF technique with a correlation coefficient of 0.99 (p <0.0001), followed by the STRM >5 SD technique (r= 0.92, p <0.0001). The lowest mean bias among all techniques was seen for the STRM >6 SD technique (2.11 ± 10.23, 95% CI -17.85 to 22.25) (Table 3.2), however the HMF method presented with lower bias SD and tighter CI (3.36 ± 4.25, 95% CI -4.97 to 11.68). The highest DSC and lowest absolute volume difference (δV_E) was similarly found with the HMF technique (76±3.6% and 4.1 ± 3.6 ml respectively). The next best performing 3D segmentation technique was STRM >6 SD (DSC 68.0±12.7% and δV_E 8.1±6.5 ml). Respective results for all 3D scar quantification experiments are reported in Table 3.2. An example of all segmentation technique results in a

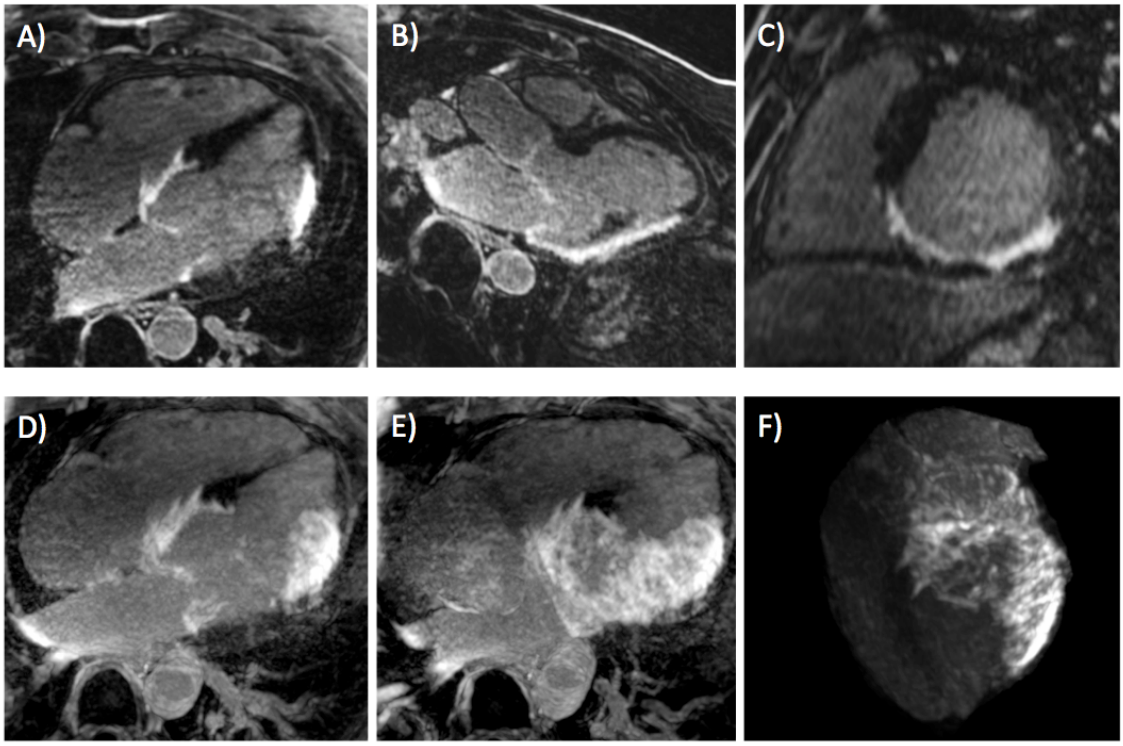

Figure 3.1: Example 3D Late Gadolinium Enhancement (LE) image dataset acquired in a 46yo male referred for recurrent sustained ventricular tachycardia late following myocardial infarction. Electrophysiologic mapping and curative ablation procedure confirmed a scar re-entry circuit with an exit site in heterogeneous scar occupying the mid inferoseptal wall. Top row: Multi-planar reformatted (MPR) images in 4-chamber (A), 3-chamber (B), and short axis mid-ventricular (B) views. Lower row: Maximum intensity projections (MIP) shown in a 10mm axial slab (D), 30mm axial slab (E), and 100mm anterior-posterior projection (F). The latter is shown with the cropping of extraneous, non-cardiac signal.

representative patient is shown in Figure 3.2.

3.3.3 3D Inter-observer and Intra-observer Reproducibility

All 3D segmentation approaches showed high intra-observer reproducibility. Intra-observer ICC values ranged from 0.95 and 0.97, as shown in Table 3.3, with the HMF method having highest reproducibility (ICC 0.97). Both HMF and FHWM outperformed STRM in terms of inter-observer reproducibility (ICC 0.95). However, FWHM showed an improved lower boundary of the 95% confidence interval (0.91).

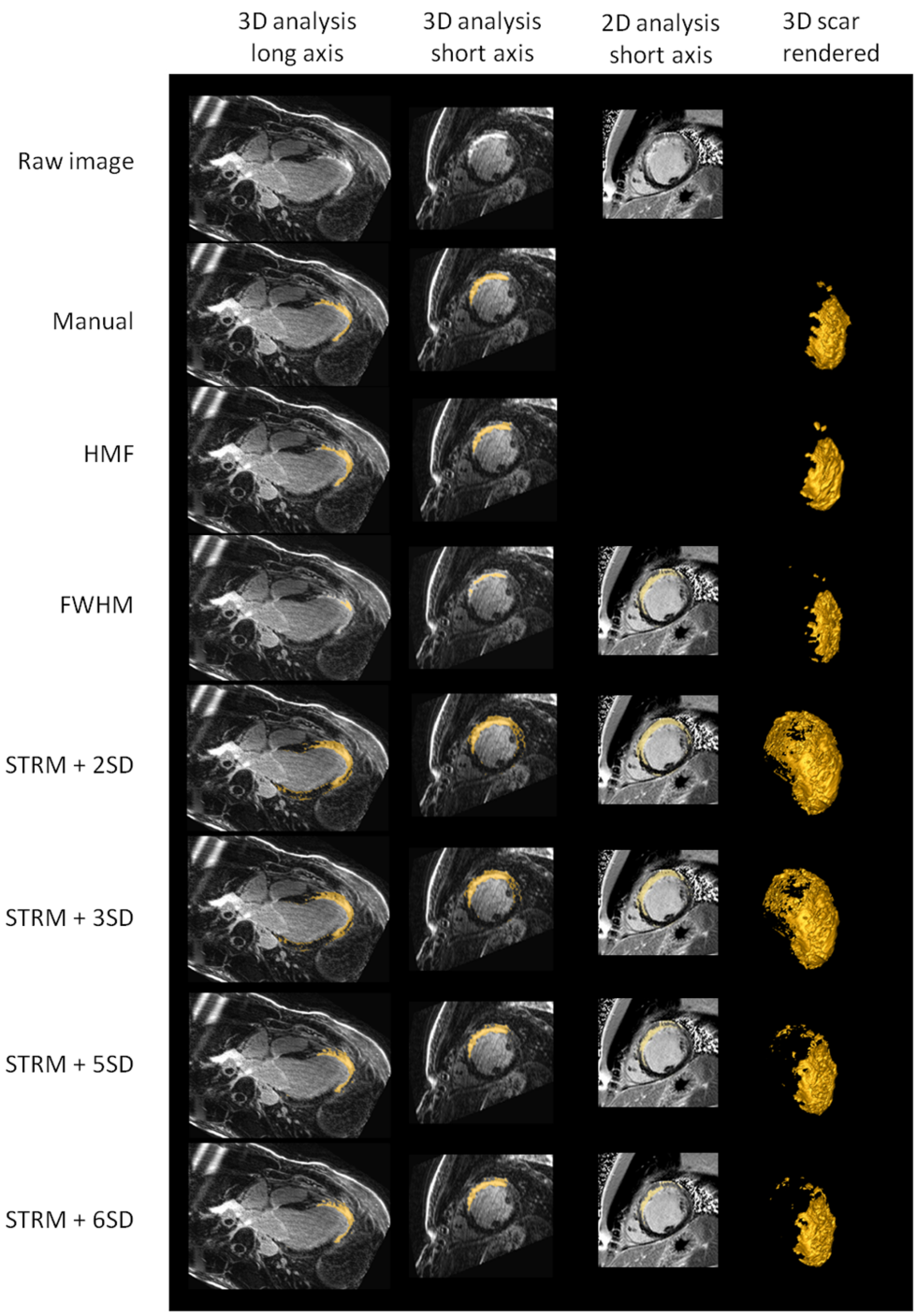

Figure 3.2: Example of all 3D scar quantification techniques applied to a dataset with a large, transmural myocardial infarction of the left anterior descending artery territory. Multi-planar reformatted results of both manual (gold standard) and all semi-automated scar segmentation techniques are shown in long axis (column 1) and short-axis (column 2) views. Corresponding segmentation of 2D LE imaging is shown in column 3. Finally, volume renderings of 3D segmented scar volumes are shown in column 4.

	Validation metrics			Bland-Altman analysis	
	DSC (%)	δV_E (ml)	Pearson r	Bias (SD)	95% CI
FWHM	58.6 ± 13.7	12.8 ± 14.8	0.68*	-11.99 (15.47)	-42.31 to 18.33
STRM >2SD	43.5 ± 17.0	57.0 ± 20.2	0.85*	56.98 (20.16)	17.47 to 96.5
STRM >3SD	53.5 ± 17.0	34.6 ± 14.7	0.89*	34.57 (14.68)	5.80 to 63.34
STRM >5SD	67.1 ± 12.9	11.3 ± 8.1	0.92*	9.74 (10.03)	-9.91 to 29.4
STRM >6SD	68.0 ± 12.7	8.1 ± 6.5	0.90*	2.20 (10.23)	-17.85 to 22.25
HMF	76.0 ± 3.6	4.1 ± 3.6	0.99*	3.36 (4.25)	-4.97 to 11.68

Table 3.2: Comparison of all 3D scar segmentation techniques against the gold standard of expert manual segmentation. Mean regional overlap DSC [%], Absolute volume difference δV_E [ml] and Pearson correlation coefficient(r) of segmented volumes are provided. * p-value<0.0001 STRM = Signal Threshold versus Reference Mean, FWHM = Full Width Half of Maximum, HMF = Hierarchical Max Flow, SD = Standard Deviation

	Reproducibility	
	Inter-observer ICC [0,1] (95% CI)	Intra-observer ICC [0,1] (95% CI)
FWHM	0.95 (0.91-0.97)	0.96 (0.93-0.98)
STRM >2SD	0.76 (0.58-0.87)	0.95 (0.90-0.97)
STRM >3SD	0.80 (0.64-0.90)	0.96 (0.92-0.98)
STRM >5SD	0.84 (0.71-0.92)	0.96 (0.92-0.98)
STRM >6SD	0.83 (0.69-0.91)	0.95 (0.90-0.97)
HMF	0.95 (0.87-0.98)	0.97 (0.94-0.98)

Table 3.3: Inter- and intra-observer reproducibility expressed by Intraclass Correlation Coefficient (ICC, single measure of absolute agreement) with 95% confidence intervals (CI), reported for all 3D scar quantification techniques. STRM = Signal Threshold versus Reference Mean, FWHM = Full Width Half of Maximum, HMF = Hierarchical Max Flow, SD = Standard Deviation

3.3.4 Comparison of 3D versus 2D LE Scar quantification

A comparison of 3D versus 2D segmentation data is presented in Table 3.4. Compared against the gold standard of 3D manual segmentation, the 2D STRM >5SD scar segmentation technique yielded the lowest mean absolute bias (3.6 ± 12.5 ml, 95% CI -20.9 to 28.1), consistent with it providing the best accuracy for estimation of total 3D scar burden. When comparing 2D versus 3D approaches of the same segmentation technique a positive bias was evident with 3D versus the respective 2D approach using STRM-based thresholds, this bias reducing with increasing threshold level (ranging from 47.1 ml at a >2SD threshold down to 7.2 ml at a >6SD threshold). Conversely, a more modest negative bias was seen with 3D versus 2D FWHM

3D	FWHM	STRM >2 SD	STRM >3 SD	STRM >5 SD	STRM >6 SD	HMF	MANUAL
2D	Bias (SD)	Bias (SD)	Bias (SD)	Bias (SD)	Bias (SD)	Bias (SD)	Bias (SD)
FWHM	-5.6 ± 14.7	63.4 ± 28.4	41.0 ± 23.5	16.1 ± 18.2	8.6 ± 16.7	9.8 ± 17.6	6.4 ± 15.9
STRM >2 SD	-21.8 ± 15.7	47.2 ± 24.5	24.8 ± 19.3	-0.1 ± 14.7	-7.6 ± 14.3	-6.5 ± 11.7	-9.8 ± 11.1
STRM >3 SD	-16.5 ± 15.8	52.5 ± 25.2	30.1 ± 19.9	5.2 ± 14.9	-2.3 ± 14.3	-1.1 ± 12.2	-4.5 ± 11.7
STRM >5 SD	-8.4 ± 14.7	60.6 ± 26.4	38.2 ± 21.0	13.4 ± 15.3	5.8 ± 14.2	7.0 ± 13.6	3.6 ± 12.5
STRM >6 SD	-7.0 ± 14.0	62.0 ± 26.4	39.6 ± 20.7	14.7 ± 14.4	7.2 ± 12.8	8.4 ± 14.1	5.0 ± 12.8

Table 3.4: Comparison of 3D versus conventional 2D Total Scar volume quantification using all available segmentation algorithms. Results shown represent the mean bias (in mL) and standard deviation (SD)between the respective techniques, as derived by Bland-Altman analysis. STRM = Signal Threshold versus Reference Mean, FWHM = Full Width Half of Maximum, HMF = Hierarchical Max Flow, SD = Standard Deviation

segmentation techniques (5.6 ml). As HMF segmentation is only applied to 3D imaging no comparison was available for this technique.

3.4 Discussion

3D LE imaging is attractive due to its superior spatial coverage, anatomic registration and capacity for more accurate volumetric characterization of myocardial scar. For these benefits to be fully realized, semi-automated quantification techniques with the capacity for efficient and reproducible scar segmentation are required. This study is the first to systematically compare the accuracy and reproducibility of conventional signal threshold-based techniques for the quantification of myocardial scar from 3D LE images, and a recent technique not reliant upon prior boundary tracing.

Our results indicate that, consistent with prior 2D LE scar segmentation studies [17], higher STRM-based thresholds provide improved accuracy for scar volume estimates. A >6SD threshold provided the greatest DSC of 76% and lowest δV_E of 4.1 ml, whereas a >2SD threshold provided a mean δV_E of 57 ml, respectively. While FWHM techniques have been shown to have high accuracy for 2D LE datasets [17], our findings show this approach performs only modestly for 3D LE segmentation (DSC of 58.6% and δV_E of 14.8 ml). The FWHM technique showed a systematic under-estimation of myocardial scar volumes (mean bias -11 ml, 95% CI -14 to 18ml) versus the gold standard. This finding can be explained its sampling of a single

peak (rather than mean) signal intensity reference value from this Gaussian distributed data (see [22]). This inherently achieves higher peak estimates when translated to 3D datasets due to a markedly increased voxel sample size (i.e. more than 7-fold), raising corresponding thresholds for scar labelling. Further, it must be recognized that 3D LE techniques generate higher SNR of scarred regions when compared to conventional 2D LE imaging [14], potentially contributing to the altered performance of the FWHM approach.

The reproducibility of STRM versus FWHM-based scar segmentation approaches has been well described for 2D scar segmentation [22, 23]. We found similar findings for 3D scar segmentation with the FWHM technique providing high reproducibility. For example, the ICC for intra-observer variability was 96% for FWHM versus 95% for STRM >6SD and 95% for STRM >2SD segmentations, and the ICC for intra-observer variability was 95% for FWHM versus 83% for STRM >6SD and 76% for STRM >2SD, respectively.

In this study we incrementally tested a recent HMF segmentation algorithm for 3D scar segmentation. This approach was found to match the superior reproducibility metrics of the FWHM approach while achieving improved accuracy (DSC of 76.0% and δV_E of 4.1ml) relative to the optimal STRM-based >6SD segmentation approach. Because prior segmentation of the endocardial and epicardial borders are not required in the HMF technique, its accuracy and reproducibility are further complemented by marked improvements in workflow efficiency. For example, we found the time required for myocardial contour tracing and reference tissue labelling to be 54.7 ± 17.6 and 1.4 ± 0.6 min, respectively. By comparison, the total analysis time using the HMF approach was 6.5 ± 2.3 min, primarily related to the elimination of semi-automated myocardial boundary segmentation and related manual adjustments.

3.4.1 Limitations

Inter- and intra-observer reproducibility of threshold-based (STRM and FWHM) 3D scar quantification was performed using the same myocardial border constraints, as defined by semi-automated myocardial segmentation. Therefore, this reproducibility testing focused on the ef-

fect of manual reference region selection, rather than all aspects of the segmentation pipeline. This was necessary for study feasibility as the time required for manual adjudication of endocardial and epicardial borders throughout the 3D volume precluded it being done repeatedly for all 5 threshold-based approaches. However, as this common operation must be performed in the same fashion prior to each approach, we believe that relative differences in their performance are appropriately represented by this study design. This study investigated the role of scar quantification in patients with ischemic cardiomyopathy. As such, further validation work is required for patients with non-ischemic cardiomyopathy. Translation of these findings to the latter population cannot be recommended. Finally, it must be acknowledged that manual segmentations of scar signal from 3D LE MRI represents a surrogate of ground truth and that histological validation (i.e.: animal model design) would be preferred for accuracy estimates. However, volumetric quantification of complex scar architecture from histopathology poses its own unique challenges and such techniques are currently unavailable. Further, post-mortem validation of in-vivo scar volume is incrementally challenged by the disparate respective physiologic states. Accordingly, the manual segmentation of 3D scar architecture remains the most appropriate gold standard.

3.5 Conclusions

Volumetric quantification of scar from 3D LE datasets is clinically feasible and can be performed using both STRM and FWHM-based signal threshold techniques. Our findings support that STRM-based segmentation has improved accuracy at higher thresholds (i.e.: >5SD or >6SD) with acceptable intra- and inter-observer reproducibility. However, while an FWHM-based approach provides superior reproducibility, it lacks accuracy with systematic underrepresentation of both scar volume and architecture. Recent segmentation algorithms, such as HMF, may be preferred for such datasets with a combined achievement of optimal accuracy and reproducibility along with a substantial reduction in image processing time. The imple-

mentation of such image processing tools is required for appropriate exploitation of 3D scar imaging for the guidance of therapeutic procedures, particularly those reliant upon accurate representation of scar characteristics.

Bibliography

[1] John Stirrat and James A White. The prognostic role of late gadolinium enhancement magnetic resonance imaging in patients with cardiomyopathy. *Canadian Journal of Cardiology*, 29(3):329–336, 2013.

[2] Robert Goetti, Sebastian Kozerke, Olivio F Donati, Daniel Sürder, Paul Stolzmann, Philipp A Kaufmann, Thomas F Lüscher, Roberto Corti, and Robert Manka. Acute, subacute, and chronic myocardial infarction: quantitative comparison of 2D and 3D late gadolinium enhancement MR imaging. *Radiology*, 259(3):704–711, 2011.

[3] Steve Kecskemeti, Kevin Johnson, Christopher J François, Mark L Schiebler, and Orhan Unal. Volumetric late gadolinium-enhanced myocardial imaging with retrospective inversion time selection. *Journal of Magnetic Resonance Imaging*, 38(5):1276–1282, 2013.

[4] Jennifer Keegan, Permi Jhooti, Sonya V Babu-Narayan, Peter Drivas, Sabine Ernst, and David N Firmin. Improved respiratory efficiency of 3D late gadolinium enhancement imaging using the continuously adaptive windowing strategy (CLAWS). *Magnetic Resonance in Medicine*, 2013.

[5] James A White, Nowell Fine, Lorne J Gula, Raymond Yee, Mohammed Al-Admawi, Qi Zhang, Andrew Krahn, Allan Skanes, Anna MacDonald, Terry Peters, et al. Fused whole-heart coronary and myocardial scar imaging using 3-T CMRI. mplications for planning of cardiac resynchronization therapy and coronary revascularization. *JACC: Cardiovascular Imaging*, 3(9):921–930, 2010.

[6] Simon G Duckett, Amedeo Chiribiri, Matthew R Ginks, Stephen Sinclair, Benjamin R Knowles, Rene Botnar, Gerry S Carr-White, Christopher A Rinaldi, Eike Nagel, Reza Razavi, et al. Cardiac MRI to investigate myocardial scar and coronary venous anatomy using a slow infusion of dimeglumine gadobenate in patients undergoing assessment for cardiac resynchronization therapy. *Journal of Magnetic Resonance Imaging*, 33(1):87–95, 2011.

[7] Juan Fernández-Armenta, Antonio Berruezo, David Andreu, Oscar Camara, Etelvino Silva, Luis Serra, Valeria Barbarito, Luigi Carotenutto, Reinder Evertz, José T Ortiz-Pérez, et al. Three-dimensional architecture of scar and conducting channels based on high resolution CE-CMR: Insights for ventricular tachycardia ablation. *Circulation: Arrhythmia and Electrophysiology*, 6(3):528–537, 2013.

[8] Christian Sohns, Rashed Karim, James Harrison, Aruna Arujuna, Nick Linton, Richard Sennett, Hendrik Lambert, Giovanni Leo, Steven Williams, Reza Razavi, et al. Quantitative magnetic resonance imaging analysis of the relationship between contact force and left atrial scar formation after catheter ablation of atrial fibrillation. *Journal of cardiovascular electrophysiology*, 2013.

[9] Ganesh Adluru, Liyong Chen, Seong-Eun Kim, Nathan Burgon, Eugene G Kholmovski, Nassir F Marrouche, and Edward VR DiBella. Three-dimensional late gadolinium enhancement imaging of the left atrium with a hybrid radial acquisition and compressed sensing. *Journal of Magnetic Resonance Imaging*, 34(6):1465–1471, 2011.

[10] Gaston R Vergara and Nassir F Marrouche. Tailored management of atrial fibrillation using a LGE-MRI based model: From the clinic to the electrophysiology laboratory. *Journal of cardiovascular electrophysiology*, 22(4):481–487, 2011.

[11] Anoop K Shetty, Simon G Duckett, Matthew R Ginks, Yinglaing Ma, Manav Sohal, Julian Bostock, Stam Kapetanakis, Jagmeet P Singh, Kawal Rhode, Matthew Wright, et al.

Cardiac magnetic resonance-derived anatomy, scar, and dyssynchrony fused with fluoroscopy to guide lv lead placement in cardiac resynchronization therapy: a comparison with acute haemodynamic measures and echocardiographic reverse remodelling. *European Heart Journal–Cardiovascular Imaging*, 14(7):692–699, 2013.

[12] David Andreu, Antonio Berruezo, José T Ortiz-Pérez, Etelvino Silva, Lluis Mont, Roger Borràs, Teresa María de Caralt, Rosario Jesús Perea, Juan Fernández-Armenta, Hrvojka Zeljko, et al. Integration of 3d electroanatomic maps and magnetic resonance scar characterization into the navigation system to guide ventricular tachycardia ablation. *Circulation: Arrhythmia and Electrophysiology*, 4(5):674–683, 2011.

[13] Kosuke Morita, Daisuke Utsunomiya, Seitaro Oda, Masanori Komi, Tomohiro Namimoto, Toshinori Hirai, Masahiro Hashida, Seiji Takashio, Megumi Yamamuro, and Yasuyuki Yamashita. Comparison of 3d phase-sensitive inversion-recovery and 2D inversion-recovery MRI at 3.0 T for the assessment of late gadolinium enhancement in patients with hypertrophic cardiomyopathy. *Academic radiology*, 20(6):752–757, 2013.

[14] Magalie Viallon, Alexis Jacquier, Carmen Rotaru, Bénédicte Delattre, Nathan Mewton, Fabrice Vincent, and Pierre Croisille. Head-to-head comparison of eight late gadolinium-enhanced cardiac MR (LGE CMR) sequences at 1.5 Tesla: From bench to bedside. *Journal of Magnetic Resonance Imaging*, 34(6):1374–1387, 2011.

[15] Hidenari Matsumoto, Tetsuya Matsuda, Kenichi Miyamoto, Kenji Nakatsuma, Masataka Sugahara, and Toshihiko Shimada. Feasibility of free-breathing late gadolinium-enhanced cardiovascular MRI for assessment of myocardial infarction: Navigator-gated versus single-shot imaging. *International journal of cardiology*, 168(1):94–99, 2013.

[16] Mehmet Akçakaya, Hussein Rayatzadeh, Tamer A Basha, Susie N Hong, Raymond H Chan, Kraig V Kissinger, Thomas H Hauser, Mark E Josephson, Warren J Manning, and Reza Nezafat. Accelerated late gadolinium enhancement cardiac MR imaging with

isotropic spatial resolution using compressed sensing: initial experience. *Radiology*, 264 (3):691, 2012.

[17] Andrew S Flett, Jonathan Hasleton, Christopher Cook, Derek Hausenloy, Giovanni Quarta, Cono Ariti, Vivek Muthurangu, and James C Moon. Evaluation of techniques for the quantification of myocardial scar of differing etiology using cardiac magnetic resonance. *JACC: cardiovascular imaging*, 4(2):150–156, 2011.

[18] Martin Rajchl, Jing Yuan, Eranga Ukwatta, and PM Peters. Fast interactive multi-region cardiac segmentation with linearly ordered labels. In *Biomedical Imaging (ISBI), 2012 9th IEEE International Symposium on*, pages 1409–1412. IEEE, 2012.

[19] Paul A Yushkevich, Joseph Piven, Heather Cody Hazlett, Rachel Gimpel Smith, Sean Ho, James C Gee, and Guido Gerig. User-guided 3D active contour segmentation of anatomical structures: significantly improved efficiency and reliability. *Neuroimage*, 31 (3):1116–1128, 2006.

[20] Martin Rajchl, Jing Yuan, James A White, Cyrus MS Nambakhsh, Eranga Ukwatta, Feng Li, John Stirrat, and Terry M Peters. A fast convex optimization approach to segmenting 3D scar tissue from delayed-enhancement cardiac MR images. In *Medical Image Computing and Computer-Assisted Intervention–MICCAI 2012*, pages 659–666. Springer, 2012.

[21] M. Rajchl, J. Yuan, J. White, E. Ukwatta, J. Stirrat, C. Nambakhsh, F. Li, and T. Peters. Interactive hierarchical max-flow segmentation of scar tissue from late-enhancement cardiac MR images. *IEEE Transactions on Medical Imaging*, 33(1):159–172, 2014.

[22] Anja Hennemuth, Achim Seeger, Ola Friman, Stephan Miller, Bernhard Klumpp, Steffen Oeltze, and H-O Peitgen. A comprehensive approach to the analysis of contrast enhanced cardiac mr images. *Medical Imaging, IEEE Transactions on*, 27(11):1592–1610, 2008.

[23] Peng Gao, Raymond Yee, Lorne Gula, Andrew D Krahn, Allan Skanes, Peter Leong-Sit, George J Klein, John Stirrat, Nowell Fine, Luljeta Pallaveshi, et al. Prediction of arrhythmic events in ischemic and dilated cardiomyopathy patients referred for implantable cardiac defibrillator evaluation of multiple scar quantification measures for late gadolinium enhancement magnetic resonance imaging. *Circulation: Cardiovascular Imaging*, 5 (4):448–456, 2012.

Chapter 4

Fast Deformable Image Registration with Non-Smooth Dual Optimization

4.1 Introduction

Registration of medical images is a challenging task which attempts to spatially align two images and find the spatial correspondences between the anatomies in each dataset. It becomes fundamental to many applications in the field of neuroimaging, such as atlas-based image segmentation, quantifying spatial and longitudinal disease patterns and computer-assisted diagnostics. However, it is well-known that the linear image registration, which computes an optimal affine transformation of one brain image onto another, is often insufficient and fails to account for anatomical variability and other highly non-linear phenomena. This limitation encouraged the development of many deformable or non-rigid image registration methods over the past decade to address these challenges (see Sec. 4.1.2 for a short review).

Of particular note is the application of deformable image registration (DR) to determine

This Chapter is adapted from an article currently in revision. M. Rajchl, J.S.H. Baxter, W. Qiu, A.R. Khan, A. Fenster, T.M. Peters, and J. Yuan (2014). *Fast Deformable Image Registration with Non-Smooth Dual Optimization.* IEEE Transactions on Medical Imaging.

an accurate mapping of an annotated image to new patient data, essential to the atlas-based image segmentation approach widely-used in neuroimaging [1, 2, 3] and other medical imaging [4, 5, 6, 7, 8, 9, 10, 11, 12]. Such techniques makes full use of the expert manual segmentations on a small subset of the image data, avoiding the prohibitive time consumption required for delineating a large number of images manually.

Often, deformable registration is achieved through the use of mathematical optimization theory, where an optimizer is used to explicitly maximize a similarity metric, such as mutual information [13, 14] or cross-correlation [15, 16], or minimize a dissimilarity metric such as intensity differences, or a neighbourhood descriptor [17]. This approach, however, is a mathematically ill-posed problem and deformation fields can be constructed that achieve the optimal value of the objective function but do not represent an adequate or even a physically possible deformation. To address the issue of being ill-posed, a deformable smoothing mechanism could be added [18], constraints could be placed on the deformation field to prevent undesirable features (such as singularities) [16], or the objective function could be augmented with a regularization metric [19, 20, 21]. These regularization metrics address the ill-posed-ness problem by rewarding deformation fields for their smoothness, implicitly discouraging highly non-smooth features rather than placing explicit constraints against them. The benefit of the latter two is that they can be incorporated directly into the optimization problem being addressed.

Variational optical-flow based optimization approaches are a subset of deformable registration techniques, which have been developed as efficient non-rigid medical image registration methods with improved robustness and lower variability (see [22, 23] for references). Often, incremental coarse-to-fine frameworks [24, 25] are employed to capture substantial non-rigid deformations, represented at the coarsest levels, with sufficient smoothness without sacrificing the accuracy at the finest-resolved levels. In this respect, a partial differential equation (PDE) diffusion algorithm is often derived with a corresponding first-order gradient-descent solver, often resulting in slow convergence towards a local optimum.

Recently, direct convex optimization methods, specifically dual optimization, were successfully developed to efficiently solve a wide spectrum of problems in image processing [26, 27] and have been subject to increasing attention in medical image segmentation [28, 29, 30, 31, 32] and registration [19, 20, 21]. It provides both a sound foundation in mathematical optimization and an efficient numerical algorithm, with the capability of tackling non-smooth energy function terms. Given convex regularization functions, linearization of the image similarity measure at each scale results in a convex optimization problem that reflects the local geometry of the non-convex objective function. Also, with the availability of powerful and inexpensive graphics hardware and the inherent parallelism of the derived algorithms, these approaches can be easily implemented through modern GPGPU to achieve a significant improvement in computation time.

4.1.1 Contributions

In this work, we propose a new dual optimization-based approach to address non-rigid brain image registration efficiently and accurately based on our recent work [33]. This framework employs a standard coarse-to-fine optical-flow estimation framework, and can optimize the energy function based on any point-wise similarity or dissimilarity metric and either total variation or other convex regularization using a non-smooth Gauss-Newton (GN) approach. We introduce a novel dual optimization formulation from which we derive an efficient duality-based optimization algorithm. Unlike the previous approaches proposed in [19, 20], which target to optimize a similar convex energy function, our method optimizes the exact convexified objective function, rather than an approximate energy function with the additional artificial splitting term. This implies great advantages in higher optimality degree and numerical performance, such that the proposed method is more accurate, simple (with fewer parameters) and robust when presented with a low regularization parameter, and it has more uniform convergence in said cases without sacrificing optimality. Additionally, our method takes advantage of GPGPU computing to dramatically improve its computational efficiency. In particular, we

implement and study two convex deformation regularization functions upon the proposed dual optimization framework. Extensive comparisons against the four highest ranking methods as highlighted by Klein et al. [34], which allow direct and fair numerical comparisons, demonstrate that the proposed dual optimization based approach achieves both high accuracy and numerical efficiency.

4.1.2 Previous Studies

In this section, we summarize several previous methods employed to solve the deformable image registration problems. Recent surveys [23, 35, 36] present a good overview of the existing non-linear image registration methods. First, we present a more detailed summary of the similar TV-L_1 regularization method investigated by Pock et al.[19, 20] :

TV-L_1-Optical-Flow:

The *TV-L_1-Optical-Flow* method developed by Pock et al.[19, 20] is similar to our method in that it addresses total-variation based regularization. The specific objective function involves two coupled deformation fields $u(x)$ and $v(x)$ for an N-dimensional problem and is defined as:

$$\begin{aligned}\min_{u,v}\ & \lambda \int_\Omega |I_1(x+v) - I_2(x)|dx \\ & + \frac{1}{2\theta}\int_\Omega \sum_{d=1}^{N}(u(x)-v(x))^2 dx + \int_\Omega \sum_{d=1}^{N}|\nabla u(x)|dx\end{aligned} \tag{4.1}$$

in which $\lambda \geq 0$ weights the contribution of the dissimilarity against the regularization, and $\theta > 0$ is a small parameter of the term penalizing the difference between the two deformation fields u and v. This objective function is addressed through the splitting approach, that is, two simultaneous simpler problems are addressed:

$$\min_{v} \lambda \int_\Omega |I_1(x+v) - I_2(x)|dx + \frac{1}{2\theta}\int_\Omega \sum_{d=1}^{N}(u(x)-v(x))^2 dx \tag{4.2}$$

which considers the deformation field u to be fixed and

$$\min_{u} \frac{1}{2\theta} \int_{\Omega} \sum_{d=1}^{N} (u(x) - v(x))^2 dx + \int_{\Omega} \sum_{d=1}^{N} |\nabla u(x)| dx \tag{4.3}$$

which considers the deformation field v to be fixed. This is done in a coarse-to-fine framework using thresholding to address the first optimization problem and a Chambolle iteration [37] for the second. This method is similar in that it uses a duality-based approach to optimize for the total variation based regularization, but is developed with a novel optimization perspective, differing in terms of the objective function and optimization structure.

As a basis for comparison, we use the comparative study performed by Klein et al. [34] where 14 DR algorithms were compared across four open brain image databases. In this work, we use the highest four ranking DR methods identified in [34], as an example of the best in the state of the art:

Advanced Normalization Tools (ANTs):

The *Symmetric Normalization (SyN)* DR method proposed by Avants et al.[16] uses a multi-resolution scheme to enforce a bi-directional diffeomorphism while maximizing a cross-correlation metric. It has been shown in several open challenges [34, 38, 39] to outperform well established methods. *SyN* regularizes the deformation field through penalizing the squared magnitude of the underlying velocity field.

Image Registration Toolkit (IRTK):

The well-known *Fast Free-Form deformations (F3D)* method in [40] defines "a lattice of equally spaced control points" [34] over the target image and, by moving each point, locally modifies the deformation field. Normalized mutual information combined with a cubic b-spline bending energy is used as the objective function. It employs a multi-resolution approach that

uses progressively decreasing lattice spacing along with Gaussian smoothing.

Automatic Registration Toolbox (ART):

Ardekani et al.[18] present a homeomorphic DR method using normalized cross-correlation as similarity metric in a multi-resolution framework. The deformation field is regularized via median and low-pass Gaussian filtering at each iteration.

Statistical Parametric Mapping DARTEL Toolbox (SPM_D):

The *DARTEL* algorithm presented in [41] employs a static finite difference model of a velocity field. The flow field is considered to be a member of the Lie algebra, which is exponentiated to produce a deformation inherently enforcing a diffeomorphism [41]. It is implemented in a recursive, multi-resolution manner.

4.2 Methods

In this section, we propose a multi-scale dual optimization-based method to estimate the non-linear deformation field $u(x) = [u_1(x), u_2(x), u_3(x)]^{\mathrm{T}}$, between two given images $I_1(x)$ and $I_2(x)$, which minimizes a variational optical-flow energy function, i.e.

$$\min_{u} \quad P(I_1, I_2; u) \; + \; R(u) \tag{4.4}$$

where $P(I_1, I_2; u)$ represents a dissimilarity measure of the two input images $I_1(x)$ and $I_2(x)$ under deformation by u, and $R(u)$ is the regularization function to match a deformation field with the required smoothness. In this chapter, we employ the sum of absolute intensity differences (SAD):

$$\min_{u} \quad P(I_1, I_2; u) \; := \; \int_{\Omega} |I_1(x+u) - I_2(x)| \; dx \, , \tag{4.5}$$

as an effective and robust similarity measurement to the two input images from the same imaging modalities.

The proposed framework can also be directly adapted for more advanced image dissimilarity measures designed for image registration between different image modalities, where other metrics, such as mutual information (MI) [13, 14] or the non-local image similarity function [17] may be employed. Without additional constraints or regularization, any optimization problem using these metrics is ill-posed and can lead to trivial or erroneous deformations.

A regularization term $R(u)$ in (4.4) is often incorporated to make the minimization problem (4.4) well-posed, and solutions well-behaved. These regularization terms also encourage the deformation field to preserve the image's topology. We consider the L_p-norm convex function as the regularization term in this work, such that:

$$R(u) := \alpha \sum_{i=1}^{3} \int_{\Omega} |\nabla u_i|^p \, dx \tag{4.6}$$

where $p \geq 1$. Clearly, $p = 1$ gives rise to a non-smooth function, specifically the sum of three convex total-variation functions: $R(u) = \alpha \int_{\Omega} (|\nabla u_1| + |\nabla u_2| + |\nabla u_3|) dx$. In this chapter, we focus on two well-known regularization functions, $R(u)$ in (4.6) where $p = 1$ or 2, the former we will denote as total-variation regularization (TVR) and the latter as quadratic regularization (QR).

Because of the expected non-linearity and non-convexity of the image functions $I_1(x)$ and $I_2(x)$ because of noise and the presence of structure, it is challenging to directly optimize the energy function (4.4), even if its regularization term $R(u)$ is convex. To address this issue, we introduce an incremental linearization and convexification approach to solving the studied optimization problem (4.4), which lends itself to a standard coarse-to-fine optimization framework. This approach allows for a global-optimization perspective, properly avoiding local optima through the ability to capture large deformations.

In Section 4.2.1, we develop the coarse-to-fine optimization framework, composed of a sequence of related minimization problems. Each of these problems is solved through a new

non-smooth GN approach, introduced in Sections 4.2.2 and 4.2.3, which employs a novel sequential convexification and dual optimization procedure.

4.2.1 Coarse-to-Fine Optimization Framework

The first stage in our multi-scale approach, is the construction of the coarse-to-fine image pyramid for each image function. Let $I_1^1(x) \dots I_1^L(x)$ be the L-level pyramid representation of the image $I_1(x)$ from the coarsest resolution $I_1^1(x)$ to the finest resolution $I_1^L(x) = I_1(x)$, and $I_2^1(x) \dots I_2^L(x)$ the L-level coarse-to-fine pyramid representation of the image $I_2(x)$. Indeed, at the finest image resolution $\ell = L$, we have $I_1^L(x) = I_1(x)$ and $I_2^L(x) = I_2(x)$, i.e. the original images.

The optimization process begins at the coarsest resolution level, i.e. $\ell = 1$, which extracts the deformation field $u^1(x)$ between the two images of $I_1^1(x)$ and $I_2^1(x)$ such that

$$\min_{u^1} \quad P(I_1^1(x), I_2^1(x); u^1) + R(u^1)\,. \tag{4.7}$$

In fact, the resulting vector field $u^1(x)$ gives the optimum deformation field at the coarsest scale. It is interpolated to the next finer image resolution $\ell = 2$ so as to compute the optimum finer-level deformation field $u^2(x)$; the same process is repeated to obtain the optimum deformation field $u^3(x) \dots u^L(x)$ at each image resolution level, sequentially from the coarsest level to the finest.

Second, at each resolution level ℓ, $\ell = 2 \dots L$, we compute an incremental deformation field $t^\ell(x)$ based on the two image functions $I_2^\ell(x)$ and $I_1^\ell(x + u^{\ell-1})$, where $I_1^\ell(x + u^{\ell-1})$ is warped by the deformation field $u^{\ell-1}(x)$ computed at the previous resolution level $\ell - 1$, i.e.

$$\min_{t^\ell} \quad P(I_1^\ell(x + u^{\ell-1}), I_2^\ell(x); t^\ell) + R(u^{\ell-1} + t^\ell)\,. \tag{4.8}$$

Clearly, the optimization problem (4.7) can be viewed as the special case of (4.8), i.e. for $\ell = 1$, we define $u^0(x) = 0$ and $u^1(x) = (u^0 + t^1)(x)$. Therefore, the proposed coarse-to-

fine optimization framework sequentially explores the minimization of (4.8) at each image resolution level, from the coarsest $\ell = 1$ to the finest $\ell = L$.

4.2.2 Sequential Convexification and Dual Optimization

Now we consider the optimization problem (4.8) at a single image resolution level. Given the highly non-linear function $P(I_1^\ell(x+u^{\ell-1}), I_2^\ell(x); t^\ell)$ in (4.8), we introduce a sequential linearization and convexification procedure for this challenging non-linear optimization problem. This procedure results in a series of incremental warping steps in which each step approximates an update of the deformation field $t^\ell(x) = [t_1^\ell(x), t_2^\ell(x), t_3^\ell(x)]^{\mathrm{T}}$, until the updated deformation is sufficiently small, i.e., it iterates through the following sequence of convex minimization steps until convergence is attained:

- Initialize $(h^\ell)^0(x) = 0$ and let $k = 1$;
- At the k^{th} iteration, define the deformation field as

$$\tilde{u}^{\ell-1}(x) := \Big(u^{\ell-1} + \sum_{i=0}^{k-1} (h^\ell)^i\Big)(x)$$

  and compute the update deformation $(h^\ell)^k$ to $\tilde{u}^{\ell-1}(x)$ by minimizing the following convex energy function:

$$\min_{(h^\ell)^k} \int_\Omega \left|\tilde{P}_0^k + \nabla \tilde{P}^k \cdot (h^\ell)^k\right| dx \; + \; R(u^{\ell-1} + (h^\ell)^k)\,, \tag{4.9}$$

  where

$$\tilde{P}^k((h^\ell)^k) \;=\; P(I_1^\ell(x + \tilde{u}^{\ell-1}), I_2^\ell(x); (h^\ell)^k)$$

  and $\tilde{P}_0^k(x) = P(I_1^\ell(x + \tilde{u}^{\ell-1}), I_2^\ell(x); 0)$.

- Let $k = k + 1$ and repeat the second step until the new update $(h^\ell)^k$ is sufficiently small. Then, we have the total incremental deformation field $t^\ell(x)$ at the image resolution level

ℓ as:

$$t^{\ell}(x) \;=\; \sum_{i=0}^{k} (h^{\ell})^{i}(x)\,.$$

These steps can be viewed as a non-smooth GN method for the non-linear optimization problem (4.8), in contrast to the classical GN method proposed in [42]. Moreover, the L_1-norm and the convex regularization term $\mathcal{R}(\cdot)$ in (4.9) results in a convex optimization problem. The non-smooth L_1-norm from (4.9) provides more robustness in practice than the conventional smooth L_2-norm.

Here, we study the convex minimization problem (4.9), the most essential optimization step in the proposed algorithmic framework, using a novel primal-dual optimization strategy: This variational analysis not only provides an equivalent dual formulation to the proposed optimization problem (4.9) but also results in an efficient duality-based optimization algorithm.

We simplify the expression of the convex optimization problem (4.9) as follows:

$$\min_{h} \int_{\Omega} |P_0 + \nabla P \cdot h|\, dx \;+\; R(\tilde{u} + h)\,, \tag{4.10}$$

where $\tilde{u}(x)$ stands for a given deformation function.

Through variational analysis, we can derive a mathematically equivalent *dual model* to the convex minimization problem (4.10):

Proposition 4.2.1 *The* convex minimization problem (4.10) *can be represented by its* primal-dual model (B.7) *and* dual model*:*

$$\max_{|w(x)|\leq 1, q} E(w,q) := \int (wP_0 + \sum_{i=1}^{3} \tilde{u}_i \operatorname{div} q_i) dx \;-\; R_p^*(q) \tag{4.11}$$

subject to

$$F_i(x) := (w \cdot \partial_i P + \operatorname{div} q_i)(x) = 0\,, \quad i = 1,2,3\,. \tag{4.12}$$

For $p = 1, 2$, the dual regularization function $R_p^*(q)$ is given by (B.4)-(B.5)*.*

The proof is given in Appendix B.

4.2.3 Duality-Based Optimization Algorithm

As shown in Appendix B, each component of the deformation field $[h_1(x), h_2(x), h_3(x)]^{\mathrm{T}}$ operates as the optimal multiplier functions for their respective constraints, (4.12). Therefore, the energy function of the primal-dual model (B.7) is exactly the Lagrangian function to the *dual model* (4.11):

$$L(h, w, q) = E(w, q) + \sum_{i=1}^{3} \langle h_i, F_i \rangle ,$$

where $E(w, q)$ and the linear functions $F_i(x)$, $i = 1, 2, 3$, are defined in (4.11) and (4.12) respectively. We can now derive an efficient duality-based Lagrangian augmented algorithm based on the modern convex optimization theories (see [43, 26, 27] for details), using the augmented Lagrangian function:

$$L_c(h, w, q) = L(h, w, q) - \frac{c}{2} \sum_{i=1}^{3} \|F_i\|^2 , \tag{4.13}$$

where $c > 0$ is a positive constant and the additional quadratic penalty function is applied to ensure the functions (4.12) vanish. Our proposed *duality-based optimization algorithm* is:

- Set the initial values of w^0, q^0 and h^0, and let $k = 0$.
- Fix q^k and h^k, optimize w^{k+1} by

$$w^{k+1} := \arg \max_{|w(x)| \le 1} L_c(h^k, w, q^k) \tag{4.14}$$

generating the convex minimization problem:

$$\min_{|w(x)| \le 1} \int w P_0 dx + \frac{c}{2} \sum_{i=1}^{3} \int (w \partial_i P - T_i^k)^2 dx ; \tag{4.15}$$

where $T_i^k(x)$ $(i = 1, 2, 3)$ is computed from the fixed variables q^k and h^k. w^{k+1} can be computed by thresholding:

$$w^{k+1} = \text{Threshhold}_{|w(x)|\leq 1}(w^{k+1/2}(x)), \tag{4.16}$$

where

$$w^{k+1/2} = \frac{c\sum_{i=1}^{3}(\partial_i P \cdot T_i^k) - P_0}{c\sum_{i=1}^{3}(\partial_i P)^2}.$$

- Fixing w^{k+1} and h^k, optimize q^{k+1} by

$$q^{k+1} := \arg\min_{q} L_c(h^k, w^{k+1}, q); \tag{4.17}$$

which amounts to three convex minimization problems:

$$\min_{q_i} \int q_i \cdot \nabla \tilde{u}_i dx + \frac{c}{2}\int (\text{div}\, q_i - U_i^k)^2 dx + R_p^*(q);$$
$$i = 1, 2, 3; \tag{4.18}$$

where U_i^k is computed from the fixed variables w^{k+1} and h^k. Hence, q_i^{k+1}, $i = 1, 2, 3$, can be approximated by a gradient-descent or gradient-projection step, depending on which formulation $R_p^*(q)$ of (B.4) and (B.5) is applied.

- Once w^{k+1} and q^{k+1} are obtained, update h^{k+1} by

$$h_i^{k+1} = h^k - c\left(w^{k+1} \cdot \partial_i P + \text{div}\, q_i^{k+1}\right);$$
$$i = 1, 2, 3; \tag{4.19}$$

- Increment k and iterate until converged, i.e.

$$c\int \left|w^{k+1} \cdot \partial_i P + \text{div}\, q_i^{k+1}\right| dx \leq \delta, \tag{4.20}$$

where δ is a chosen small positive parameter (5×10^{-4}).

4.3 Experiments

4.3.1 Image databases

The image data consisted of an open multi-center T1-weighted (T1w) MRI dataset with corresponding manual segmentations of 80 labelled image volumes. All data used in [34] were made available on *www.mindboggle.info* [44] in a pre-processed form with labeling protocols and transforms into MNI space or pairwise affine registrations (for LPBA40). Table 4.1 gives an overview of the image acquisition parameters and image information.

Dataset	Subjects	Ages	TR	TE (ms)	FA	FS	N_{Labels}
LPBA40 [45]	40 (20 ♂, 20 ♀)	4.2-4.5	20	1.5T	56		
IBSR18 [46]	18 (14 ♂, 4 ♀)	7-71	n/a	n/a	n/a	1.5T	84
CUMC12 [47]	12 (6 ♂, 6 ♀)	34	5	45	1.5T	128	
MGH10	10 (4 ♂, 6 ♀)	22-29	6.6	2.9	8	3.0T	74

Table 4.1: Overview of image acquisition and population parameters.

4.3.2 Initialization & Pre-processing

Prior to registration, all T1w images in the IBSR18, MGH10, and CUMC12 databases were skull stripped by constructing brain masks from manual labels using morphological operations [34]. The images in the LPBA40 database were already pre-processed in a similar manner as described in [45]. Prior to DR, the images were mapped to the *MNI152_T1_1mm_brain* (for IBSR18, MGH10, CUMC12) and MNI_305 space (for LPBA40), respectively using the *FMRIB Software Library's (FSL) FLIRT* package [48]. These affine transformations were available and used to initialize the DR algorithms. This guarantees that the same initialization is used for the algorithms in [34] and our proposed methods, allowing for quantitative comparisons. As a pre-processing step, both source and target images were robustly normalized to

zero mean and standard deviation units to ensure regularization weight α constancy across the different databases.

4.3.3 Implementation & Parameter Tuning

Both proposed DR methods were implemented using MATLAB (Natick, MA) and the CUDA (NVIDIA, Santa Clara, CA) GPGPU computing architecture. The GN optimization scheme was implemented in a hierarchical manner involving a series of 'levels.' Each level corresponds to a degree of undersampling, each subsequent level increasing in resolution by a factor of two until the original image resolution is reached. Each level additionally consists of multiple warps invoking the proposed GPGPU accelerated regularization algorithm. Parameter tuning of the regularization weight α was performed on two randomly picked dataset pairs from each database, similar to the tuning in [34]. All other parameters, such as the number of levels (N_{Levels}), the number of warps (N_{Warps}) and the maximum number of iterations (It_{MAX}) were determined heuristically on a single image volume not used in this study. Table 4.2 contains all set parameter values, which were fixed for all experiments.

Method	α	N_{Levels}	N_{Warps}	It_{MAX}
GN QR	0.05	3	4	220
GN TVR	0.30	3	4	220
All parameters were kept constant across all experiments.				

Table 4.2: Registration parameters for the proposed methods

4.3.4 Validation Metrics

To facilitate direct comparison with other DR registration algorithms, we evaluated the resulting deformation fields using the same metrics as in [34]. These metrics evaluate the accuracy of the correspondence between the source image, F, to the target image, R, with respect to a labelled region, L, as indicated in [34]. Obtained deformations fields are used to warp the atlas label of F into the space of R to be numerically compared by several metrics:

- The *target overlap* (*TO*) as a regional metric:

$$TO = \frac{\sum_L |F_L \cap R_L|}{\sum_L |R_L|}, \tag{4.21}$$

- The *volume similarity* (*VS*) as a volume metric:

$$VS = 2\frac{\sum_L |F_L| - |R_L|}{\sum_L |F_L| + |R_L|}, \tag{4.22}$$

- The *mean absolute distance* (*MAD*) between the floating image boundary point $F_L B_p$ and the closest reference image boundary point $R_L B_{p'}$ as a distance metric:

$$MAD_L = \frac{1}{P}\sum_{p=1}^{P} \min_{p'} |F_L B_p - R_L B_{p'}|, \tag{4.23}$$

For all accuracy metrics on all four databases, results were considered significant if the probability of making a type I error was less than 5% ($p < 0.05$). For this purpose, we employed a series of two-tailed, pairwise Student's t-test, under the Bonferroni correction to address for multiple hypotheses. Both proposed methods were tested against each other and the best performing comparative method in order to determine significances in means.

4.4 Results

4.4.1 Run times

All experiments were conducted on a Ubuntu 12.04 (64-bit) desktop machine with 144 GB memory and an NVIDIA Tesla C2060 (512 cores, 6 GB memory) graphics card. The maximum run times for the MATLAB code including pre-processing and GN optimization, and GPGPU enhanced regularization at different resolution levels, are stated in Table 4.3. Considering total run times, the GN TVR runs for ~30 seconds longer, mainly due to the increased computational

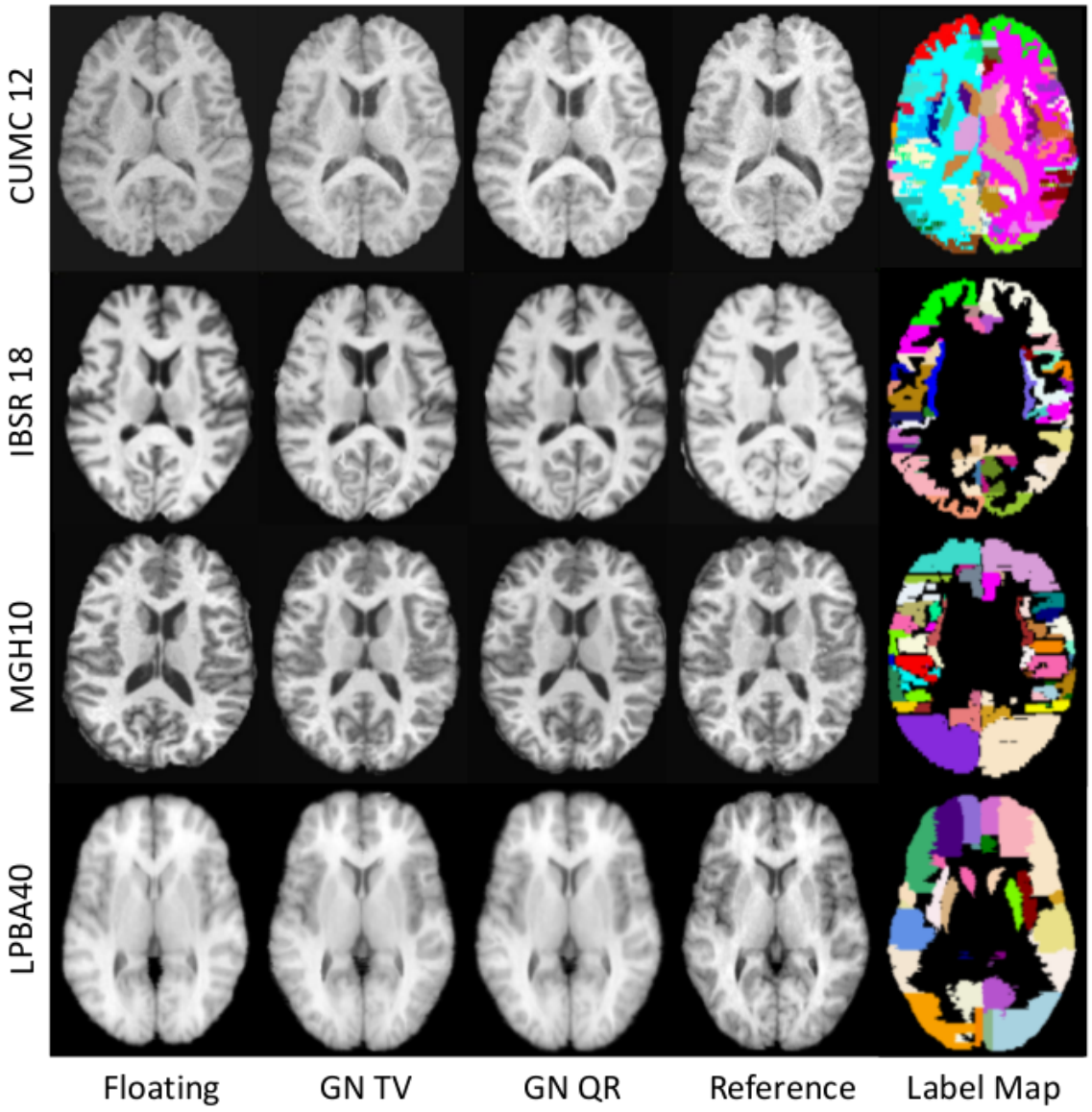

Figure 4.1: Exemplary registration results for both proposed methods on all four databases. Columns (from left to right): Floating image, registration with GN TV, registration with GN QR, reference image, label map of the reference image, . Rows (from top to bottom): Image pairs from the CUMC12, IBSR18, MGH10 and LPBA40 databases.

complexity of the method.

	GPU reg. [s]			GN opt. [s]	Total time [s]
DSF	4x	2x	1x		
GN QR	0.26	1.82	13.59	9.08	71.40
GN TVR	0.37	2.70	20.66	10.62	104.70

Table 4.3: Partial and total maximum run times for GN optimization and regularization using the proposed methods. The partial maximum run times are stated for GPGPU-based optimization on resolution levels with different downsampling factors (DSF).

4.4.2 Accuracy

Figure 4.2 shows boxplots of the TO accuracy for each of the four databases using the four best ranked methods according to Klein et al.[34] and the two proposed methods. Table 4.4 lists all numerical results of the TO, where numerical results for VS and MAD can be found in Table 4.5 and Table 4.6 respectively. The results were averaged across all regions in each label set (LPBA40, IBSR18, CUMC12, and MGH10) then across brain pairs as obtained from the scripts available in [44]. All T-tests were statistically significant ($p < 0.05$, under Bonferroni correction), unless noted with (*).

Target Overlap

The proposed GN TVR method significantly outperformed all comparative methods in terms of mean TO in 3 out of 4 databases (IBSR18, CUMC12, MGH10), yielding at least 10% higher TO than the methods presented in [34]. However, on the LPBA40 database, *ART* outperformed both proposed methods significantly. In comparison, the GN method using TVR yielded significantly higher TO than with QR, except on LPBA40.

Volume Similarity

In terms of VS, the GN QR method outperformed both the GN TVR and comparative methods on 2 of 4 databases significantly (IBSR18, CUMC12). Improvements over *ART* were not significant on LPBA40 and also not significant compared to TVR on MGH10.

Distance Error

All DEs for proposed GN methods were computed with the scripts provided online on [44], however were only stated for LPBA40 for all comparative methods, since only those results were provided. On LPBA40, *SPM_D* yielded significantly lower DE by an average of 0.25 mm than both proposed methods. On all other databases (IBSR18, CUM12, MGH10), the GN TVR method outperformed the QR-based method significantly.

	LPBA40	**IBSR18**	**CUMC12**	**MGH10**
FLIRT	59.3 ± 11.9	39.7 ± 13.0	39.6 ± 11.5	46.2 ± 14.0
SPM_D	67.2 ± 18.4	54.0 ± 14.7	52.0 ± 13.9	54.3 ± 16.1
IRTK	70.0 ± 10.3	52.1 ± 15.0	51.8 ± 12.5	54.9 ± 15.7
ART	**71.9 ± 9.6**	51.5 ± 14.1	50.5 ± 12.2	56.1 ± 15.3
Syn	71.4 ± 10.9	52.8 ± 14.9	51.6 ± 12.6	56.8 ± 15.8
GN QR	71.1 ± 9.4	60.8 ± 11.8	60.3 ± 10.4	65.2 ± 10.2
GN TVR	69.5 ± 10.0	**64.9 ± 12.5**	**64.7 ± 10.5**	**69.2 ± 9.4**

All results were statistically significant ($p < 0.05$, see Sec.4.4.2).
The highest mean TO for each database is shown in bold.

Table 4.4: Mean target overlap (TO) accuracy

4.5 Discussion

We proposed two novel GPGPU-accelerated regularization methods on deformation fields in deformable registration. These methods were implemented within a multi-resolution GN optimization framework and compared on four publicly available databases. We employed the

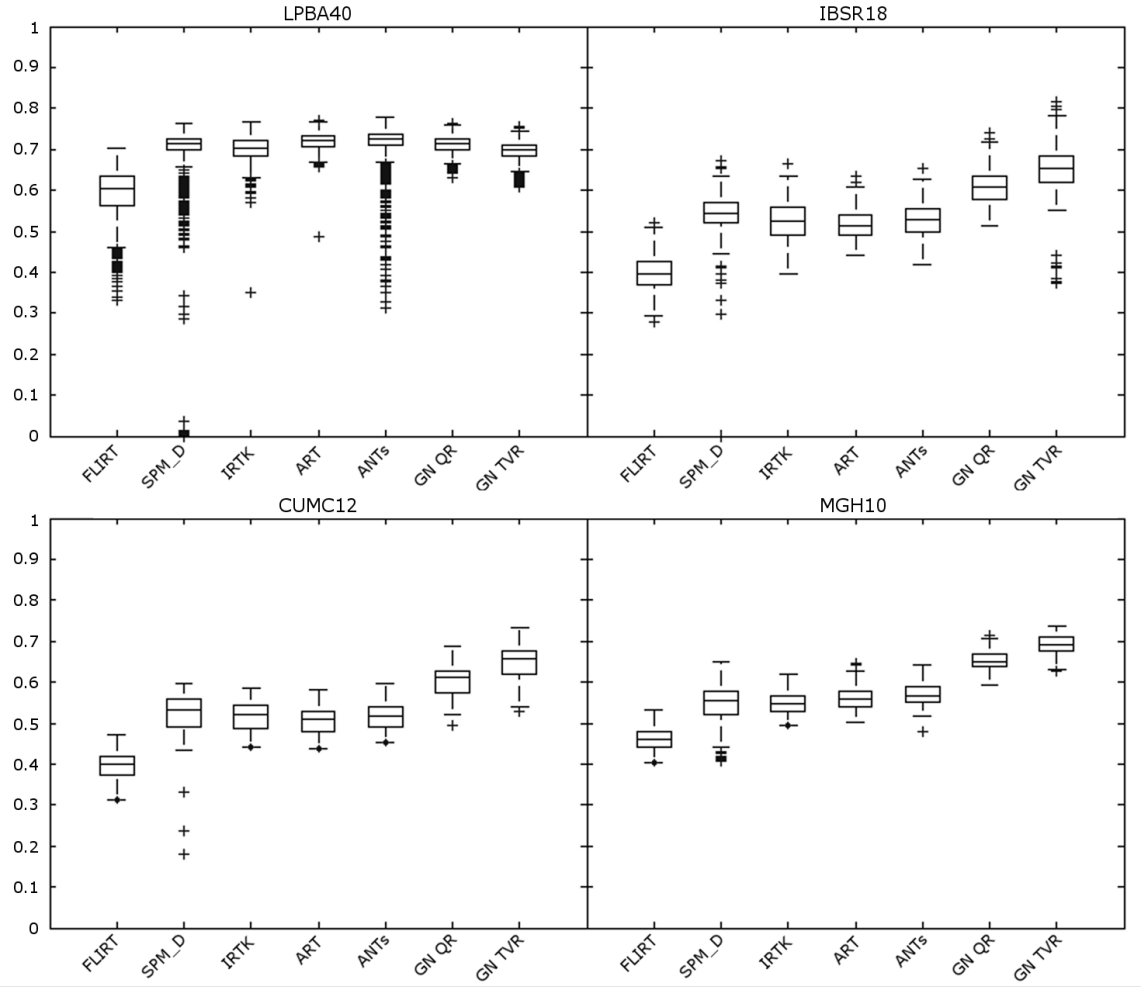

Figure 4.2: Mean Target Overlap (TO) Results Across All Image Databases

	LPBA40	IBSR18	CUMC12	MGH10
FLIRT	89.7 ± 7.6	82.2 ± 12.6	83.0 ± 11.9	81.3 ± 12.6
SPM5-D	87.1 ± 20.3	83.3 ± 12.3	83.3 ± 14.4	80.9 ± 13.3
IRTK	91.1 ± 6.7	82.4 ± 12.6	83.8 ± 11.7	81.4 ± 13.1
ART	91.4 ± 6.6*	83.0 ± 12.3	83.8 ± 11.7	82.0 ± 12.6
Syn	91.4 ± 6.7	83.1 ± 12.2	83.7 ± 11.7	81.7 ± 12.7
GN QR	**91.5 ± 6.5***	**94.4 ± 4.3**	**94.7 ± 4.0**	**94.8 ± 3.8***
GN TVR	91.0 ± 6.8	93.3 ± 5.9	94.7 ± 4.1	94.7 ± 3.9*

All results were statistically significant ($p < 0.05$), except for *., see Sec.4.4.2
The highest mean VS for each database is shown in bold.

Table 4.5: Mean volume similarity (VS) accuracy

	LPBA40	IBSR18	CUMC12	MGH10
FLIRT	3.80 ± 1.19			
SPM5-D	**2.84 ± 1.44**			
IRTK	3.03 ± 1.00			
ART	2.92 ± 0.93			
Syn	2.89 ± 1.01			
GN QR	2.94 ± 0.93	1.74 ± 0.25	1.24 ± 0.39	2.13 ± 0.62
GN TVR	3.09 ± 0.98	**1.56 ± 0.23**	**1.11 ± 0.38**	**1.98 ± 0.57**

All results were statistically significant ($p < 0.05$, see Sec.4.4.2).
The lowest mean MAD for each database is shown in bold.

Table 4.6: Mean mean absolute distance (MAD) accuracy

same initialization, tuning conditions, and evaluation scripts to quantitatively compare the proposed methods against 14 well-known DR methods, and we numerically state the accuracy metrics for the four highest ranked methods for direct comparison.

4.5.1 Run times

Due to the inherent parallelism of both QR and TVR regularizers, comparably short run times were observed for both proposed methods. The overall lower run time of the QR regularization (see Table 4.3) can be explained by the lower complexity of the QR solver. The maximum run time of 104 seconds of the GN TVR method is very low compared to those reported for the comparative methods by Klein et al. [34], where the mean run times reported ranged from ~17

(*SPM_D*) to ~120 (*IRTK*) minutes.

We want to emphasize the potential impact of graphics hardware on the total run time of the proposed methods: TV regularization required ~90% of the total run time of the method on a relatively old Tesla C2060 GPU (release date 2010). Because of this, the run times of both methods can be expected to improve considerably by employing more recent hardware, which could help overcome the computational limitations associated with approaches relying heavily on DR, such as multi-atlas-based segmentation.

Lastly, we note that the similarity metric we used has a low computational cost, but the total run time might increase when implementing more advanced similarity metrics such as mutual information, cross-correlation, or non-local approaches [17]. However, there have also been attempts to implement such algorithms using GPGPU [49, 50, 51] to mitigate the increase in computational burden.

4.5.2 Accuracy

Both proposed methods yielded higher accuracy on three of the four databases in all metrics, where the GN TVR version scored higher in TO and MAD and slightly lower in terms of VS on IBSR18, CUMC12 and LPBA40 (VS results on MGH10 were not statistically significant). The proposed GN TVR method demonstrated impressive performance yielding improved TO accuracy of >5% over QR and >10% against the comparative methods on the IBSR18, CUMC12 and MGH10 databases.

We note the qualitatively lower number of outliers in TO for both proposed methods (see Figure 4.2). Especially on LPBA40, where the affine initialization (FLIRT) had several outliers yielding low TO, both methods were able to correct for this, demonstrating good robustness with respect to initialization.

All accuracy metrics on LPBA40 for all DR methods were similar in their means, however differences statistically significant ($p < 0.05$). This might be due to the choice of labeling protocol (see Figure 4.1) for this particular database being very liberal in its classification of

cortical gray matter. This labeling protocol demarcates no distinct gray matter/white matter boundaries and this might reduce its capacity to measure accuracy of DR techniques.

Recently, the S-HAMMER [52] method has been developed and validated across the same sequence of image databases outperforming the same 14 methods explored by Klein et al [34]. The authors in [52] state means and standard deviations of resulting TO of S-HAMMER, however, no other metrics evaluated in Klein et al. [34] were reported. Since the individual results obtained by the S-HAMMER method were not released, statistical testing was not possible. Both of our proposed methods outperform S-HAMMER across three of the four databases (IBSR18, CUMC12, and MGH10) by >5% TO. Wu et al [52] reported a TO of 72.48 ± 8.46% for LPBA40 - higher than the best performing method (ART) in this study.

We note that both proposed methods employ the simplest and non-robust similarity metric, SAD, while *SPM_D*, *IRTK*, *ART* and *SyN* use advanced metrics (see [34]). The choice of similarity metric was intentionally chosen for these experiments to demonstrate the potential of the proposed methods without more sophisticated similarity metrics or an advanced optimizer (i.e. a Levenberg-Marquardt optimizer as that used in *SPM_D* [41]).

4.5.3 Future directions

The current *RANCOR* framework can be seen as a basic method to be extended over time, under the same open science credo, that allowed us to readily and quantitatively compare well-known open methods using public databases. As the current framework cannot mathematically guarantee that the resulting deformations will be diffeomorphic, the next step is to enforce such a constraint. Furthermore, to enable inter-modality DR, we will implement and test commonly used advanced similarity metrics, such as normalized mutual-information, normalized cross-correlation, or more recently developed methods, such as the $L2-norm$ of the MIND descriptor [17]. Since command-line tools, such as the open DR methods are required for large-scale data analysis, *RANCOR* and its source code is openly available to the community (*http://sourceforge.net/projects/rancor/*).

4.6 Conclusions

We proposed two GPGPU-accelerated regularization mechanisms implemented within a GN optimization framework and evaluated them against the four highest ranking non-linear registration algorithms according to [34]. Further, we demonstrated its high accuracy in performing pairwise registrations on four open databases both visually and numerically, and provide the implementation back to the community in an open manner.

Bibliography

[1] Paul Aljabar, Rolf A Heckemann, Alexander Hammers, Joseph V Hajnal, and Daniel Rueckert. Multi-atlas based segmentation of brain images: atlas selection and its effect on accuracy. *Neuroimage*, 46(3):726–738, 2009.

[2] Owen T Carmichael, Howard A Aizenstein, Simon W Davis, James T Becker, Paul M Thompson, Carolyn Cidis Meltzer, and Yanxi Liu. Atlas-based hippocampus segmentation in alzheimer's disease and mild cognitive impairment. *Neuroimage*, 27(4):979–990, 2005.

[3] Xabier Artaechevarria, Arrate Munoz-Barrutia, and Carlos Ortiz-de Solorzano. Combination strategies in multi-atlas image segmentation: Application to brain MR data. *Medical Imaging, IEEE Transactions on*, 28(8):1266–1277, 2009.

[4] Ivana Isgum, Marius Staring, Annemarieke Rutten, Mathias Prokop, Max A Viergever, and Bram van Ginneken. Multi-atlas-based segmentation with local decision fusionapplication to cardiac and aortic segmentation in CT scans. *Medical Imaging, IEEE Transactions on*, 28(7):1000–1010, 2009.

[5] Michal Depa, Mert R Sabuncu, Godtfred Holmvang, Reza Nezafat, Ehud J Schmidt, and Polina Golland. Robust atlas-based segmentation of highly variable anatomy: Left atrium

segmentation. In *Statistical Atlases and Computational Models of the Heart*, pages 85–94. Springer, 2010.

[6] Robin Wolz, Chengwen Chu, Kazunari Misawa, Kensaku Mori, and Daniel Rueckert. Multi-organ abdominal CT segmentation using hierarchically weighted subject-specific atlases. In *Medical Image Computing and Computer-Assisted Intervention–MICCAI 2012*, pages 10–17. Springer, 2012.

[7] Yongxin Zhou and Jing Bai. Multiple abdominal organ segmentation: an atlas-based fuzzy connectedness approach. *Information Technology in Biomedicine, IEEE Transactions on*, 11(3):348–352, 2007.

[8] Xiao Han, Mischa S Hoogeman, Peter C Levendag, Lyndon S Hibbard, David N Teguh, Peter Voet, Andrew C Cowen, and Theresa K Wolf. Atlas-based auto-segmentation of head and neck CT images. In *Medical Image Computing and Computer-Assisted Intervention–MICCAI 2008*, pages 434–441. Springer, 2008.

[9] Sofia K Michopoulou, Lena Costaridou, Elias Panagiotopoulos, Robert Speller, George Panayiotakis, and Andrew Todd-Pokropek. Atlas-based segmentation of degenerated lumbar intervertebral discs from MR images of the spine. *Biomedical Engineering, IEEE Transactions on*, 56(9):2225–2231, 2009.

[10] Stefan Klein, Uulke A van der Heide, Irene M Lips, Marco van Vulpen, Marius Staring, and Josien PW Pluim. Automatic segmentation of the prostate in 3D MR images by atlas matching using localized mutual information. *Medical physics*, 35(4):1407–1417, 2008.

[11] Sébastien Martin, Jocelyne Troccaz, and Vincent Daanen. Automated segmentation of the prostate in 3D MR images using a probabilistic atlas and a spatially constrained deformable model. *Medical physics*, 37(4):1579–1590, 2010.

[12] Mariano Cabezas, Arnau Oliver, Xavier Lladó, Jordi Freixenet, and Meritxell

Bach Cuadra. A review of atlas-based segmentation for magnetic resonance brain images. *Computer methods and programs in biomedicine*, 104(3):e158–e177, 2011.

[13] William M Wells III, Paul Viola, Hideki Atsumi, Shin Nakajima, and Ron Kikinis. Multi-modal volume registration by maximization of mutual information. *Medical image analysis*, 1(1):35–51, 1996.

[14] Peter Rogelj, Stanislav Kovačič, and James C Gee. Point similarity measures for non-rigid registration of multi-modal data. *Computer vision and image understanding*, 92(1): 112–140, 2003.

[15] Adrian Andronache, Martin von Siebenthal, Gábor Székely, and Ph Cattin. Non-rigid registration of multi-modal images using both mutual information and cross-correlation. *Medical image analysis*, 12(1):3–15, 2008.

[16] Brian B Avants, Charles L Epstein, Murray Grossman, and James C Gee. Symmetric diffeomorphic image registration with cross-correlation: evaluating automated labeling of elderly and neurodegenerative brain. *Medical image analysis*, 12(1):26–41, 2008.

[17] Mattias P Heinrich, Mark Jenkinson, Manav Bhushan, Tahreema Matin, Fergus V Gleeson, Sir Michael Brady, and Julia A Schnabel. Mind: Modality independent neighbourhood descriptor for multi-modal deformable registration. *Medical Image Analysis*, 16(7): 1423–1435, 2012.

[18] Babak A Ardekani, Stephen Guckemus, Alvin Bachman, Matthew J Hoptman, Michelle Wojtaszek, and Jay Nierenberg. Quantitative comparison of algorithms for inter-subject registration of 3d volumetric brain mri scans. *Journal of neuroscience methods*, 142(1): 67–76, 2005.

[19] Thomas Pock, Martin Urschler, Christopher Zach, Reinhard Beichel, and Horst Bischof. A duality based algorithm for tv-l 1-optical-flow image registration. In *Medical Im-*

age Computing and Computer-Assisted Intervention–MICCAI 2007, pages 511–518. Springer, 2007.

[20] Christopher Zach, Thomas Pock, and Horst Bischof. A duality based approach for real-time tv-l 1 optical flow. In *Pattern Recognition*, pages 214–223. Springer, 2007.

[21] Yue Sun, Jing Yuan, Martin Rajchl, Wu Qiu, Cesare Romagnoli, and Aaron Fenster. Efficient convex optimization approach to 3d non-rigid mr-trus registration. In *Medical Image Computing and Computer-Assisted Intervention–MICCAI 2013*, pages 195–202. Springer, 2013.

[22] Jan Modersitzki. *Numerical Methods for Image Registration*. Numerical Mathematics and Scientific Computation. Oxford University Press, 2004. ISBN 0-19-852841-8.

[23] Aristeidis Sotiras, Christos Davatzikos, and Nikos Paragios. Deformable medical image registration: A survey. *IEEE Trans. Med. Imaging*, 32(7):1153–1190, 2013.

[24] Pierre Hellier, Christian Barillot, Étienne Mémin, and P. Perex. Hierarchical estimation of a dense deformation field for 3D robust registration. *IEEE Trans. Med. Imaging*, 20 (5):388–402, 2001.

[25] Jing Yuan, Christoph Schnörr, and Étienne Mémin. Discrete orthogonal decomposition and variational fluid flow estimation. *Journal of Mathematical Imaging and Vision*, 28 (1):67–80, 2007.

[26] Jing Yuan, Egil Bae, and Xue-Cheng Tai. A study on continuous max-flow and min-cut approaches. In *Computer Vision and Pattern Recognition (CVPR), 2010 IEEE Conference on*, pages 2217–2224. IEEE, 2010.

[27] Jing Yuan, Egil Bae, Xue-Cheng Tai, and Yuri Boykov. A continuous max-flow approach to potts model. In *Computer Vision–ECCV 2010*, pages 379–392. Springer, 2010.

[28] E. Ukwatta, Jing Yuan, M. Rajchl, Wu Qiu, D. Tessier, and A. Fenster. 3-d carotid multi-region mri segmentation by globally optimal evolution of coupled surfaces. *Medical Imaging, IEEE Transactions on*, 32(4):770–785, April 2013.

[29] M Rajchl, J Yuan, E Ukwatta, and TM Peters. Fast interactive multi-region cardiac segmentation with linearly ordered labels. In *Biomedical Imaging (ISBI), 2012 9th IEEE International Symposium on*, pages Page–s. IEEE Conference Publications, 2012.

[30] Jing Yuan, Wu Qiu, Eranga Ukwatta, Martin Rajchl, Yue Sun, and Aaron Fenster. An efficient convex optimization approach to 3d prostate mri segmentation with generic star shape prior. *Prostate MR Image Segmentation Challenge, MICCAI*, 2012.

[31] Wu Qiu, Jing Yuan, Eranga Ukwatta, Yue Sun, Martin Rajchl, and Aaron Fenster. Fast globally optimal segmentation of 3D prostate mri with axial symmetry prior. In *Medical Image Computing and Computer-Assisted Intervention–MICCAI 2013*, pages 198–205. Springer Berlin Heidelberg, 2013.

[32] M. Rajchl, J. Yuan, J. White, E. Ukwatta, J. Stirrat, C. Nambakhsh, F. Li, and T. Peters. Interactive hierarchical max-flow segmentation of scar tissue from late-enhancement cardiac MR images. *IEEE Transactions on Medical Imaging*, 33(1):159–172, 2014.

[33] Martin Rajchl, John SH Baxter, Wu Qiu, Ali R Khan, Aaron Fenster, Terry M Peters, and Jing Yuan. Rancor: Non-linear image registration with total variation regularization. *arXiv preprint arXiv:1404.2571*, 2014.

[34] Arno Klein, Jesper Andersson, Babak A Ardekani, John Ashburner, Brian Avants, Ming-Chang Chiang, Gary E Christensen, D Louis Collins, James Gee, Pierre Hellier, et al. Evaluation of 14 nonlinear deformation algorithms applied to human brain mri registration. *Neuroimage*, 46(3):786–802, 2009.

[35] WR Crum, T Hartkens, and DLG Hill. Non-rigid image registration: theory and practice. 2004.

[36] Ali Gholipour, Nasser Kehtarnavaz, Richard Briggs, Michael Devous, and Kaundinya Gopinath. Brain functional localization: a survey of image registration techniques. *Medical Imaging, IEEE Transactions on*, 26(4):427–451, 2007.

[37] Antonin Chambolle. An algorithm for total variation minimization and applications. *Journal of Mathematical imaging and vision*, 20(1-2):89–97, 2004.

[38] Keyvan Farahani, Bjoern Menze, Mauricio Reyes, Elizabeth Gerstner, Justin Kirby, and Jayashree Kalpathy-Cramer. Multimodal brain tumor segmentation (BRATS 2013), September 2013. URL `http://martinos.org/qtim/miccai2013/index.html`.

[39] Keelin Murphy, Bram Van Ginneken, Joseph M Reinhardt, Sven Kabus, Kai Ding, Xiang Deng, Kunlin Cao, Kaifang Du, Gary E Christensen, Vincent Garcia, et al. Evaluation of registration methods on thoracic CT: the EMPIRE10 challenge. *Medical Imaging, IEEE Transactions on*, 30(11):1901–1920, 2011.

[40] Daniel Rueckert, Luke I Sonoda, Carmel Hayes, Derek LG Hill, Martin O Leach, and David J Hawkes. Nonrigid registration using free-form deformations: application to breast MR images. *Medical Imaging, IEEE Transactions on*, 18(8):712–721, 1999.

[41] John Ashburner. A fast diffeomorphic image registration algorithm. *Neuroimage*, 38(1): 95–113, 2007.

[42] Maximilian Baust, Darko Zikic, Nassir Navab, and GER Munich. Diffusion-based regularisation strategies for variational level set segmentation. In *BMVC*, pages 1–11, 2010.

[43] Dimitri P Bertsekas. Nonlinear programming. 1999.

[44] Mindboggle, 2014. URL `http://www.mindboggle.info/`. Accessed: 2014-05-28.

[45] David W Shattuck, Mubeena Mirza, Vitria Adisetiyo, Cornelius Hojatkashani, Georges Salamon, Katherine L Narr, Russell A Poldrack, Robert M Bilder, and Arthur W Toga.

Construction of a 3d probabilistic atlas of human cortical structures. *Neuroimage*, 39(3): 1064–1080, 2008.

[46] The internet brain segmentation repository (IBSR) 2.0, 2014. URL `http://www.nitrc.org/projects/ibsr/`. Accessed: 2014-05-28.

[47] V Caviness, James Meyer, Nikos Makris, and D Kennedy. Mri-based topographic parcellation of human neocortex: an anatomically specified method with estimate of reliability. *Cognitive Neuroscience, Journal of*, 8(6):566–587, 1996.

[48] Mark Jenkinson, Peter Bannister, Michael Brady, and Stephen Smith. Improved optimization for the robust and accurate linear registration and motion correction of brain images. *Neuroimage*, 17(2):825–841, 2002.

[49] Feng Li, Pencilla Lang, Martin Rajchl, Elvis CS Chen, Gerard Guiraudon, and Terry M Peters. Towards real-time 3d us-ct registration on the beating heart for guidance of minimally invasive cardiac interventions. In *SPIE Medical Imaging*, pages 831615–831615. International Society for Optics and Photonics, 2012.

[50] Pencilla Lang, Martin Rajchl, Feng Li, and Terry M Peters. Towards model-enhanced real-time ultrasound guided cardiac interventions. In *Intelligent Computation and Bio-Medical Instrumentation (ICBMI), 2011 International Conference on*, pages 89–92. IEEE, 2011.

[51] Marc Modat, Gerard R Ridgway, Zeike A Taylor, Manja Lehmann, Josephine Barnes, David J Hawkes, Nick C Fox, and Sébastien Ourselin. Fast free-form deformation using graphics processing units. *Computer methods and programs in biomedicine*, 98(3):278–284, 2010.

[52] Guorong Wu, Minjeong Kim, Qian Wang, and Dinggang Shen. S-hammer: Hierarchical attribute-guided, symmetric diffeomorphic registration for MR brain images. *Human brain mapping*, 2012.

Chapter 5

Hierarchical Max-Flow Segmentation Framework For Multi-Atlas Segmentation with Kohonen Self-Organizing Map Based Gaussian Mixture Modeling

5.1 Introduction

Automatic partitioning of an image into multiple clinically relevant regions is a common yet challenging problem, which spans almost all of medical image analysis. In particular, the incorporation of intensity, spatial, and topological information into automatic brain segmentation has been a recurring subject of research in medical image analysis [1, 2, 3, 4, 5, 6, 7, 8].

This Chapter is adapted from an article currently in submission. M. Rajchl*, J.S.H. Baxter*, A.J. McLeod, J. Yuan, W. Qiu, T.M. Peters and A.R. Khan (2014). *Hierarchical Max-Flow Segmentation Framework For Multi-Atlas Segmentation with Kohonen Self-Organizing Map Based Gaussian Mixture Modeling.* Medical Image Analysis. *Authors contributed equally.

Many of these approaches to automatic partitioning have focused on the incorporation of a complex shape-model representing the entire anatomy [9], or the incorporation of large-scale medical image atlases [5, 10] containing images with these regions segmented a priori and often manually. The former often involves complex procedures to fit the model to the image which can experience difficulty in the presence of pathology. The latter suffers from issues associated with registration error, manual segmentation or user variability, and limited image variability in the atlas. A large portion of research in these areas has focused on overcoming these issues and expanding the scope of these methods.

In this chapter, we study a general approach to multi-region segmentation and test its applicability to the segmentation of brain structures from magnetic resonance images (MRI) based on our previous work [11]. The proposed method learns Gaussian Mixture models of image features derived from training data via Kohonen Self-Organizing Maps, and combines them with shape models generated from multi-atlas registrations. The information is fused and subsequently regularized via max-flow optimization in a globally optimal manner, where major components of the pipeline are parallelized using GPGPU for a substantial increase in computational efficiency.

5.1.1 Incorporating Intensity Information

With the increasing prevalence of multi-channel data in medical imaging, whether through multiple acquisitions or derived intensities, intensity distribution modelling has become increasingly necessary for image segmentation. Many machine learning approaches treat this as a classification problem, using a large number of channels (often derived, such as gradient magnitudes, or multi-scale image pyramids) as input vectors to a general purpose classifier such as a support vector machine or k nearest neighbours [12].

Other approaches have been centred more in probability theory, where the intensity distribution is explicitly modelled. Mixture models, specifically Gaussian mixture models trained

using variants of the expectation maximization algorithm [13, 8, 14] have been fairly popular due to their ability to capture information and correlations between multiple channels without prohibitive memory requirements or metrification artifacts.

5.1.2 Incorporating Spatial Information

One approach to the incorporation of spatial information is to consider it a specialized form of 'intensity'. Using the location of a point in a common co-ordinate system as a separate feature is a common approach in machine learning methods [12]. Learning the distribution of such information has also been used, either alone or in the context of another segmented object [13, 14].

Registration to an atlas is often used to encode spatial information either to assist in classification [15] or perform label fusion [3, 6].

5.1.3 Incorporating Topological Information

Markov Random Field modelling has been of increasing interest to the medical imaging community [2, 16, 17, 18, 19, 6, 7]. Specifically for multi-region image segmentation, there exist several computationally inexpensive solvers approximating global optimality. A recently published review on discrete and continuous Potts model regularization can be found in Nieuwenhuis et al. [20]. A commonly studied model for representing multi-region segmentation is the convex relaxed continuous Potts model [21, 22], minimizing:

$$E(u) = \sum_{\forall L} \int_{\Omega} (D_L(x)u_L(x) + S(x)|\nabla u_L(x)|)dx$$
$$\text{s.t. } u_L(x) \geq 0 \text{ and } \sum_{\forall L} u_L(x) = 1$$

where $u_L(x)$ represents a probabilistic segmentation of region L based on data terms, $D_L(x)$, and regularization term, $S(x)$.

The dual formulation of this relaxed Potts model amounts to a rapid optimization technique, which can be readily implemented using GPGPU on commercially available hardware to achieve substantial improvements in computation speed. However, these models have difficulty in managing multi-region segmentation problems in which several regions have individual regularization requirements not represented by a single smoothness term [23]. This lack of topological knowledge has lead to the development of more nuanced max-flow segmentation models such as Ishikawa models [24, 25, 26] although said models are constrained to segmentation problems in which the relationships between objects can be expressed using a full-ordering. This constraint poses difficulty for the segmentation of anatomy in which the part/whole relationships cannot be defined as such.

Recently, irregular hierarchical models have been proposed to address problems in which the labels are not expressed as fully ordered, but have differing regularization requirements. In a former study [27], we proposed a method based on a partially ordered Potts model.

This approach allows for labels to be grouped and regularized together and can thus treat label groups with different smoothness constraints. The dual formulation also permits a GPGPU-based implementation. As of yet, however, these hierarchies have been limited in the number of labels, and have traditionally been hard-coded, and therefore not readily extendable to larger segmentation problems. An extendable hierarchical version of discrete graph cuts using the h-fusion algorithm similar to $\alpha\beta$-swap has recently been proposed to address some of these topological problems [28]. However, as with other discrete graphical models, this method suffers from the same limitations compared to their continuous counterparts [22, 20].

5.1.4 Contributions

We have developed a series of segmentation support tools and constructed a multi-atlas tissue segmentation framework. Novel tools include:

1. A Kohonen self-organizing map (KSOM) based intensity distribution modelling mechanism that takes advantage of the dual probabilistic and manifold-learning nature of these

networks, and

2. A max-flow solution algorithm to general hierarchical segmentation problems where the topological is expressed not as a Potts model or Ishikawa ordering, but an arbitrary hierarchy, which can be modified in run-time, minimizing recompilation.

These tools, as well as label-fusion techniques, can be combined into a optimization-based segmentation framework addressing the *maximum a posteriori* probability problem. In addition, we have released open-source CPU and GPGPU implementations online (*http://sourceforge.net/projects/asets/*) to ensure reproducibility.

We assess our framework in terms of accuracy against a conventional convex-relaxed continuous Potts model. The datasets used for this validation are both publicly available neuroimaging databases, specifically the OASIS database [29, 30] and the MRBrainS2013 database [31].

5.2 Methods

Our method involves four major components, each of which will be discussed in detail. These methods were combined in the pipeline shown in Figure 5.1.

5.2.1 Generalized Hierarchical Max-Flow Segmentation

Generalized Hierarchical Max-Flow (GHMF) models [32] generalize both Potts and Ishikawa models, minimizing energy functionals of the form:

$$\min_{u} \quad \sum_{\forall L} \int_{\Omega} \left(D_L(x) u_L(x) + S_L(x) |\nabla u_L(x)| \right) dx \tag{5.1}$$

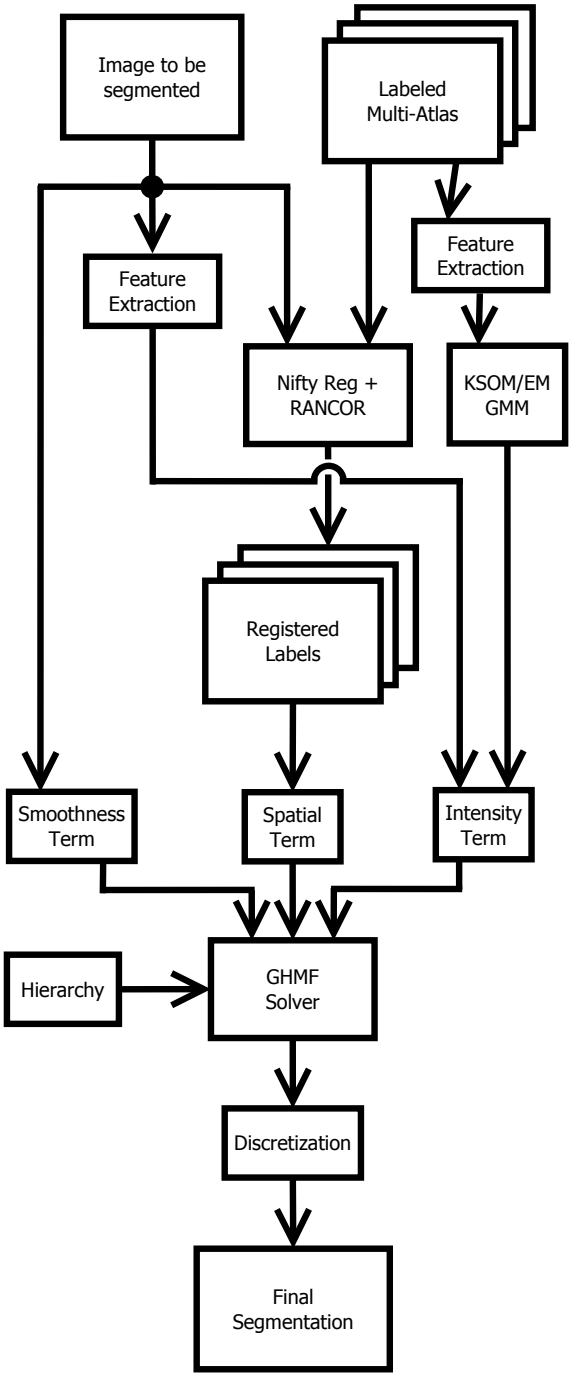

Figure 5.1: Segmentation Pipeline

subject to the constraints:

$$\begin{aligned} &\forall L,\ u_L(x) \geq 0 \\ &\forall L,\ \sum_{L' \in L.C} u_{L'}(x) = u_L(x) \\ &u_S(x) = 1 \end{aligned} \tag{5.2}$$

in which $L.C$ refers to the children, or the partition, of L. In this formulation, the regions must be arranged in a tree where each parent region is partitioned into its child regions and a specialized root node, S, representing the entire image. From here on, trees of this form will be referred to as hierarchies. (The specific hierarchies used are shown in Figures 5.3 and 5.4.) These hierarchies have been previously used to express topological considerations in image segmentation, specifically part/whole relationships [4, 28].

A distinct advantage of such a general formulation is that it is sufficiently expressive to represent a super-factorial number of hierarchies including all possible Potts and Ishikawa models, which is considerably larger asymptotically than either the 1 possible Potts model or the $N!$ possible Ishikawa models given N labels. This indicates that a larger class of segmentation problems can be addressed with the GHMF formulation than previous extendable formulations, allowing for more topological information (specifically in the form of part/whole relationships) to be explicitly included in the optimization-based segmentation framework [32].

Additionally, GHMF has a more flexible regularization parameter space in stark contrast to the one parameter Potts model commonly used.

This problem expressed in (5.1) and (5.2) can be addressed through a primal-dual optimization framework similar to that proposed by [22], displaying the equivalence of (5.1) to the primal model:

$$\max_{p,q} \int_{\Omega} p_S(x)dx \tag{5.3}$$

subject to the flow conservation constraint:

$$G(x) := \text{div}q_L(x) + p_L(x) - p_{L.P}(x) = 0 \,, \tag{5.4}$$

spatial flow capacities:

$$\forall L,\ |q_L(x)| \leq S_L(x) \,, \tag{5.5}$$

and sink capacities:

$$\forall L \text{ s.t. } L.C = \emptyset,\ 0 \leq p_L(x) \leq D_L(x)\ . \tag{5.6}$$

Without loss of generality, we consider only the leaf nodes (that is, nodes where $L.C = \emptyset$) to have non-zero data terms [32]. The primal model (5.3) and dual model (5.1) can both be shown to be equivalent to the following primal-dual model using a Lagrangian multiplier over the flow conservation constraint (5.4):

$$\min_{u} \max_{p,q} \left(\int_{\Omega} p_S(x)dx + \sum_{\forall L \neq S} \int_{\Omega} u_L(x) G_L(x) dx \right), \tag{5.7}$$

subject to (5.5) and (5.6) which can be addressed computationally through augmentation [33] as:

$$\begin{aligned} \min_{u} \max_{p,q} \Bigg(& \int_{\Omega} p_S(x)dx + \sum_{\forall L \neq S} \int_{\Omega} u_L(x) G_L(x) dx + \\ & \frac{c}{2} \sum_{\forall L \neq S} \int_{\Omega} G_L(x)^2 dx \Bigg)\ . \end{aligned} \tag{5.8}$$

This minmax optimization problem can be decomposed into a sequence of highly parallelizable tasks, making it suitable for GPGPU acceleration. Our implementation takes advantage of Compute Unified Device Architecture (CUDA) (NVIDIA, US) integrated into the Visualization Toolkit (VTK) library (Kitware, US). In addition to the fine-grained parallelism within individual tasks, there are additional coarse-grained concurrent execution possibilities between tasks, allowing for multiple GPUs to be used simultaneously on a single segmentation problem to further improve performance. Details concerning the solver are provided by [32].

The cost terms were generated using both a spatial/shape framework discussed in Section 5.2.2 and an intensity framework discussed in Section 5.2.3.

5.2.2 Deformable Registration and Atlas

The first step in our segmentation pipeline is to register the incoming image to our atlas of images that have been manually segmented *a priori*. To achieve this, we used a convex optimiza-

tion based deformable registration method, RANCOR [34], with an affine initialization from the Nifty Reg package [35]. The similarity metric used in RANCOR was the sum of absolute differences between images and total-variation regularization on the underlying deformation fields was used to ensure that they maintain topological consistency and avoid erroneous trivial solutions or singularities in the resulting deformation field. The underlying objective function being minimized is:

$$\min_{t} \int_{\Omega} |I_1(x) - I_2(x + t(x))| + \sum_{i=1}^{3} |\nabla_x t_i(x)| dx \tag{5.9}$$

where $I_1(x)$ and $I_2(x)$ represent the underlying images and $t(x)$ represents the underlying deformation field. Due to the non-linearity of $I_1(x)$ and $I_2(x)$, this function is obviously non-convex. To address this, a multi-scale coarse-to-fine optimization framework is used where the optimal coarser-grained deformation fields are used to initialize the finer-grained ones in a dual-optimization framework [34].

Once the current image has been registered to each image in the atlas, an initial set of labels can be propagated. Since multiple images are used, each with its own labeling, fusion methods are required to combine this information or to distill probabilistic approximations and log-likelihood cost terms. For this, we investigated two methods:

- Mean label fusion (MLF) is the simplest label fusion technique. Probability maps are created based solely on the percentage of atlases choosing a particular label for a particular voxel, that is:

$$P(x \in L) = \frac{\text{\# of atlases with voxel } x \in L}{\text{\# of atlases}}.$$

- Joint label fusion (JLF) [10] develops probability maps similar to MLF, but weights the atlases at each voxel, based on the joint probability of multiple atlases making incorrect labellings simultaneously. This probability is estimated from the difference in intensity in a local neighbourhood between the atlases and the target image.

5.2.3 Kohonen Self-Organizing Map Based Mixture Modeling and Optimization Costs

One of the most common data term structures is based on applying Bayes' theorem to the image intensity using *a priori* trained intensity distribution models, either from sampled voxels from the image to be segmented [16] or a prior segmented atlas [5]. The latter is implemented in our framework using the data term:

$$D_L(x) = -\ln\left(P(I(x)|x \in R_L)\right) \ . \tag{5.10}$$

Gaussian mixture models (GMMs) are widely known to be a flexible alternative to histogram-based intensity distribution representation, especially well suited to multi-channel segmentation in which the storage space required by histograms becomes prohibitive and metrification artifacts degrade derived statistical measures. These models describe a general distribution as:

$$P\left(I(x)\right) = \sum_{i=1}^{N} w^{(i)} \mathcal{N}(\mu^{(i)}, \Sigma^{(i)}) \ . \tag{5.11}$$

which are normally trained using the Expectation Maximization (EM) algorithm [36]. Despite its popularity, this algorithm is known to have a number of limitations especially sensitivity to initialization and the dominance of a few components with higher weight over a larger number of lower weighted components.

Since their inception, Kohonen self-organing maps (KSOMs) [37] have received a large degree of interest in the machine learning community for clustering, manifold learning, and dimensionality reduction purposes. Recently, several approaches have been made to consolidate KSOMs with GMMs [38, 39, 40] through modifications to the expectation-maximization (EM) algorithm, the traditional method for GMM training. To reduce the memory requirements for the GMM, the covariance matrix was assumed to be diagonal with variance $v_j^{(i)}$ for Gaussian component i and channel j. The particular KSOM-based training algorithm used is given in

Figure 5.2. This algorithm was also accelerated using GPGPU programming in order to ensure computational performance.

Initialize $w^{(i)}$, $\mu^{(i)}$, and $v^{(i)}$ ensuring that $\sum_{\forall i} w^{(i)} = 1$, $w^{(i)} \geq 0$, $v_j^{(i)} > 0$

while not converged **do**

Pick some sample subset, $S \subset \{1, 2...V\}$

$$s \in S, h^{(i,s)} \leftarrow w^{(i)} g(x^{(s)} | \mu^{(i)}, v^{(i)})$$

$$s \in S, h^{(i,x)} \leftarrow h^{(i,s)} / \sum_{j=1}^{M} h^{(j,s)}$$

$$\forall s \in S, c^{(s)} \leftarrow \underset{\{i\}}{\operatorname{argmin}}\, h^{(i,s)}$$

$$w^{(i)} \leftarrow (1-\alpha) w^{(i)} + \frac{\alpha^{(t)}}{|S|} \sum_{s \in S} \left(h^{(i,s)} - w^{(i)} \right)$$

$$\mu^{(i)} \leftarrow (1-\alpha) \mu^{(i)} + \frac{\alpha^{(t)}}{|S|} \frac{\sum_{s \in S} \mathcal{N}^{(t)}_{|i-c^{(s)}|} h^{(i,s)} (x^{(s)} - \mu^{(i)})}{\sum_{s \in S} \mathcal{N}^{(t)}_{|i-c^{(s)}|} h^{(i,s)}}$$

$$v^{(i)} \leftarrow (1-\alpha) v^{(i)} + \frac{\alpha^{(t)}}{|S|} \frac{\sum_{s \in S} \mathcal{N}^{(t)}_{|i-c^{(s)}|} h^{(i,s)} ((x^{(s)} - \mu^{(i)})^2 - v^{(i)})}{\sum_{s \in S} \mathcal{N}^{(t)}_{|i-c^{(s)}|} h^{(i,s)}}$$

end while

Figure 5.2: KSOM-Based GMM Training

In terms of initialization, we take advantage of the relationship between KSOM training and manifold learning or dimensionality reduction. We use a Principle Component Analysis based initialization, where the Gaussian components in the mixture model are initially uniformly spaced in a plane dictated by the first N principle components of the training images, corresponding to the N-dimensional Gaussian component indexing scheme. (For this application we have chosen $N = 2$, which allows for ready visualization of the maps to ensure fidelity.) This ensures that linear components of the intensity distribution are automatically handled through the initialization, and guarantees more repeatable and therefore comparable maps despite the random component present in data subset selection.

5.2.4 Smoothness Terms

Smoothness terms were created sensitive to edges in the image identified by local intensity changes. The smoothness cost was correspondingly:

$$S_L(x) = \alpha_L * \exp\left(\frac{-\lambda|\nabla I(x)|}{1 + |\nabla(k * I(x))|}\right), \tag{5.12}$$

where k is a Gaussian kernel and the parameter α_L is specified per label in GHMF.

The normalization by local contrast allows for a single smoothness field to be used for all regions despite discrepancies in contrast between regions. This reduces the amount of parameterization necessary in the segmentation pipeline, and allows it to generalize more effectively across different MR acquisitions.

5.3 Experiments

Two experiments were performed to investigate the efficacy of KSOM-based GMMs over traditional EM-based approaches, and the applicability of hierarchies over the more commonly-used continuous Potts model [20].

5.3.1 OASIS Database

The MICCAI 2012 Grand Challenge and Workshop on Multi-Atlas Labeling [30] recently released all training and test data to the pubic. It provides 15 training and 20 test datasets from the Open Access Series of Imaging Studies (OASIS) database [29] with manually segmented label maps performed by [41]. Each entry in the database contains a defaced T1-weighted volume (MPRAGE sequence at 1.5-T, TR = 9.7, TE = 4.0, TI = 20.0, flip angle = 10°) with 1x1x1.25 mm voxel sizes.

The labeling protocol for the OASIS database in its original form is a brain parcellation protocol using 134 labels. These original labels were fused to a tissue segmentation protocol

containing background (BG), cortical gray matter (cGM), subcortical gray matter (sGM), white matter (WM), ventricles (V) and brain stem (BS).

Ten features are extracted from the input T1w image: i) the image intensity, ii) the intensity after convolution with a Gaussian kernel of $\sigma = 1, 2, 3\, mm^3$, iii) the gradient magnitude of the intensity after convolution with a Gaussian kernel of $\sigma = 1, 2, 3\, mm^3$ and the Laplacian of the intensity after convolution with a Gaussian kernel with $\sigma = 1, 2, 3\, mm^3$. All images are normalized to unit standard deviation within the brain mask to ensure intensity consistency. These features allow us to create a 'synthetic multi-channel' image (as opposed to multiple distinct MR sequences) that captures intensity information on multiple scales.

5.3.2 MRBrainS Database

To evaluate our segmentation method on multi-channel data, we used the MRBrainS 2013 database [31] which contains twenty entries each with three images, a T1-weighted, T2 Fluid Attenuated Inversion Recovery (FLAIR), and T1 inversion recovery (IR) image all at 3-T with a voxel size of 0.96x0.96x3.00 mm and co-registered into a single co-ordinate space. Five datasets were provided for training and 15 for testing purposes.

The MRBrainS labels to be segmented contained background (BG), cortical gray matter (cGM), subcortical gray matter (sGM), white matter (WM), white matter lesions (WML), external cerebro-spinal fluid (eCSF), and ventricles (V).

For MRBrainS segmentation, we used all three provided intensity channels: i) T1w, ii) T2 FLAIR and iii) T1 IR as features. All images are normalized to unit standard deviation using the brain mask to ensure intensity consistency.

As evaluation on this database was done externally (ground truth was provided only for the five training datasets) and with limited submissions, only the highest performing combination of components (i.e. KSOM GMM learning with JLF under GHMF regularization) of our framework, based on the results from the OASIS database, was evaluated. This, however, allowed for quantitative comparison against other submissions representative of the state-of-

the-art in multi-region brain segmentation.

5.3.3 Multi-Atlas Image Registration

All images were bias-corrected using the approach of [42] and normalized [6]. All training images were then affinely registered using a block-matching technique [35] (default parameters). Subsequent deformable registration was performed using RANCOR, a GPGPU-enhanced deformable registration using a Gauss-Newton optimizer, with total-variation regularization ($\alpha_{Reg} = 0.05$) and the sum of absolute intensity differences as a similarity metric in a multi-resolution manner [34]. Using the registered images, a brain mask is automatically generated from computed spatial priors. For the purpose of the MRBrainS challenge, we fused all registered WM and WML labels to obtain a combined WM label for the spatial term.

5.3.4 Learning GMMs via KSOMs

Image features are generated from each training image and used to learn GMMs via the proposed KSOM method. All features were used in the training of the 2D KSOMs of size $32x32$ for 112 epochs and GMMs of equivalent size using conventional EM [36] for 112 epochs. To compare these distributions, we used the Kullback-Leibler divergence:

$$D_{KL}(P||P_{est}) = \sum_i \ln\left(\frac{P(i)}{P_{est}(i)}\right) P(i) \tag{5.13}$$

where i is a (vector-valued) intensity, $P(i)$ is the true intensity distribution and $P_{est}(i)$ is the estimated distribution. Because the true distribution is not fully known outside of the estimates $P_{KSOM}(i)$ and $P_{EM}(i)$, we cannot estimate D_{KL} directly. However, we can estimate the difference

in D_{KL} between methods by:

$$\begin{aligned}
&D_{KL}(P||P_{EM}) - D_{KL}(P||P_{KSOM}) \\
&= \sum_i \ln\left(\frac{P(x)}{P_{EM}(i)}\right) P(i) - \sum_i \ln\left(\frac{P(i)}{P_{KSOM}(i)}\right) P(i) \\
&= \sum_i \left(\ln\left(\frac{P(i)}{P_{EM}(i)}\right) - \ln\left(\frac{P(i)}{P_{KSOM}(i)}\right)\right) P(i) \\
&= \sum_i \left(\ln P_{KSOM}(i) - \ln P_{EM}(i)\right) P(i) \\
&\approx \frac{1}{V} \sum_x \left(\ln P_{KSOM}(x_i) - \ln P_{EM}(x_i)\right)
\end{aligned} \tag{5.14}$$

where x_i is the intensity of voxel x from the V testing voxels.

Data Costs for Segmentation

As stated in the previous section, our data terms are composed of two probabilistic frameworks: the first from the intensity model and the second from a label fusion mechanism. We used two label fusion methods for the purpose of these experiments: i) mean label fusion using GPGPU and subsequently convolved with a Gaussian kernel ($\sigma = 0.75$) and ii) using the JLF method in [10] using the ANTs [43] package. Due to the low number of available training images in the MRBrainS database ($N = 5$) we left/right flipped the training datasets to artificially create more images for the multi-atlas which allows for more accurate priors.

The energy (5.1) is optimized where $D_L(x)$ is:

$$D_L(x) = -\log P(I(x)|L) \; - \beta_L \; \log(P(S_L(x)), \tag{5.15}$$

and $P(S_L(x)$ and $P(I(x)|L)$ are the probabilities generated from the intensity model and the label fusion mechanism, respectively. The parameter β_L allows for the weighting of the intensity and label fusion information to vary between labels based on which have more distinguishable contrast but lower registration accuracy (such as eCSF) or low contrast with higher registration

accuracy (such as sCGM). The $S_L(x)$ was defined in (5.12).

Hierarchy and Parameters

The hierarchies are given in Figures 5.3 and 5.4. (The S node refers to the entire image. That is: $u_S(x) = \sum_{\forall L \in \mathbb{L}} u_L(x) = 1$.) These hierarchies were chosen heuristically based on the adjacency and any shared regularization requirements of the regions to be segmented. The segmentation parameters are given in Table 5.1. (Note that only segmented labels are associated with data terms and have β_L parameters.)

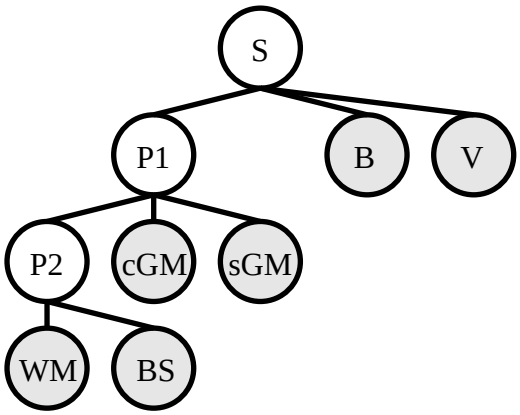

Figure 5.3: MICCAI 2012 OASIS - Segmentation Hierarchy
** segmented labels are shown in gray: B - background, V - ventricles, cGM - cortical gray matter, sGM - subcortical gray matter, WM - white matter, BS - brain stem*

All segmentation parameters were tuned on the training data in a leave-one-out manner. λ and the β_L parameters were tuned through brute force search to maximize the DSC on the training databases for the Potts model, along with the Potts smoothness parameter. The GHMF smoothness parameters, α, were tuned heuristically due to the large parameter space using the β_L parameters tuned previously, ensuring that the Potts and GHMF models were given the same data costs and are comparable.

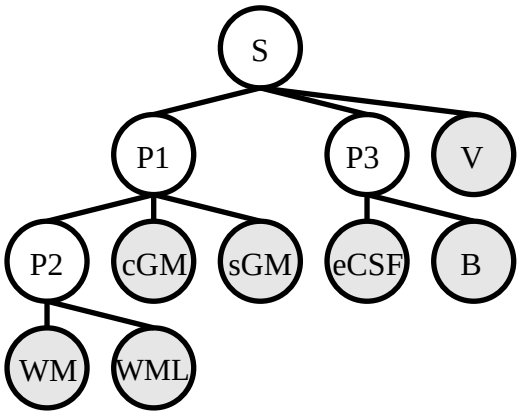

Figure 5.4: MICCAI 2013 MRBrainS - Segmentation Hierarchy
** segmented labels are shown in gray: B - background, eCSF - external cerebro-spinal fluid, V - ventricles, cGM - cortical gray matter, sGM - subcortical gray matter, WM - white matter, WML - white matter lesions*

5.3.5 Segmentation Evaluation Metrics

Each segmentation was evaluated along the lines of three metrics per label, L, where R_L represents the generated segmented region, and $R_L^{(G)}$ indicates the gold standard segmentation:

- The *Dice similarity coefficient* (*DSC*) as a regional metric:

$$DSC_L = \frac{2|R_L \cap R_L^{(G)}|}{|R_L| + |R_L^{(G)}|} \tag{5.16}$$

- The *absolute volume difference* (*VE*) as a volumetric metric:

$$AVD_L = \frac{|R_L| - |R_L^{(G)}|}{|R_L^{(G)}|} \tag{5.17}$$

- The *modified Hausdorff distance* (*MHD*) as a distance metric, where MHD is the 95th-percentile of the Hausdorff distance (HD):

$$HD_L = \max_{p \in \delta R_L} \min_{p' \in \delta R_L^{(G)}} |p - p'| \tag{5.18}$$

	MLF		JLF	
	α_L	β_L	α_L	β_L
	OASIS $\lambda = 1$			
BG	0.5	3	0	12.5
cGM	75	9	70	22.5
sGM	0.6	3.5	2	20
WM	10	0.25	2.5	9
V	60	20	80	25
BS	0.75	2.0	0.25	14
P1	0.05		0.05	
P2	0.5		0.1	
Potts	1.25		3.0	
	MRBrainS $\lambda = 0.25$			
BG			2.0	10.0
cGM			0.05	2.25
sGM			0.6	1.5
WM			0	0.5
WML			0.05	0.75
eCSF			3.0	3.0
V			10.0	0.5
P1			0.025	
P2			0.025	
P3			0.025	

Table 5.1: Segmentation Parameters: Parameters for the four comparative algorithms are shown for OASIS. MRBrainS was only evaluated using the GHMF+JLF algorithm.

5.3.6 Implementation details

Each element in the proposed segmentation pipeline is implemented in C++ and CUDA (NVIDIA Corp., Santa Clara, CA) and wrapped in VTK (Kitware Inc., Clifton Park, NY) filters and made available publicly within the ASeTs repository on *https://sourceforge.net/projects/asets/*. The JLF technique in [10] was released within the Advanced Normalization Tools (ANTs) [43] and the elements of the registration pipeline are available within the RANCOR [34, 44] and *Nifty Reg* packages [45].

5.4 Results

5.4.1 Intensity Distribution Results

As stated in Section 5.3.4, the intensity distribution models were evaluated based on the difference in Kullback-Leibler divergence. For the sampling of the ground truth distribution, we used the entire test set of images. This also maintained the separation of training and testing data. The results for foreground labels in terms of the natural unit (nat) of continuous information using equation 5.14 are presented in Table 5.2. Positive results indicate that KSOM produces a lower divergence than EM and negative indicate the opposite.

		ΔD_{KL} (nats)
MICCAI 2012	cGM	**2.9 ± 5.0**
OASIS	sGM	**420.6 ± 108.5**
	WM	**35.7 ± 8.8**
	BS	**821.2 ± 480.0**
	V	75.8 ± 273.7

Table 5.2: Intensity Distribution Validation

Results were significant to $p < 0.05$ after Bonferroni correction are shown in bold.

5.4.2 Run Times

Maximum run times for the various framework components are presented in Table 5.3.

5.4.3 Segmentation Results

The quantitative segmentation results are reported for the MRBrainS database in Table 5.4 and for the OASIS database in Table 5.5. For the OASIS database, the evaluation is done in pairs, comparing Potts with GHMF. Significantly better results (in terms of a two-tailed t-test with $p \leq 0.05$) are shown in bold for both Potts and GHMF.

Visual segmentation results (using the GHMF+JLF version of the algorithm) are presented for OASIS (Figure 5.5) and MRBrainS (Figures 5.6 and 5.7) displaying both best case and

OASIS	Max. Run Time [min]
Affine Reg.	1.85
Deformable Reg.	1.35
MLF	0.07
JLF	57.0
Regularization	1.25
Total w/ MLF	49.32
Total w/ JLF	106.25
MRBrainS	
Affine Reg.	0.62
Deformable Reg.	0.68
JLF	11.0
Regularization	0.65
Total w/ JLF	24.65

Table 5.3: Maximum run times.

worst case results. Enlarged regions of interest (ROIs) with high disagreement between our segmentation results and the gold standard are also shown. For all rows, the underlying image (or images) are shown on the left, followed by the gold standard in the center, and then our segmentation on the right.

MRBrainS		GHMF + JLF
DSC	CSF	82.10 ± 4.42
	GM	84.13 ± 1.46
	WM	87.96 ± 1.11
	mean	84.73 ± 3.65
AVD	CSF	12.78 ± 11.57
	GM	5.44 ± 3.81
	WM	6.59 ± 4.81
	mean	8.27 ± 8.08
MHD	CSF	2.71 ± 0.72
	GM	1.92 ± 0.00
	WM	2.49 ± 0.46
	mean	2.37 ± 0.59

Table 5.4: Segmentation Results - MRBrainS

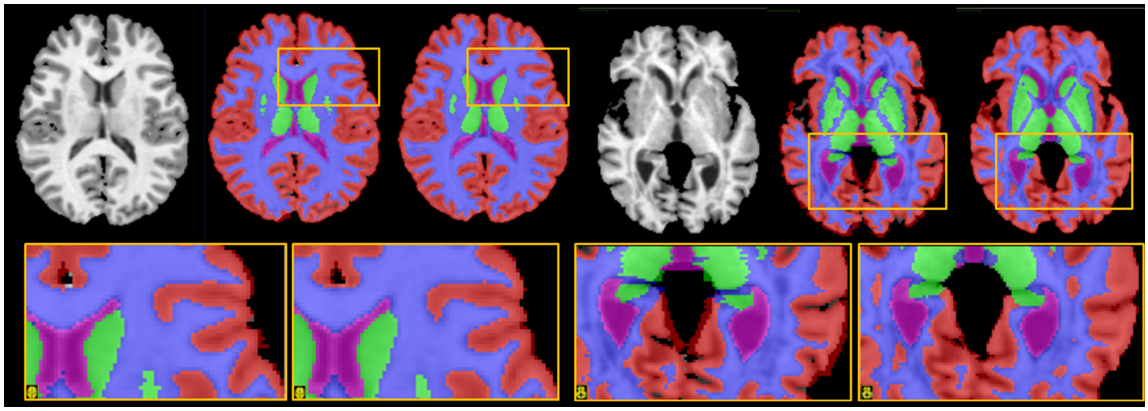

Figure 5.5: Best and Worst Case Visual Results - OASIS (top row: best case T1w image, gold standard, proposed method, worst case T1w image, gold standard, proposed method. bottom row: enlarged ROIs)

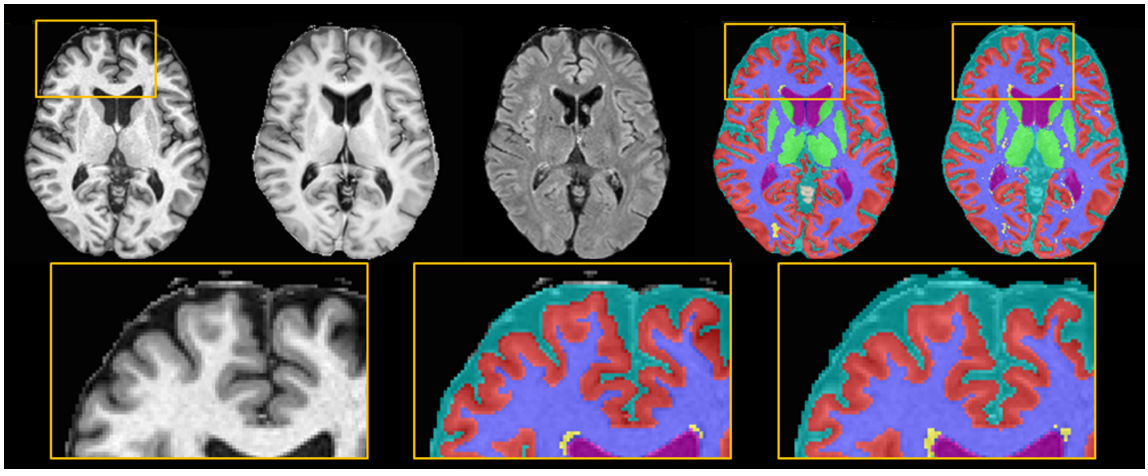

Figure 5.6: Best Case Visual Results - MRBrainS (top row: T1w, T1IR, T2FLAIR, gold standard, proposed method. bottom row: enlarged ROI)

OASIS	Potts + MLF	GHMF + MLF	Potts + JLF	GHMF + JLF
DSC				
cGM	86.00 ± 4.72	**86.36 ± 4.43**	88.42 ± 3.39	**88.88 ± 3.32**
sGM	85.45 ± 4.3	**86.06 ± 3.84**	91.06 ± 1.77	**91.10 ± 1.78**
WM	89.68 ± 3.95	**89.93 ± 3.53**	92.47 ± 2.73	**92.56 ± 2.67**
V	87.41 ± 3.61	**87.53 ± 3.58**	91.14 ± 3.07	**91.22 ± 3.01**
BS	89.05 ± 2.24	89.11 ± 2.25	92.96 ± 0.92	**92.99 ± 0.92**
mean	87.52 ± 3.76	**87.80 ± 3.52**	91.21 ± 2.38	**91.35 ± 2.34**
AVD				
cGM	7.00 ± 5.63	**5.65 ± 4.58**	4.17 ± 2.85	3.76 ± 2.50
sGM	8.91 ± 8.44	**7.16 ± 7.35**	3.45 ± 2.04	**3.22 ± 1.90**
WM	11.59 ± 11.81	**10.19 ± 10.93**	7.70 ± 7.13	**7.50 ± 7.00**
V	14.26 ± 10.58	14.74 ± 10.51	6.97 ± 5.33	6.77 ± 5.55
BS	8.18 ± 5.84	**6.93 ± 5.88**	5.00 ± 2.20	2.66 ± 2.11
mean	9.99 ± 8.46	**8.94 ± 7.85**	5.00 ± 3.87	**4.78 ± 3.81**
MHD				
cGM	2.18 ± 0.26	2.20 ± 0.22	2.18 ± 0.38	**1.99 ± 0.34**
sGM	1.98 ± 0.50	1.95 ± 0.50	1.31 ± 0.27	1.30 ± 0.23
WM	1.55 ± 0.44	1.56 ± 0.43	1.17 ± 0.32	1.19 ± 0.36
V	**1.79 ± 0.60**	1.91 ± 0.57	1.18 ± 0.21	1.20 ± 0.23
BS	2.21 ± 0.46	2.23 ± 0.44	1.56 ± 0.26	**1.54 ± 0.26**
mean	1.94 ± 0.45	1.97 ± 0.43	1.48 ± 0.29	**1.44 ± 0.28**

Table 5.5: Segmentation Results - OASIS: *significantly better metrics are shown in bold*

5.5 Discussion

5.5.1 Accuracy

At the time of writing, our multi-atlas framework was the highest ranking framework submitted to the MRBrainS competition. These rankings are an aggregate measure of quality across the numerical results shown in Table 5.4.

In both our best case and worst case, there is a slight over-regularization of cortical folds likely due to some uncertainty in the intensity priors and spatial priors as a result of partial volume effects and registration error respectively. In the worst case image, white matter lesions are largely over-segmented, and the regularization term has difficult maintaining elongated structures such as the posterior horn of the ventricle.

GHMF shows a slight improvement over the Potts model using the same data terms across

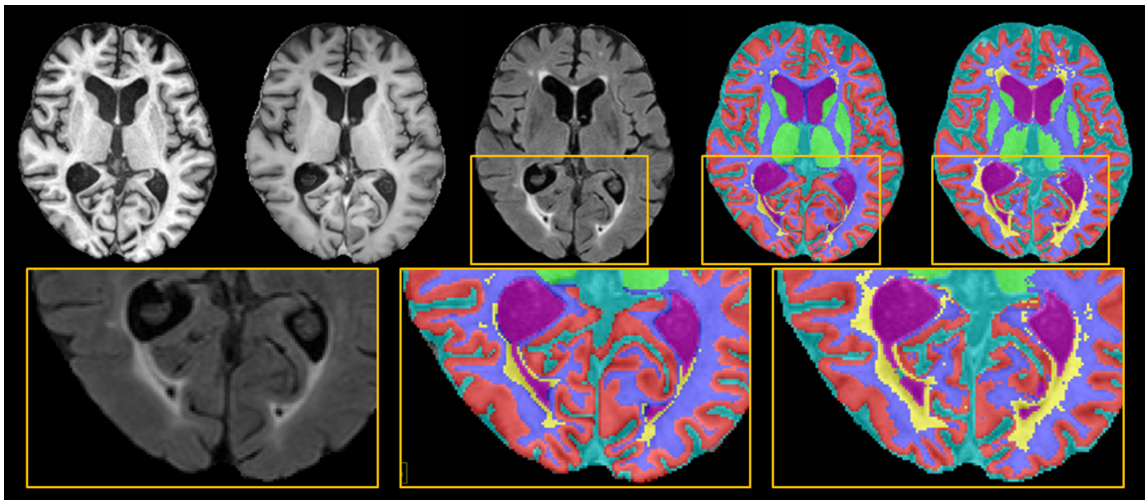

Figure 5.7: Worst Case Visual Results - MRBrainS (top row: T1w, T1IR, T2FLAIR, gold standard, proposed method. bottom row: enlarged ROI)

most metrics (23 out of 30), DSC (which both were tuned for) in particular. Although this difference is slight, it is significant in many places. Out of the 30 metrics evaluated, GHMF outperformed Potts on 17, Potts outperformed GHMF on 1, and the remaining 12 were not significant. GHMF also outperformed Potts significantly on 5 of the 6 aggregate metrics.

In terms of our visual results, our worst case scenario was dominated by white matter lesions. These lesions have a similar intensity as gray matter, making them more difficult to distinguish based on the intensity models. This caused the mis-segmentation of white matter lesions as gray matter. This can be mitigated by the incorporation of T2 FLAIR acquisitions and the inclusion of white matter lesions as a separate segmentation label. However, neither were available in the OASIS database.

The λ and β_L parameters were tuned specifically for the Potts model. This implies that our results are, in theory, biased towards improved Potts models, which, along with the limited size and variability in the gold standard segmentations, could lead to an understatement of the improvements yielded by incorporating more complex, representative topological information using GHMF.

5.5.2 Generality and Hierarchy Selection

Our framework has been designed with generality across applications and modalities in mind.

The improvement of GMM trained via Kohonen self-organizing maps over expectation maximization is known in the literature for synthetic problems [38, 39, 40]. This improvement is expected in any case where the underlying distribution displays some continuum behaviour (such as intensity variation resulting from magnetic field inhomogeneity in MRI) or generally requires a large number of Gaussian components. (These results are reflected in our evaluation as shown by Table 5.2.) In addition, the duality displayed in KSOMs as being both a continuous manifold and probability distribution could yield insights into methods of dimensionality reduction, useful in image processing outside of segmentation. This makes KSOM-based GMMs a theoretically sound tool for modelling intensity distributions in multi-channel images above those achieved with EM.

Our framework also allows for more generality in terms of the geometrical relationships of the labels being segmented. Unlike the Potts and Ishikawa models, which have relatively few possibilities, GHMF models allow for a large number of hierarchies to be defined expressing a wide degree of geometric knowledge. However, there are issues associated with the selection of hierarchies which do not have an analogue in the simpler models. For the OASIS database, we performed a six label segmentation that was arranged in one of the 2752 possible hierarchies. The seven label case from the MRBrainS database corresponds to 39208 hierarchies [46] and the number of possible hierarchies grows super-factorially with the number of labels being segmented. Because of the sheer number of hierarchies, a full exploration of hierarchical models is impossible in general.

5.5.3 Run Time and Applicability

One issue with multi-region segmentation currently is the prohibitive run times associated with these processes. Some components' run times scale with the number of atlases included, specifically the registration and label fusion components.

All components were GPGPU accelerated with the exceptions of affine registration and JLF, for which open source implementations were used. This resulted in a maximum runtime on the OASIS database and MRBrainS of 106 and 23 minutes, respectively. In both cases, the most time prohibitive portion of our framework is the joint label fusion [10] taking approximately 50% of the total run time. In future, this technique could be implemented in a GPGPU accelerated form to address this issue, or more computationally inexpensive techniques such as mean label fusion could be used.

The computational feasibility and theoretical generality indicate that our multi-atlas segmentation framework should be applicable to a wide array of multi-region segmentation problems.

5.5.4 Combinatorial Optimality

Previous optimal variational approaches such as those presented in [25] and [47] have considered optimality in both the relaxed and combinatorial contexts. These methods have shown the strong duality, proven for the relaxed method, indeed applies under integrality constraints through simple, linear-time operations such as thresholding. Because GHMF is a generalization of these segmentation problem classes, it makes the same guarantees and similar processes can be used to guarantee the combinatorial optimality of GHMF results conditioned on properties of the hierarchy. For example, if the hierarchy can be transformed into an Ishikawa model in polynomial time, global optimality in the discrete case can be guaranteed [32].

However, it is well known that simple multi-region segmentation configurations, such as the Potts model, are NP-hard even constrained to finite lattice graphs [48] which is a strong indication that this duality gap for general hierarchies in a variational sense may not be bridged with simultaneous computational efficiency and theoretical optimality. This problem has been well documented for the continuous Potts model in particular [20, 21, 22].

5.5.5 Similar approaches

The proposed method is similar to the hierarchical approach taken by [4]. In terms of similarities, both frameworks take advantage of multi-channel data using a probabilistic intensity model. Both use deformable registration to define probabilistic spatial priors. Most notable, both frameworks express the topological relationships, specifically part/whole relationships, in the form of a hierarchy or tree.

Conceptually, this structure describes a series of segmentations in which each object is subdivided into its constituent parts, the final segmentation being the collection of 'indivisible' labels. In [4], this interpretation is implemented directly, resulting in a series of segmentation problems each referring to a subdivision mentioned above. Our framework on the other hand, using a large-scale graphical model, addresses the optimization problem directly with one simultaneous segmentation of all labels while still maintaining this topological structure. This addresses a weakness identified by [4], specifically that a purely top-down framework would not be able to recover from early-stage segmentation errors.

Another key difference between these frameworks is the scale of the probabilistic intensity model. [4] used single Gaussians as the distribution for each label. Although the parameters of these Gaussians could be learned with certain optimality, they do not have the flexibility of our large-scale, KSOM based Gaussian mixtures to capture continuous shifts in the intensity distribution caused by inhomogeneities either in the tissues or underlying magnetic field.

5.5.6 Future Work

There are many directions in which to take this segmentation approach. The first is to extend our results to a variety of complex, multi-faceted anatomies outside of brain segmentation, and to extend our results within brain segmentation to atlases and labeling protocols with a large number of regions such as those presented in other open brain image databases.

To mitigate for the effects of hierarchy selection, we could transition to more advanced max-flow solution algorithms that allow for arbitrary sets of objects to be regularized. In such

a framework, hierarchies can automatically be generated to satisfy any specification of topological part/whole relationships [49].

Lastly, some components of our label fusion approaches could be improved to incorporate a level of expected registration error to mitigate the effects of mis-registration of one or more atlas image to the image being segmented. JLF incorporates this based on intensity information from the underlying image, but when such intensity information is sparse, or the difference in intensity between adjacent labels is slight, other distance-based approaches may be applicable.

5.6 Conclusions

In this article, we present a novel segmentation pipeline which takes advantage of optimization techniques in segmentation through the use of:

- intensity distribution modelling through large-scale Gaussian mixture models to ensure more robust and accurate probabilistic models, and

- generalized hierarchical max-flow segmentation to optimally combine probabilistic information from the above two with boundary regularization requirements.

We have found that this multi-atlas based segmentation pipeline can be significantly improved by using a Kohonen self-organizing map based learning procedure for the large scale Gaussian mixture model over traditional expectation maximization, and the incorporation of hierarchical regularization and part-whole relationships over the traditional Potts model.

These results were determined based on segmentations of the OASIS database of T1-weighted MR images and the multi-channel MRBrainS 2013 database.

Bibliography

[1] Tina Kapur, W Eric L Grimson, William M Wells III, and Ron Kikinis. Segmentation of brain tissue from magnetic resonance images. *Medical image analysis*, 1(2):109–127, 1996.

[2] Yongyue Zhang, Michael Brady, and Stephen Smith. Segmentation of brain MR images through a hidden markov random field model and the expectation-maximization algorithm. *Medical Imaging, IEEE Transactions on*, 20(1):45–57, 2001.

[3] Rolf A Heckemann, Joseph V Hajnal, Paul Aljabar, Daniel Rueckert, and Alexander Hammers. Automatic anatomical brain MRI segmentation combining label propagation and decision fusion. *NeuroImage*, 33(1):115–126, 2006.

[4] Kilian M Pohl, Sylvain Bouix, Motoaki Nakamura, Torsten Rohlfing, Robert W McCarley, Ron Kikinis, W Eric L Grimson, Martha Elizabeth Shenton, and William M Wells. A hierarchical algorithm for MR brain image parcellation. *Medical Imaging, IEEE Transactions on*, 26(9):1201–1212, 2007.

[5] Fedde van der Lijn, Tom den Heijer, MM Breteler, and Wiro J Niessen. Hippocampus segmentation in MR images using atlas registration, voxel classification, and graph cuts. *Neuroimage*, 43(4):708, 2008.

[6] Jyrki MP Lötjönen, Robin Wolz, Juha R Koikkalainen, Lennart Thurfjell, Gunhild Waldemar, Hilkka Soininen, and Daniel Rueckert. Fast and robust multi-atlas segmentation of brain magnetic resonance images. *Neuroimage*, 49(3):2352–2365, 2010.

[7] Robin Wolz, Rolf A Heckemann, Paul Aljabar, Joseph V Hajnal, Alexander Hammers, Jyrki Lötjönen, and Daniel Rueckert. Measurement of hippocampal atrophy using 4D graph-cut segmentation: application to ADNI. *NeuroImage*, 52(1):109–118, 2010.

[8] Christian Ledig, Rolf A Heckemann, Alexander Hammers, and Daniel Rueckert. Improving whole-brain segmentations through incorporating regional image intensity statistics. In *SPIE Medical Imaging*, pages 86691M–86691M. International Society for Optics and Photonics, 2013.

[9] Tobias Heimann and Hans-Peter Meinzer. Statistical shape models for 3D medical image segmentation: A review. *Medical image analysis*, 13(4):543–563, 2009.

[10] Hongzhi Wang, Jung Wook Suh, Sandhitsu R Das, John B Pluta, Caryne Craige, and Paul A Yushkevich. Multi-atlas segmentation with joint label fusion. *Pattern Analysis and Machine Intelligence, IEEE Transactions on*, 35(3):611–623, 2013.

[11] Martin Rajchl, John SH Baxter, A Jonathan McLeod, Jing Yuan, Wu Qiu, Terry M Peters, James A White, and Ali R Khan. ASeTs: MAP-based brain tissue segmentation using manifold learning and hierarchical max-flow regularization. In *MRBrainS 2013 - MICCAI Grand Challenge on MR Brain Segmentation 2013*, 2014.

[12] Loredana Murino, Donatella Granata, Maria Francesca Carfora, S Selvan, Bruno Alfano, Umberto Amato, and Michele Larobina. Evaluation of supervised methods for the classification of major tissues and subcortical structures in multispectral brain magnetic resonance images. *Computerized Medical Imaging and Graphics*, 2014.

[13] Hayit Greenspan, Amit Ruf, and Jacob Goldberger. Constrained Gaussian mixture model framework for automatic segmentation of MR brain images. *Medical Imaging, IEEE Transactions on*, 25(9):1233–1245, 2006.

[14] Zexuan Ji, Yong Xia, Quansen Sun, Qiang Chen, and Dagan Feng. Adaptive scale fuzzy local Gaussian mixture model for brain MR image segmentation. *Neurocomputing*, 134: 60–69, 2014.

[15] Renske de Boer, Henri A Vrooman, Fedde van der Lijn, Meike W Vernooij, M Arfan Ikram, Aad van der Lugt, Monique Breteler, and Wiro J Niessen. White matter lesion

extension to automatic brain tissue segmentation on mri. *Neuroimage*, 45(4):1151–1161, 2009.

[16] Yuri Boykov and Marie-Pierre Jolly. Interactive organ segmentation using graph cuts. In *Medical Image Computing and Computer-Assisted Intervention–MICCAI 2000*, pages 276–286. Springer, 2000.

[17] Michael Wels, Gustavo Carneiro, Alexander Aplas, Martin Huber, Joachim Hornegger, and Dorin Comaniciu. A discriminative model-constrained graph cuts approach to fully automated pediatric brain tumor segmentation in 3-D MRI. In *Medical Image Computing and Computer-Assisted Intervention–MICCAI 2008*, pages 67–75. Springer, 2008.

[18] Zhuang Song, Nicholas Tustison, Brian Avants, and James C Gee. Integrated graph cuts for brain MRI segmentation. In *Medical Image Computing and Computer-Assisted Intervention–MICCAI 2006*, pages 831–838. Springer, 2006.

[19] Lichen Liang, Kelly Rehm, Roger P Woods, David A Rottenberg, et al. Automatic segmentation of left and right cerebral hemispheres from MRI brain volumes using the graph cuts algorithm. *NeuroImage*, 34(3):1160, 2007.

[20] Claudia Nieuwenhuis, Eno Töppe, and Daniel Cremers. A survey and comparison of discrete and continuous multi-label optimization approaches for the Potts model. *International Journal of Computer Vision*, pages 1–18, 2013.

[21] Thomas Pock, Antonin Chambolle, Daniel Cremers, and Horst Bischof. A convex relaxation approach for computing minimal partitions. In *Computer Vision and Pattern Recognition, 2009. CVPR 2009. IEEE Conference on*, pages 810–817. IEEE, 2009.

[22] Jing Yuan, Egil Bae, Xue-Cheng Tai, and Yuri Boykov. A continuous max-flow approach to potts model. In *Computer Vision–ECCV 2010*, pages 379–392. Springer, 2010.

[23] John SH Baxter, Martin Rajchl, A Jonathan McLeod, Ali R Khan, Jing Yuan, and Terry M Peters. Smoothness parameter tuning for generalized hierarchical continuous max-flow segmentation. In *SPIE Medical Imaging*, pages 903410–903410. International Society for Optics and Photonics, 2014.

[24] Hiroshi Ishikawa. Exact optimization for markov random fields with convex priors. *Pattern Analysis and Machine Intelligence, IEEE Transactions on*, 25(10):1333–1336, 2003.

[25] Egil Bae, Jing Yuan, Xue-Cheng Tai, and Yuri Boykov. A fast continuous max-flow approach to non-convex multilabeling problems. *Efficient global minimization methods for variational problems in imaging and vision*, pages 134–154, 2011.

[26] Martin Rajchl, Jing Yuan, James A White, Cyrus MS Nambakhsh, Eranga Ukwatta, Feng Li, John Stirrat, and Terry M Peters. A fast convex optimization approach to segmenting 3D scar tissue from delayed-enhancement cardiac MR images. In *Medical Image Computing and Computer-Assisted Intervention–MICCAI 2012*, pages 659–666. Springer Berlin Heidelberg, 2012.

[27] M Rajchl, J Yuan, J White, E Ukwatta, J Stirrat, C Nambakhsh, F Li, and T Peters. Interactive hierarchical max-flow segmentation of scar tissue from late-enhancement cardiac MR images. *IEEE Transactions on Medical Imaging*, 2014.

[28] Andrew Delong, Lena Gorelick, Olga Veksler, and Yuri Boykov. Minimizing energies with hierarchical costs. *International journal of computer vision*, 100(1):38–58, 2012.

[29] Daniel S Marcus, Tracy H Wang, Jamie Parker, John G Csernansky, John C Morris, and Randy L Buckner. Open access series of imaging studies (OASIS): cross-sectional MRI data in young, middle aged, nondemented, and demented older adults. *Journal of cognitive neuroscience*, 19(9):1498–1507, 2007.

[30] MALC. MICCAI grand challenge and workshop on multi-atlas labeling.

http://masi.vuse.vanderbilt.edu/workshop2012/, 2012. Accessed: 2014-05-08.

[31] MRBrainS. MICCAI grand challenge on MR brain image segmentation workshop. http://mrbrains13.isi.uu.nl/, 2013. Accessed: 2014-05-08.

[32] John SH Baxter, Martin Rajchl, Jing Yuan, and Terry M Peters. A continuous max-flow approach to general hierarchical multi-labelling problems. *arXiv preprint arXiv:1404.0336*, 2014.

[33] Dimitri P Bertsekas. Nonlinear programming. 1999.

[34] Martin Rajchl, John SH Baxter, Wu Qiu, Ali R Khan, Aaron Fenster, Terry M Peters, and Jing Yuan. RANCOR: Non-linear image registration with total variation regularization. *arXiv preprint arXiv:1404.2571*, 2014.

[35] Sébastien Ourselin, Radu Stefanescu, and Xavier Pennec. Robust registration of multi-modal images: towards real-time clinical applications. In *Medical Image Computing and Computer-Assisted InterventionMICCAI 2002*, pages 140–147. Springer, 2002.

[36] Arthur P Dempster, Nan M Laird, Donald B Rubin, et al. Maximum likelihood from incomplete data via the em algorithm. *Journal of the Royal statistical Society*, 39(1): 1–38, 1977.

[37] Teuvo Kohonen. The self-organizing map. *Proceedings of the IEEE*, 78(9):1464–1480, 1990.

[38] Tom Heskes. Self-organizing maps, vector quantization, and mixture modeling. *Neural Networks, IEEE Transactions on*, 12(6):1299–1305, 2001.

[39] Jakob J Verbeek, Nikos Vlassis, and Ben JA Kröse. Self-organizing mixture models. *Neurocomputing*, 63:99–123, 2005.

[40] Hujun Yin and Nigel M Allinson. Self-organizing mixture networks for probability density estimation. *Neural Networks, IEEE Transactions on*, 12(2):405–411, 2001.

[41] Neuromorphometrics. Neuromorphometrics, Inc. `http://www.neuromorphometrics.com/`, 2014. Accessed: 2014-05-08.

[42] Nicholas J Tustison and James C Gee. N4itk: Nick's N3 ITK implementation for MRI bias field correction. *Insight Journal*, 2009.

[43] ANTs. ANTs - Advanced Normalization Tools. `http://sourceforge.net/projects/advants/`, 2010. Accessed: 2014-05-08.

[44] RANCOR. RANCOR - registration via convex relaxation. `http://sourceforge.net/projects/rancor/`, 2014. Accessed: 2014-05-08.

[45] Marc Modat, Gerard R Ridgway, Zeike A Taylor, Manja Lehmann, Josephine Barnes, David J Hawkes, Nick C Fox, and Sébastien Ourselin. Fast free-form deformation using graphics processing units. *Computer methods and programs in biomedicine*, 98(3):278–284, 2010.

[46] Fionn Murtagh. Counting dendrograms: a survey. *Discrete Applied Mathematics*, 7(2): 191–199, 1984.

[47] Jing Yuan, Egil Bae, and Xue-Cheng Tai. A study on continuous max-flow and min-cut approaches. In *Computer Vision and Pattern Recognition (CVPR), 2010 IEEE Conference on*, pages 2217–2224. IEEE, 2010.

[48] Vladimir Kolmogorov and Ramin Zabih. Computing visual correspondence with occlusions using graph cuts. In *Computer Vision, 2001. ICCV 2001. Proceedings. Eighth IEEE International Conference on*, volume 2, pages 508–515. IEEE, 2001.

[49] John SH Baxter, Martin Rajchl, Jing Yuan, and Terry M Peters. A continuous max-flow

approach to multi-labeling problems under arbitrary region regularization. *arXiv preprint arXiv:1405.0892*, 2014.

Chapter 6

Conclusions

We presented methods for the segmentation of scar tissue from late-gadolinium-enhancement MRI and brain tissue from multi-sequence MRI in semi- and fully automated processing pipelines, respectively. Both methods employ a label hierarchy to extend the well-known Potts model to multi-region segmentation including prior information about the anatomical appearance and can be readily implemented using GPGPU for a substantial increase in computation speed.

The ability to individually regularize labels in these hierarchies allow for proper incorporation of variable smoothness requirements across different anatomical structures, thus resulting in more accurate segmentation. The advantages of the continuous max-flow formulations, such as avoidance of metrication artifacts and approximately globally optimal results, are preserved with this new formulation and add to those mentioned previously. Additionally, the ability to compute results within short time periods, make these algorithms available for large scale multi-labelling problems, such as gray matter parcellation of the brain or multi-organ segmentation in the abdomen.

Furthermore, two methods have been proposed and evaluated for the regularization of deformation fields to address the ill-posedness of deformable registration methods. Using an unsophisticated similarity metric, the sum-of-absolute intensity differences, we outperformed

four high-ranked and well-known methods in pairwise brain registrations. Both regularizers were implemented using GPGPU and demonstrated with far lower run times, while yielding high accuracy in the majority of metrics. The highest performing method was subsequently integrated into a multi-atlas pipeline for brain tissue segmentation, ranking high in a public segmentation challenge.

We want to emphasize that developments in the field of graphics hardware such as faster clock speeds, increase in memory, and available cores will largely impact the performance of GPU-based algorithm run times and so potentially facilitate real-time computations of variants of the proposed methods [1]. This is particularly of interest to the image-guided interventions community, where problems often have to be solved in to real-time to facilitate guidance or navigation tasks based on intra-operative imaging.

Future directions

Advanced Segmentation Tools (ASeTs)

In order to facilitate further development and advancement of the presented segmentation methods, all source code will be made available to the community in the form of a software repository. Further, we intend to provide simple examples on how to implement these max-flow methods into new pipelines to potentially solve new problems. For this purpose, we created the *Advanced Segmentation Tools (ASeTs)* library, containing a scalable implementation of the *Hierarchical Max-Flow* algorithm [2] employed in the Chapters 2 and 5. The optimizers and all employed data terms will be provided with an interface, to readily create modules in 'plug-and-play' manner using the well-known and established *VTK* library.

Further developments are intended to simplify customization of label ordering to solve other segmentation problems. Developments such as the *Directed Acyclic Graphical Max-Flow (DAGMF)* recently developed by Baxter et al. [3] allows labels to have multiple parents and allows for more intuitive design of the label ordering supporting any configuration created

using set theoretic operators. Additionally, recently proposed constraints can be enforced on labels to incorporate additional information about the objects, such as *Star-shape priors* [4] which enforce convexity of the region towards one or more points, or constraints on the volume of the segmented objects [5].

Lastly, we will provide general-purpose tools, such as those for multi-atlas label fusion problems and means of max-flow based contour evolution (see [6]), building and extending on developments in this thesis.

Registration via Convex Relaxation (RANCOR)

The *RANCOR* approach demonstrated promising performance in deformable image registration of pairwise brain images. Note, that the non-smooth total variation approach using the L^1 norm yielded higher accuracy than its quadratic counterpart. The source code of the former will be publicly released and optimizability of the L^p-norm, where $0 < p < 1$ investigated. Further, general means of improving registration methods, such as employing advanced similarity metrics, (i.e. mutual information, normalized cross-correlation or the MIND descriptor [7], or symmetric warping techniques) will be investigated.

We hope that methods developed in this thesis contribute to solving complex and important problems in the field of medical image analysis and continue to be employed within clinical studies to ultimately impact medical discovery and patient care.

Bibliography

[1] M Rajchl, J Yuan, and TM Peters. Real-time segmentation in 4D ultrasound with continuous max-flow. In *SPIE Medical Imaging*, pages 83141F–83141F. International Society for Optics and Photonics, 2012.

[2] John SH Baxter, Martin Rajchl, Jing Yuan, and Terry M Peters. A continuous max-flow approach to general hierarchical multi-labelling problems. *arXiv preprint arXiv:1404.0336*, 2014.

[3] John SH Baxter, Martin Rajchl, Jing Yuan, and Terry M Peters. A continuous max-flow approach to multi-labeling problems under arbitrary region regularization. *arXiv preprint arXiv:1405.0892*, 2014.

[4] Jing Yuan, Wu Qiu, Eranga Ukwatta, Martin Rajchl, Yue Sun, and Aaron Fenster. An efficient convex optimization approach to 3D prostate mri segmentation with generic star shape prior. *Prostate MR Image Segmentation Challenge, MICCAI*, 2012.

[5] Wu Qiu, Martin Rajchl, Fumin Guo, Yue Sun, Eranga Ukwatta, Aaron Fenster, and Jing Yuan. 3d prostate TRUS segmentation using globally optimized volume-preserving prior. In *Medical Image Computing and Computer-Assisted Intervention–MICCAI 2014*, volume Accepted. Springer Berlin Heidelberg, 2014.

[6] Eranga Ukwatta, Jing Yuan, Martin Rajchl, Wu Qiu, David Tessier, and Aaron Fenster. 3D carotid multi-region MRI segmentation by globally optimal evolution of coupled surfaces. *IEEE Transactions on Medical Imaging*, 32(4):770–785, 2013.

[7] Mattias P Heinrich, Mark Jenkinson, Manav Bhushan, Tahreema Matin, Fergus V Gleeson, Sir Michael Brady, and Julia A Schnabel. MIND: Modality independent neighbourhood descriptor for multi-modal deformable registration. *Medical Image Analysis*, 16(7):1423–1435, 2012.

Appendix A

Potts Model and Convex Relaxation

The Potts model originates from statistical physics [1]. Its spatially continuous version can be stated by partitioning the continuous image domain Ω into n disjoint subdomains $\{\Omega_i\}_{i=1}^n$ with the minimum total perimeter such that:

$$\min_{\{\Omega_i\}_{i=1}^n} \quad \sum_{i=1}^{n} \int_{\Omega_i} \rho_i(x)\, dx + \alpha \sum_{i=1}^{n} |\partial\Omega_i| \tag{A.1}$$

$$\text{s.t.} \quad \cup_{i=1}^{n} \Omega_i = \Omega\,; \quad \Omega_k \cap \Omega_l = \emptyset\,, \quad \forall k \neq l \tag{A.2}$$

where $|\partial\Omega_i|$ measures the perimeter of each disjoint subdomain Ω_i, $i = 1 \ldots n$; the function $\rho_i(x), i = 1 \ldots n$, evaluates the cost of assigning the label l_i to the specified position $x \in \Omega$ and the positive $\alpha > 0$ gives the trade-off between the total perimeter and assignment cost.

Obviously, the Potts model (A.1) favors the segmented regions with 'tight' boundaries and, by (A.2), each pixel can be assigned to only one region.

Let $u_i(x), i = 1 \ldots n$, denote the indicator function of each disjoint subdomain Ω_i, i.e.

$$u_i(x) := \begin{cases} 1\,, & x \in \Omega_i \\ 0\,, & x \notin \Omega_i \end{cases}, \quad i = 1 \ldots n\,. \tag{A.3}$$

Hence, the perimeter of each disjoint subdomain Ω_i can be evaluated by

$$|\partial\Omega_i| \;=\; \int_{\Omega} |\nabla u_i| \; dx\,, \quad i = 1 \ldots n\,. \tag{A.4}$$

In view of (A.3) and (A.4), the Potts model (A.1) can then be identically reformulated as

$$\min_{u_i(x)\in\{0,1\}} \sum_{i=1}^{n} \int_{\Omega} u_i(x)\rho_i(x)\, dx + \alpha \sum_{i=1}^{n} \int_{\Omega} |\nabla u_i| \; dx \tag{A.5}$$

$$\text{s.t.} \;\; \sum_{i=1}^{n} u_i(x) \;=\; 1\,, \quad \forall x \in \Omega\,; \tag{A.6}$$

where the constraints on $u_i(x)$, $i = 1 \ldots n$, in (A.6) just corresponds to the condition (A.2), i.e. each image pixel can be assigned to one and only one region.

Solving the Potts model (A.5) is challenging due to the binary constraint of each labeling function and the linear equality constraint (A.6). In this regard, the convex relaxation technique was recently developed to efficiently compute (A.5) by the reduced convex optimization problem:

$$\min_{u(x)\in\triangle_+} \sum_{i=1}^{n} \int_{\Omega} u_i(x)\, \rho_i(x)\, dx \;+\; \alpha \sum_{i=1}^{n} \int_{\Omega} |\nabla u_i| \; dx \tag{A.7}$$

where the binary constraint of each labeling function $u_i(x) \in \{0, 1\}$, $i = 1 \ldots n$, is relaxed to the convex section of $u_i(x) \in [0, 1]$, then at each pixel $x \in \Omega$, the labeling functions suffice the convex constrained set $\triangle_+$:

$$\sum_{i=1}^{n} u_i(x) \;=\; 1\,; \quad u_i(x) \in [0, 1]\,, \quad i = 1 \ldots n\,.$$

The main motivation of exploring such convex relaxation formulation is that a series of efficient convex optimization algorithms [2, 3, 4, 5, 6] can be employed to well approximate the original combinatorial optimization problem (A.5) in a computationally 'economical' way; such as the duality-based continuous max-flow approach [2, 3], the Douglas-Rachford splitting

algorithm [4], the iterative primal-dual algorithm [5] and the entropy-maximum regularized algorithm [6] etc.

In this work, we focus on the efficient continuous max-flow method, like [2, 3], which implicitly encodes the ordered region constraint with maximizing the corresponding flow functions and avoids directly tackling the existing non-smooth energy function terms.

Bibliography

[1] Renfrey B. Potts. Some generalized order-disorder transformations. *In Proceedings of the Cambridge Philosophical Society, Vol. 48*, pages 106–109, 1952.

[2] Jing Yuan, Egil Bae, Xue-Cheng Tai, and Yuri Boykov. A continuous max-flow approach to potts model. In *Computer Vision–ECCV 2010*, pages 379–392. Springer, 2010.

[3] J. Yuan, E. Bae, and X.C. Tai. A study on continuous max-flow and min-cut approaches. In *IEEE Computer Vision and Pattern Recognition – CVPR*, USA, San Francisco, 2010.

[4] Jan Lellmann, Jörg Kappes, Jing Yuan, Florian Becker, and Christoph Schnörr. Convex multi-class image labeling by simplex-constrained total variation. In *SSVM '09*, pages 150–162, 2009. ISBN 978-3-642-02255-5.

[5] A. Chambolle, D. Cremers, and T. Pock. A convex approach for computing minimal partitions. Technical Report TR-2008-05, University of Bonn, November 2008.

[6] E. Bae, J. Yuan, and X.C. Tai. Global minimization for continuous multiphase partitioning problems using a dual approach. Technical report CAM09-75, UCLA, CAM, September 2009.

Appendix B

RANCOR - Dual Optimization Analysis

Given the conjugate representation of the absolute function:

$$|v| \;=\; \max_{w} \; w \cdot v \,, \quad \text{s.t. } |w| \;\leq\; 1 \,, \tag{B.1}$$

we can rewrite the first L_1-norm term of (4.10) as follows:

$$\int_{\Omega} |P_0 + \nabla P \cdot h| \, dx \;=\; \max_{|w(x)| \leq 1} \int_{\Omega} w(P_0 + \nabla P \cdot h) dx \,. \tag{B.2}$$

Additionally, given the regularization function, $R(\tilde{u} + h)$, in terms of (4.6), we also have

$$\begin{aligned} & \alpha \sum_{i=1}^{3} \int_{\Omega} |\nabla(\tilde{u}_i + h_i)|^p \, dx \\ = \;& \max_{q} \; \sum_{i=1}^{3} \int \operatorname{div} q_i(\tilde{u}_i + h_i) dx - R_p^*(q) \,, \end{aligned} \tag{B.3}$$

where each dual variable $q_i(x)$, $i = 1, 2, 3$, gives a vector function and, for the case $p = 2$,

$$R_2^*(q) \;=\; \frac{1}{\alpha} \sum_{i=1}^{3} \int |q_i(x)|^2 \; dx \,, \tag{B.4}$$

for the case $p = 1$,

$$R_1^*(q) = \chi_{|q_{1,2,3}(x)|\leq\alpha}(q)\,, \tag{B.5}$$

i.e. the characteristic function of the constraints $|q_i(x)| \leq \alpha$, $i = 1, 2, 3$.

Considering (B.2) and (B.3), it is easy to see that the convex minimization problem (4.9) is mathematically equivalent to the following minimax problem:

$$\min_h \max_{|w(x)|\leq 1, q} \int w(P_0 + \nabla P \cdot h)dx + \sum_{i=1}^{3} \int \operatorname{div} q_i(\tilde{u}_i + h_i)dx - R_p^*(q) \tag{B.6}$$

i.e.

$$\min_h \max_{|w(x)|\leq 1, q} \int (wP_0 + \sum_{i=1}^{3} \tilde{u}_i \operatorname{div} q_i)dx + \sum_{i=1}^{3} \int h_i(w \cdot \partial_i P + \operatorname{div} q_i)dx - R_p^*(q) \tag{B.7}$$

which is called the *primal-dual formulation* in this thesis.

After variation by the free variable $h_i(x)$, $i = 1, 2, 3$, the minimization of the *primal-dual formulation* (B.7) over $h_i(x)$, $i = 1, 2, 3$, results in the linear equalities' constraints

$$(w \cdot \partial_i P + \operatorname{div} q_i)(x) = 0\,, \quad i = 1, 2, 3\,, \tag{B.8}$$

and the maximization problem

$$\max_{|w(x)|\leq 1, q} E(w, q) := \int (wP_0 + \sum_{i=1}^{3} \tilde{u}_i \operatorname{div} q_i)dx - R_p^*(q)$$

thereby proving Prop. 4.2.1.

Ethics Approval Notices

Research Western

Use of Human Participants - Ethics Approval Notice

Principal Investigator: James White
Review Number: 17696
Review Level: Delegated
Approved Local Adult Participants: 50
Approved Local Minor Participants: 0
Protocol Title: Multi-Modality Imaging Assessment for Pacing Interventions in Heart Failure: Targeting Optimal Sites and Outcomes (MAPIT-HF TOO)
Department & Institution: Medicine-Dept of, University of Western Ontario
Sponsor: Heart and Stroke Foundation of Canada

Ethics Approval Date: November 24, 2011 **Expiry Date:** December 31, 2014
Documents Reviewed & Approved & Documents Received for Information:

Document Name	Comments	Version Date
Other	Addition of research personnel: S. Haider, I. Petrov & J. Ouellette	

This is to notify you that The University of Western Ontario Research Ethics Board for Health Sciences Research Involving Human Subjects (HSREB) which is organized and operates according to the Tri-Council Policy Statement: Ethical Conduct of Research Involving Humans and the Health Canada/ICH Good Clinical Practice Practices: Consolidated Guidelines; and the applicable laws and regulations of Ontario has reviewed and granted approval to the above referenced revision(s) or amendment(s) on the approval date noted above. The membership of this REB also complies with the membership requirements for REB's as defined in Division 5 of the Food and Drug Regulations.

The ethics approval for this study shall remain valid until the expiry date noted above assuming timely and acceptable responses to the HSREB's periodic requests for surveillance and monitoring information. If you require an updated approval notice prior to that time you must request it using the UWO Updated Approval Request Form.

Members of the HSREB who are named as investigators in research studies, or declare a conflict of interest, do not participate in discussion related to, nor vote on, such studies when they are presented to the HSREB.

The Chair of the HSREB is Dr. Joseph Gilbert. The UWO HSREB is registered with the U.S. Department of Health & Human Services under the IRB registration number IRB 00000940.

Ethics Officer to Contact for Further Information

X Janice Sutherland (jsuther1@uwo.ca)	Grace Kelly (grace.kelly@uwo.ca)	Shantel Walcott (swalcot@uwo.ca)

This is an official document. Please retain the original in your files.

The **University** *of* **Western Ontario**
Office of Research Ethics
Support Services Building Room 5150 • London, Ontario • CANADA - N6G 1G9
PH: 519-661-3036 • F: 519-850-2466 • ethics@uwo.ca • www.uwo.ca/research/ethics

Office of Research Ethics
The University of Western Ontario
Room 5150 Support Services Building, London, ON, Canada N6A 3K7
Telephone: (519) 661-3036 Fax: (519) 850-2466 Email: ethics@uwo.ca
Website: www.uwo.ca/research/ethics

Use of Human Subjects - Ethics Approval Notice

Principal Investigator: Dr. J. White
Review Number: 17697 **Review Level:** Full Board
Review Date: January 11, 2011 **Approved Local # of Participants:** 150
Protocol Title: Canadian Cardiomyopathy Registry for Device therapy: a Magnetic Resonance imaging (CanCARD-MR) Study
Department and Institution: Cardiology, London Health Sciences Centre
Sponsor: CIHR-CANADIAN INSTITUTE OF HEALTH RESEARCH
Ethics Approval Date: February 24, 2011 **Expiry Date:** December 31, 2017
Documents Reviewed and Approved: UWO Protocol (including instruments noted in section 8.1), Letter of information & consent form dated January 17/11
Documents Received for Information: Protocol version 1.3 dated December 10/10

This is to notify you that The University of Western Ontario Research Ethics Board for Health Sciences Research Involving Human Subjects (HSREB) which is organized and operates according to the Tri-Council Policy Statement: Ethical Conduct of Research Involving Humans and the Health Canada/ICH Good Clinical Practice Practices: Consolidated Guidelines; and the applicable laws and regulations of Ontario has reviewed and granted approval to the above referenced study on the approval date noted above. The membership of this REB also complies with the membership requirements for REB's as defined in Division 5 of the Food and Drug Regulations.

The ethics approval for this study shall remain valid until the expiry date noted above assuming timely and acceptable responses to the HSREB's periodic requests for surveillance and monitoring information. If you require an updated approval notice prior to that time you must request it using the UWO Updated Approval Request Form.

During the course of the research, no deviations from, or changes to, the protocol or consent form may be initiated without prior written approval from the HSREB except when necessary to eliminate immediate hazards to the subject or when the change(s) involve only logistical or administrative aspects of the study (e.g. change of monitor, telephone number). Expedited review of minor change(s) in ongoing studies will be considered. Subjects must receive a copy of the signed information/consent documentation.

Investigators must promptly also report to the HSREB:

a) changes increasing the risk to the participant(s) and/or affecting significantly the conduct of the study;
b) all adverse and unexpected experiences or events that are both serious and unexpected;
c) new information that may adversely affect the safety of the subjects or the conduct of the study.

If these changes/adverse events require a change to the information/consent documentation, and/or recruitment advertisement, the newly revised information/consent documentation, and/or advertisement, must be submitted to this office for approval.

Members of the HSREB who are named as investigators in research studies, or declare a conflict of interest, do not participate in discussion related to, nor vote on, such studies when they are presented to the HSREB.

Chair of HSREB: Dr. Joseph Gilbert
FDA Ref. #: IRB 00000940

Ethics Officer to Contact for Further Information			
☑ Janice Sutherland (jsutherl@uwo.ca)	☐ Elizabeth Wambolt (ewambolt@uwo.ca)	☐ Grace Kelly (grace.kelly@uwo.ca)	

This is an official document. Please retain the original in your files.

cc: ORE File

Research Western

Use of Human Participants - Ethics Approval Notice

Principal Investigator: Dr. James White
Review Number: 13920
Review Level: Delegated
Approved Local Adult Participants: 2250
Approved Local Minor Participants: 0
Protocol Title: Evaluation of the Impact of Cardiovascular MRI On Therapeutic Decisions, Resource Utilization and Outcomes in Patients with Known or Suspected Cardiovascular Disease
Department & Institution: Medicine-Dept of, University of Western Ontario
Sponsor:
Ethics Approval Date: November 24, 2011 **Expiry Date:** December 31, 2022
Documents Reviewed & Approved & Documents Received for Information:

Document Name	Comments	Version Date
Other	Addition of student scientists: F. Jalilian, J. Liu, S. Haider & I. Petrov	

This is to notify you that The University of Western Ontario Research Ethics Board for Health Sciences Research Involving Human Subjects (HSREB) which is organized and operates according to the Tri-Council Policy Statement: Ethical Conduct of Research Involving Humans and the Health Canada/ICH Good Clinical Practice Practices: Consolidated Guidelines; and the applicable laws and regulations of Ontario has reviewed and granted approval to the above referenced revision(s) or amendment(s) on the approval date noted above. The membership of this REB also complies with the membership requirements for REB's as defined in Division 5 of the Food and Drug Regulations.

The ethics approval for this study shall remain valid until the expiry date noted above assuming timely and acceptable responses to the HSREB's periodic requests for surveillance and monitoring information. If you require an updated approval notice prior to that time you must request it using the UWO Updated Approval Request Form.

Members of the HSREB who are named as investigators in research studies, or declare a conflict of interest, do not participate in discussion related to, nor vote on, such studies when they are presented to the HSREB.

The Chair of the HSREB is Dr. Joseph Gilbert. The UWO HSREB is registered with the U.S. Department of Health & Human Services under the IRB registration number IRB 00000940.

Ethics Officer to Contact for Further Information

K Janice Sutherland (jsuther1@uwo.ca)	Grace Kelly (grace.kelly@uwo.ca)	Shantel Walcott (swalcot@uwo.ca)

This is an official document. Please retain the original in your files.

The **University** *of* **Western Ontario**
Office of Research Ethics
Support Services Building Room 5150 • London, Ontario • CANADA - N6G 1G9
PH: 519-661-3036 • F: 519-850-2466 • ethics@uwo.ca • www.uwo.ca/research/ethics

Copyright Notice

Thesis / Dissertation Reuse

The IEEE does not require individuals working on a thesis to obtain a formal reuse license, however, you may print out this statement to be used as a permission grant:

Requirements to be followed when using any portion (e.g., figure, graph, table, or textual material) of an IEEE copyrighted paper in a thesis:

1) In the case of textual material (e.g., using short quotes or referring to the work within these papers) users must give full credit to the original source (author, paper, publication) followed by the IEEE copyright line © 2011 IEEE.
2) In the case of illustrations or tabular material, we require that the copyright line © [Year of original publication] IEEE appear prominently with each reprinted figure and/or table.
3) If a substantial portion of the original paper is to be used, and if you are not the senior author, also obtain the senior author's approval.

Requirements to be followed when using an entire IEEE copyrighted paper in a thesis:

1) The following IEEE copyright/ credit notice should be placed prominently in the references: © [year of original publication] IEEE. Reprinted, with permission, from [author names, paper title, IEEE publication title, and month/year of publication]
2) Only the accepted version of an IEEE copyrighted paper can be used when posting the paper or your thesis on-line.
3) In placing the thesis on the author's university website, please display the following message in a prominent place on the website: In reference to IEEE copyrighted material which is used with permission in this thesis, the IEEE does not endorse any of [university/educational entity's name goes here]'s products or services. Internal or personal use of this material is permitted. If interested in reprinting/republishing IEEE copyrighted material for advertising or promotional purposes or for creating new collective works for resale or redistribution, please go to http://www.ieee.org/publications_standards/publications/rights/rights_link.html to learn how to obtain a License from RightsLink.

If applicable, University Microfilms and/or ProQuest Library, or the Archives of Canada may supply single copies of the dissertation.

BACK CLOSE WINDOW

Curriculum Vitae

Name: Martin Rajchl

WWW: http://www.imaging.robarts.ca/petergrp/martin-rajchl

Post-secondary Education and Degrees

2014 PhD. in Biomedical Engineering
Robarts Research Institute, Western University, London, ON

2010 MSc. in Biomedical Engineering Sciences
UAS Technikum Wien, Vienna

2008 BSc. in Biomedical Engineering
UAS Technikum Wien, Vienna

Honors, Awards & Academic Accomplishments

2013 Fellow Strategic Training Program in Vascular Research
2010 Awarded Success with Good Honors at Master's thesis defense
2008 Awarded Success with Distinction at Bachelor's thesis defense

Scholarships, Fellowships & Funding Opportunities

2010-2014 Western Graduate Research Scholarship (WGRS) - (CAD $17500/yr)
2011-2012 Canadian Institutes of Health Research (CIHR)
Strategic Training Program in Vascular Research (CAD $12000/yr)

Teaching

2013-2014 Teaching Assistant, Western University, London, ON
Faculty of Engineering - Dept. of Biomedical Engineering
Advanced Medical Image Processing and Analysis
2011-2014 Teaching Assistant, Western University, London, ON
Faculty of Engineering - Dept. of Electrical and Computer Engineering
Programming Fundamentals for Engineers
2012-2014 Mentoring of two clinical research assistants, CMCR Program, Robarts Research
Western University, London, ON.

Oral Presentations

2012 SPIE Medical Imaging, San Diego, CA
2012 IEEE International Symposium on Biomedical Imaging (ISBI), Barcelona, ESP
2012 Canadian Cardiovascular Congress, Toronto, ON

Invited Talks

2013 Robarts Research MedIA Series, London, ON
2012 Imperial College, Department of Computing, London, UK

Poster Presentations

2014 SPIE Medical Imaging, San Diego, CA
2014 Imaging Network Ontario (IMNO) 2014, Toronto, ON
2014 London Health Research Day 2014, London, ON
2013 IEEE Conf. on Computer Vision and Pattern Recognition (CVPR) 2013, Portland, OR
2013 Imaging Network Ontario (IMNO) 2013, Toronto, ON
2013 London Imaging Discovery (LID) 2013, London, ON
2012 Intl. Conf. on MICCAI 2012, Nice, FRA
2012 Imaging Network Ontario (IMNO) 2012, Toronto, ON
2012 London Imaging Discovery (LID) 2012, London, ON

Scientific Review Boards

2012-* IEEE Transaction on Medical Imaging
2013-* Medical Physics
2013-* International Journal of Computer-Assisted Radiology and Surgery
2013-* Journal of Medical Imaging
2014-* IEEE Canadian Journal of Electrical and Computer Engineering
2014-* Medical Image Computing and Computer Assisted Interventions (MICCAI)
2014-* Computer Methods and Programs in Biomedicine

Professional Associations and Scientific Societies

2012-* Institute of Electrical and Electronics Engineers (IEEE)
2012-* Medical Image Computing and Computer Assisted Interventions (MICCAI) Society
2012-* International Society of Optical Engineers (SPIE)

Collaborations

2012-2014 Neochord Inc., Eden Prairie, MN
2012-2013 Medtronic Inc., Fridley, MN
2007-2008 Carl Reiner Ltd., Vienna, AUT

Publications

Journal Articles in Review/under Revision

R10. F.P. Li, M. Rajchl, J.Moore, and T.M. Peters (2014). A Mitral Annulus Tracking Approach for Navigation of Off-pump Beating Heart Mitral Valve Repair. Medical Physics.

R09. F.P. Li, M. Rajchl, J.A. White, A. Goela, and T.M. Peters (2014). Ultrasound Guidance for Beating Heart Mitral Valve Repair Augmented by Synthetic Dynamic CT. IEEE Transactions on Medical Imaging.

R08. C. Petitjean, M.A. Zuluaga, J.-N. Dacher, D. Grosgeorge, J. Caudron, W. Bai, I. Ben Ayed, M.J. Cardoso, H.-C. Chen, D. Jimenez-Carretero, M.J. Ledesma-Carbayo, C. Davatzikos, J. Doshi, G. Erus, O.M.O. Maier, C.M.S. Nambakhsh, Y. Ou, S. Ourselin, C.-W. Peng, N.S. Peters, T.M. Peters, M. Rajchl, D. Rueckert, A. Santos, W. Shi, C.-W. Wang, H. Wang, J. Yuan, and S. Ruan (2014). Right Ventricle Segmentation From Cardiac MRI: A Collation Study. Medical Image Analysis.

R07. A.M. Mendrik, K.L. Vincken, H.J. Kuijf, M. Breeuwer, W. Bouvy, J. de Bresser, A. Alansary, M. de Bruijne, A. Carass, A. ElBaz, A. Jog, R. Katyal, A.R. Khan, F. van der Lijn, Q. Mahmood, R. Mukherjee, A. van Opbroek, S. Paneri, S. Pereira, M. Persson, M. Rajchl, D. Sarikaya, O. Smedby, C.A. Silva, H.A. Vrooman, S. Vyas, C. Wang, L. Zhao, G.J. Biessels, and M.A. Viergever (2014). MRBrainS Challenge: Online Evaluation Framework for Brain Image Segmentation in 3T MRI Scans. Neuroinformatics.

R06. Y. Sun, J. Yuan, W. Qiu, M. Rajchl, C. Romagnoli, and A. Fenster. Three-Dimensional Non-Rigid MR-TRUS Registration Using Dual Optimization. IEEE Transactions on Medical Imaging.

R05. Y. Mikami, L. Kolman, S.X. Joncas, J. Stirrat, D. Scholl, M. Rajchl, C. Lydell, S. Weeks, A. Howarth, and J.A. White (2014). Accuracy and Reproducibility of Semi-automated Late Gadolinium Enhancement Quantification Techniques in Patients with Hypertrophic Cardiomyopathy. Journal of Cardiovascular Magnetic Resonance.

R04. M. Rajchl, J. Stirrat, M. Goubran, J. Yu, D. Scholl, T.M. Peters, and J.A. White (2014). Comparison of Semi-automated Scar Quantification Techniques Using High-Resolution, 3-Dimensional Late-Gadolinium-Enhancement Magnetic Resonance Imaging. The International Journal of Cardiovascular Imaging.

R03. J. Stirrat, M. Rajchl, L. Bergin, D.J. Patton, T.M. Peters, and J.A. White (2014). High-resolution 3-Dimensional Late Gadolinium Enhancement Scar Imaging in Surgically Corrected Tetralogy of Fallot: Clinical Feasibility of Volumetric Quantification and Visualization. Journal of Cardiovascular Magnetic Resonance.

R02. M. Rajchl, J.S.H. Baxter, A.J. McLeod, J. Yuan, W. Qiu, T.M.Peters, and A.R. Khan (2014). Hierarchical Max-Flow Segmentation Framework For Multi-Atlas Segmentation with Kohonen Self-Organizing Map Based Gaussian Mixture Modeling. Medical Image Analysis.

R01. M. Rajchl, J.S.H. Baxter, W. Qiu, A.R. Khan, A. Fenster, T.M. Peters, and J.Yuan (2014). Fast Deformable Image Registration with Non-Smooth Dual Optimization. IEEE Transactions on Medical Imaging.

Peer-reviewed Journal Articles

J09. Z. Laksman, R. Yee, J. Stirrat, L.J. Gula, A.C. Skanes, P. Leong-Sit, J. Manlucu, G.J. Klein, D. McCarty, D. Scholl, M. Rajchl, A. Goela, A. Islam, T. Thompson, M. Drangova, and J.A. White (2014). Model-based Navigation of Left and Right Ventricular Leads to Optimal Targets in Patients Undergoing Cardiac Resynchronization Therapy: A Single Centre Feasibility Study. Circulation Arrhythmia and Electrophysiology. (Accepted.)

J08. Rajchl M., J. Yuan, J. White, E. Ukwatta, J. Stirrat, C. Nambakhsh, F. Li, and T. Peters (2014). Interactive Hierarchical Max-Flow Segmentation of Scar Tissue from Late-Enhancement Cardiac MR Images. IEEE Transactions on Medical Imaging 33(1), 159-172.

J07. Qiu, W., J. Yuan, E. Ukwatta, Y. Sun, Rajchl M., and A. Fenster (2014). Dual Optimization Based Prostate Zonal Segmentation in 3D MR Images. Medical Image Analysis 18(5), 660-673.

J06. Qiu, W., J. Yuan, E. Ukwatta, Y. Sun, Rajchl M., and A. Fenster (2014). Prostate Segmentation: An Efficient Convex Optimization Approach with Axial Symmetry Using 3D TRUS and MR Images. IEEE Transactions on Medical Imaging 33(5), 947-960.

J05. White, J.A., Rajchl M., J. Butler, R.T. Thompson, F.S. Prato, and G. Wisenberg (2013). Active Cardiac Sarcoidosis: First Clinical Experience of Simultaneous Positron Emission TomographyMagnetic Resonance Imaging for the Diagnosis of Cardiac Disease. Circulation 127(22), e639-e641.

J04. Nambakhsh, C.M.S., J. Yuan, K. Punithakumar, A. Goela, M. Rajchl, T. M. Peters, and I.B. Ayed (2013). Left Ventricle Segmentation in MRI via Convex Relaxed Distribution Matching. Medical Image Analysis 17(8), 1010-1024.

J03. Ukwatta, E., J. Yuan, M. Rajchl, W. Qiu, D. Tessier, and A. Fenster (2013). 3D Carotid Multi-Region MRI Segmentation by Globally Optimal Evolution of Coupled Surfaces. IEEE Transactions on Medical Imaging 32(4), 770-785.

J02. Moore, J.T., M.W.A. Chu, B. Kiaii, D. Bainbridge, G. Guiraudon, C. Wedlake, M. Currie, M. Rajchl, R.V. Patel, and T.M. Peters (2013). A navigation platform for guidance of beating heart transapical mitral valve repair. IEEE Transactions on Biomedical Engineering 60(4), 1034-1040.

J01. Chu, M. W., J. Moore, T. Peters, D. Bainbridge, D. McCarty, G. M. Guiraudon, C. Wedlake, P. Lang, M. Rajchl, M. E. Currie, et al. (2012). Augmented Reality Image Guidance Improves Navigation for Beating Heart Mitral Valve Repair. Innovations: Technology and Techniques in Cardiothoracic and Vascular Surgery 7(4), 274-281

Peer-reviewed Articles in Conference Proceedings

C23. Qiu, W., M. Rajchl, F. Guo, Y. Sun, E. Ukwatta, A. Fenster, and J. Yuan (2014). 3D Prostate TRUS Segmentation Using Globally Optimized Volume-Preserving Prior. In: Medical Image Computing and Computer-Assisted Intervention (MICCAI) 2014. Springer Berlin Heidelberg, (Accepted).

C22. Rajchl M., K. Abhari, J. Stirrat, E. Ukwatta, D. Cantor-Rivera, F. P. Li, T. M. Peters, and J. A. White (2014). Distribution of guidance models for cardiac resynchronization therapy in the setting of multi-center clinical trials. In: SPIE Medical Imaging, 90361V-90361V-7.

C21. Baxter, J. S., M. Rajchl, A. J. McLeod, A. R. Khan, J. Yuan, and T. M. Peters (2014). Smoothness parameter tuning for generalized hierarchical continuous max-flow segmentation. In: SPIE Medical Imaging, 903410-903410-8.

C20. Li, F. P., M. Rajchl, J. T. Moore, and T. M. Peters (2014). Ultrasound based mitral valve annulus tracking for off-pump beating heart mitral valve repair. In: SPIE Medical Imaging, 90361M-90361M-9.

C19. Inoue, J., A. C. Skanes, J. A. White, M. Rajchl, and M. Drangova (2014). Patient-specific left atrial wall-thickness measurement and visualization for radiofrequency ablation. In: SPIE Medical Imaging, 90361N-90361N-6.

C18. Li, F., M. Rajchl, J. A. White, A. Goela, and T. M. Peters (2013). Towards CT Enhanced Ultrasound Guidance for Off-pump Beating Heart Mitral Valve Repair. In: MIAR/AE-CAI, 136-143.

C17. Yuan, J., E. Ukwatta, W. Qiu, M. Rajchl, Y. Sun, X.-C. Tai, and A. Fenster (2013). Jointly Segmenting Prostate Zones in 3D MRIs by Globally Optimized Coupled Level-Sets. In: Energy Minimization Methods in Computer Vision and Pattern Recognition. Springer Berlin Heidelberg, pp.12-25.

C16. Sun, Y., J. Yuan, M. Rajchl, W. Qiu, C. Romagnoli, and A. Fenster (2013). Efficient Convex Optimization approach to 3D Non-rigid MR-TRUS Registration. In: Medical Image Computing and Computer-Assisted InterventionMICCAI 2013. Springer Berlin Heidelberg, pp.195-202.

C15. Qiu, W., J. Yuan, E. Ukwatta, Y. Sun, M. Rajchl, and A. Fenster (2013). Fast Globally Optimal Segmentation of 3D Prostate MRI with Axial Symmetry Prior. In: Medical Image Computing and Computer-Assisted InterventionMICCAI 2013. Springer Berlin Heidelberg, pp.198-205.

C14. Ukwatta, E., J. Yuan, W. Qiu, M. Rajchl, B. Chiu, S. Shavakh, J. Xu, and A. Fenster (2013). Joint Segmentation of 3D Femoral Lumen and Outer Wall Surfaces from MR Images. In: Medical Image Computing and Computer-Assisted InterventionMICCAI 2013. Springer Berlin Heidelberg, pp.534-541.

C13. Yuan, J., W. Qiu, M. Rajchl, E. Ukwatta, X.-C. Tai, and A. Fenster (2013). Efficient 3D Endfiring TRUS Prostate Segmentation with Globally Optimized Rotational Symmetry. IEEE Conference on Computer Vision and Pattern Recognition (CVPR), 2211-2218.

C12. Qiu, W., J. Yuan, E. Ukwatta, M. Rajchl, S. Yue, and A. Fenster (2013). Efficient 3D Multi-Region Prostate MRI Segmentation using Dual Optimization. In: Information Processing in Medical Imaging. Springer Berlin Heidelberg, pp.304-315.

C11. Li, F., M. Rajchl, J. White, A. Goela, and T. Peters (2013). Generation of Synthetic 4D Cardiac CT Images for Guidance of Minimally Invasive Beating Heart Interventions. In: Information Processing in Computer-Assisted Interventions. Springer Berlin Heidelberg, pp.11-20.

C10. Li, F., J. A. White, M. Rajchl, A. Goela, and T. M. Peters (2013). Generation of Synthetic 4D Cardiac CT Images by Deformation from Cardiac Ultrasound. In: Augmented Environments for Computer-Assisted Interventions. Springer Berlin Heidelberg, pp.132-141.

C09. Ukwatta, E., J. Yuan, W. Qiu, M. Rajchl, and A. Fenster (2013). Efficient convex optimization-based curvature dependent contour evolution approach for medical image segmentation. In: SPIE Medical Imaging. International Society for Optics and Photonics, pp.866902866902.

C08. Rajchl M., J. Yuan, J. White, E. Ukwatta, M. Nambakhsh, J. Stirrat, and T. Peters (2012). A Fast Convex Optimization Approach to Segmenting 3D Scar Tissue from Delayed-Enhancement Cardiac MR Images. In: Medical Image Computing and Computer-Assisted InterventionMICCAI 2012. Springer Berlin Heidelberg, pp.659666.

C07. Rajchl M., J. Yuan, E. Ukwatta, and T. Peters (2012). Fast Interactive Multi-Region Cardiac Segmentation With Linearly Ordered Labels. In: Biomedical Imaging (ISBI), 2012 9th IEEE International Symposium on. IEEE Conference Publications, pp.1409-1412.

C06. Rajchl M., J. Yuan, and T. Peters (2012). Real-time segmentation in 4D ultrasound with continuous max-flow. In: SPIE Medical Imaging. International Society for Optics and Photonics, pp.83141F-83141F.

C05. Ukwatta, E., J. Yuan, M. Rajchl, and A. Fenster (2012). Efficient Global Optimization Based 3D Carotid AB-LIB MRI Segmentation by Simultaneously Evolving Coupled Surfaces. In: Medical Image Computing and Computer-Assisted InterventionMICCAI 2012. Springer Berlin Heidelberg, pp.377-384.

C04. Moore, J., C. Wedlake, D. Bainbridge, G. Guiraudon, M. Chu, B. Kiaii, P. Lang, M. Rajchl, and T. Peters (2012). A navigation platform for guidance of beating heart transapical mitral valve repair. In: Information Processing in Computer-Assisted Interventions. Lecture Notes in Computer Science. Springer Berlin / Heidelberg, pp.84-93.

C03. Lang, P., M. Rajchl, A. McLeod, M. Chu, and T. Peters (2012). Feature identification for image-guided transcatheter aortic valve implantation. In: SPIE Medical Imaging. International Society for Optics and Photonics, pp.83162X-83162X.

C02. Lang, P., M. Rajchl, F. Li, and T. Peters (2011). Towards Model-Enhanced Real-Time Ultrasound Guided Cardiac Interventions. In: Intelligent Computation and Bio-Medical Instrumentation (ICBMI), 2011 International Conference on. IEEE, pp.89-92.

C01. Li, F., P. Lang, M. Rajchl, E. Chen, G. Guiraudon, and T. Peters (2012). Towards real-time 3D US-CT registration on the beating heart for guidance of minimally invasive cardiac interventions. In: SPIE Medical Imaging. International Society for Optics and Photonics, pp.831615-831615.

Other Abstracts in Conference Proceedings

O14. Rajchl M., J. Baxter, J. Yuan, T. Peter, and A. Khan (2013). Multi-Atlas-based Segmentation with Hierarchical Max-Flow. In: Grand Challenge: MRBrainS13 (MICCAI) - 2013.

O13. Ukwatta, E., J. Yuan, B. Chiu, W. Qiu, Rajchl M., and A. Fenster (2013). Robust 3D MRI Segmentation of Superficial Femoral Artery for Morphological Analysis of Peripheral Arterial Disease Plaque Burden. In: Annual Meeting 2013 of the Radiological Society of North America (RSNA).

O12. White, J., M Rajchl, J Butler, J Sykes, K Blackwood, R. Thompson, F. Prato, and G Wisenberg (2013). Influence of Microvascular Obstruction on Cellular Inflammation During Early Stages of Acute Myocardial Infarction: Evaluation Using Hybrid Pet-MRI Imaging. Canadian Journal of Cardiology 29(10), S135S136.

O11. Prato, F. S., J. A. White, Rajchl M., J Skyes, J. Butler, K Blackwood, R. T. Thompson, and G. Wisenberg (2013). Hybrid PET/MRI Cardiac Imaging in Canine Myocardial Infarction: Extent of Inflammation by 18FDG in no-reflow, hyper enhanced and remote myocardium as defined by late gadolinium enhanced MRI. In: The Sixth Annual World Molecular Imaging Congress.

O10. Rajchl M., F. Li, J. Moore, C. Wedlake, U. Aladl, and T. Peters (2013). Feature Tracking for Image guided Mitral Valve Repair. In: National Image-Guided Therapy Workshop 2013, Arlington, VA. NCIGT.

O09. Li, F., M. Rajchl, J. Moore, C. Wedlake, and T. Peters (2013). CT-Enhanced Ultrasound for Guidance of Off-pump Beating Heart Interventions. In: National Image-Guided Therapy Workshop 2013, Arlington, VA. NCIGT.

O08. Rajchl M., J. Stirrat, T. Peters, and J. White (2013). Rapid Segmentation of Myocardial Scar from 3D Late Gadolinium Enhancement Magnetic Resonance Imaging. In: Imaging Network Ontario.

O07. Cepek, J., M. Rajchl, J. Trachtenberg, and A. Fenster (2013). Evaluation of Tissue Thermal Damage Models in in vivo Human Prostate Tissue. In: Imaging Network Ontario.

O06. Li, F., J. White, M. Rajchl, A. Goela, and T. Peters (2013). Generation of Synthetic 4D Cardiac CT Images for Guidance of Off-pump Beating Heart Interventions. In: Imaging Network Ontario.

O05. Yuan, J., W. Qiu, E. Ukwatta, M. Rajchl, Y. Sun, and A. Fenster (2012). An Efficient Convex Optimization Approach to 3D Prostate MRI Segmentation with Generic Star Shape Prior. In: Grand Challenge: Prostate MR Image Segmentation (MICCAI) - 2012.

O04. Nambakhsh, C., M. Rajchl, J.Yuan, T. Peters, and I. Ben-Ayed (2012). Rapid Automated 3D RV Endocardium Segmentation in MRI via Convex Relaxation and Distribution Matching. In: RV Segmentation Challenge in Cardiac MRI (MICCAI) - 2012.

O03. Rajchl M., J. Stirrat, T. Peters, and J. White (2012). Rapid Segmentation of Myocardial Scar From 3-Dimensional Late Gadolinium Enhancement Magnetic Resonance Imaging. Canadian Journal of Cardiology 28(5), S395.

O02. Stirrat, J., M. Rajchl, L. Bergin, T. Peters, and J. White (2012). 3-Dimensional Late Gadolinium Enhancement Scar Imaging For Surgically Corrected Tetrology Of Fallot: Clinical Feasibility Of Scar Segmentation. Canadian Journal of Cardiology 28(5), S141.

O01. Rajchl M., J.Yuan, D.McCarty, and T. Peters (2012). Real-time Segmentation in 4D Ultrasound with Continuous Max-Flow. In: Imaging Network Ontario.

Technical Reports

T03. Baxter, J. S., M. Rajchl, J. Yuan, and T. M. Peters (2014). A Continuous Max-Flow Approach to Multi-Labeling Problems under Arbitrary Region Regularization. arXiv preprint arXiv:1405.0892.

T02. Baxter, J. S., M. Rajchl, J. Yuan, and T. M. Peters (2014). A Continuous Max-Flow Approach to General Hierarchical Multi-Labelling Problems. arXiv preprint arXiv:1404.0336.

T01. Rajchl M., J. S. Baxter, W. Qiu, A. R. Khan, A. Fenster, T. M. Peters, and J. Yuan (2014). RANCOR: Non-Linear Image Registration with Total Variation Regularization. arXiv preprint arXiv:1404.2571.